Reappraisal of Transcallosal Neuron Organization in Mice and Evaluation of Their Dendritic Remodeling and Circuit Integration Following Traumatic Brain Injury

Dissertation

zum Erwerb des Doktorgrades der Naturwissenschaften

an der Medizinischen Fakultät der

Ludwig-Maximilians-Universität München

Angefertigt am Institut für klinische Neuroimmunologie, LMU München

eingereicht von

Alexandra Chovsepian

2018

Aus dem Institut für klinische Neuroimmunologie der Ludwig-Maximilians-Universität München

Vorstand: Prof. Dr. Hohlfeld, Prof. Dr. Kerschensteiner

Reappraisal of Transcallosal Neuron Organization in Mice and Evaluation of Their Dendritic Remodeling and Circuit Integration Following Traumatic Brain Injury

Dissertation
zum Erwerb des Doktorgrades der Naturwissenschaften
an der Medizinischen Fakultät der
Ludwig-Maximilians-Universität zu München

vorgelegt von

Alexandra Chovsepian

aus

Athen, Griechenland

Jahr

2018

Mit Genehmigung der Medizinischen Fakultät
der Universität München

Betreuer(in): P.D. Dr. Florence Bareyre

Zweitgutachter: Prof. Dr. Stephan Kröger

Dekan: Prof. Dr. med. dent. Reinhard Hickel

Tag der mündlichen Prüfung: 26.06.2019

LMU LUDWIG-
MAXIMILIANS-
UNIVERSITÄT
MÜNCHEN

Dean's Office
Medical Faculty

Affidavit

Chovsepian, Alexandra

Surname, first name

_____

Street

_____

Zip code, town

_____

Country

I hereby declare, that the submitted thesis entitled

Reappraisal of Transcallosal Neuron Organization in Mice and Evaluation of Their Dendritic Remodeling and Circuit Integration Following Traumatic Brain Injury

is my own work. I have only used the sources indicated and have not made unauthorised use of services of a third party. Where the work of others has been quoted or reproduced, the source is always given.

I further declare that the submitted thesis or parts thereof have not been presented as part of an examination degree to any other university.

Munich, 08.07.2019

Place, date

Alexandra
Chovsepian
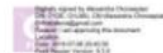
Signature doctoral candidate

To my grandmother Anna Margariti (1929-2009) and her beautiful mind that was never defeated by her Alzheimer's

TABLE OF CONTENTS

ABSTRACT

Traumatic Brain Injury (TBI) is an enormous global socio-economic burden since, apart from its high death rate, it is the primary cause of coma worldwide and a prevalent cause of long-term disability. Until today there is no established treatment for dealing with the long-term outcomes of TBI despite many years of research. Although a lot is known about the pathophysiology of TBI in the damaged tissue and the surrounding area in case of focal lesion, only few studies have investigated the structural and functional integrity of the contralateral intact cortex. In order to explore this territory, this study employs a well-established and widely used animal model of focal open skull TBI known as the Controlled Cortical Impact (CCI) model.

The first aim of this study was to systematically characterize a specific neuronal population, the transcallosal projection neurons, as they are the ones connecting the intact cortex with the lesioned cortex. The description of the organization of transcallosal neurons and their axonal projections at the contralateral hemisphere was carried out in healthy, non-injured C57Bl6 mice. Retrograde and anterograde tracing methods were implemented to label transcallosal cell bodies and their axonal projections, respectively. In addition, different injection coordinates were used in order to label transcallosal connections at distinct brain regions, including the motor cortex (M1), somatosensory cortex (S1), and barrel cortex, rostral and caudal to Bregma. In agreement with previous research, I observed that transcallosal projections are organized homotopically across the various brain regions, with the axonal terminals spanning the entire cortical column. Interestingly my study describes for the first time a non-negligible fraction of heterotopic transcallosal neurons that, in addition, display a slightly less strict layer distribution pattern compared to the homotopic ones.

After the initial characterization of transcallosal neuron organization, I proceeded by investigating how these neurons with projections at the injury site are affected at various timepoints following focal TBI. I used GFPM mice to visualize dendrites and spines of transcallosal and non-transcallosal neurons, in order to examine their structural integrity at different timepoints post-injury. I detected significant differences in dendritic spine density and morphology between controls and injured mice, which were time-dependent. More specifically, the dendritic spine density in transcallosal neurons was strongly decreased as soon as 7days following injury. Interestingly, spine density in non-transcallosal neurons was not changed following TBI. In terms of spine shape, I found a morphological shift only for the apical tuft segments. These results point towards a general sensitivity of transcallosal spines to TBI-

induced damage, where loss of spines (preferentially mature) seems to take place at 1-2 weeks post-injury and resolve at 3-6 weeks post-injury, indicative of late plasticity processes. As the anatomically connected neuronal population seems to recover overtime I then decided to further explore whether transcallosal circuit remodeling takes place after TBI. To do so I used the retrograde mono-trans-synaptic tracer SADΔG-GFP (EnvA) Rabies virus. In that way, I was able to distinctively label transcallosal neurons and their presynaptic partners and obtain an overview of the presynaptic population throughout the cortex across brain regions at different post-injury timepoints. This study demonstrates that spine plasticity did not result in adaptive circuit plasticity with the recruitment of other brain regions but rather that initial circuits were re-established.

In brief, during this thesis I have demonstrated the adaptive plastic capacities of anatomically connected neurons to the brain injury. I believe that this knowledge may help in unraveling further compensatory plastic mechanisms that could then be therapeutically targeted to improve the outcome following brain injury.

ZUSAMENFASSUNG

Schädel-Hirn-Traumata (SHT) sind eine enorme und globale sozioökonomische Belastung, da sie - abgesehen von der damit einhergehenden hohen Sterblichkeitsrate - weltweit die Hauptursache für Komas und eine häufige Ursache für Langzeitbehinderungen sind. Bis heute gibt es trotz langjähriger Forschung keine etablierte Behandlung der langfristigen Auswirkungen von SHT. Obwohl viel über die Pathophysiologie von SHT im beschädigten Gewebe und dessen Umgebung bei fokalen Läsionen bekannt ist, haben nur wenige Studien die strukturelle und funktionelle Integrität des kontralateralen intakten Kortex untersucht. Um dieses Gebiet zu erkunden, verwendet diese Studie ein gut etabliertes und weit verbreitetes Tiermodell eines fokalen offenen Schädel-SHT, welches als traumatisches kortikales Kontusionsmodell bekannt ist.

Das erste Ziel dieser Studie war die systematische Charakterisierung einer bestimmten neuronalen Population, der transkallosalen Projektionsneuronen, da diese den intakten Kortex mit dem verletzten Kortex verbinden. Die Beschreibung der Organisation trankallosaler Neurone und ihrer axonalen Projektionen an der kontralateralen Hemisphäre wurde in gesunden, nicht verletzten C57Bl6-Mäusen durchgeführt. Retrograde und anterograde Verfolgungsmethoden wurden implementiert, um transkallosale Zellkörper bzw. deren axonale Projektionen zu markieren. Darüber hinaus wurden verschiedene Injektionskoordinaten verwendet, um transkallosale Verbindungen in diversen Hirnregionen kranial und kaudal zu Bregma zu markieren, einschließlich Motorkortex (M1), somatosensorischer Kortex (S1) und Barrel-Kortex. In Übereinstimmung mit früheren Forschungen beobachte Ich, dass Transkallosalprojektionen homotopisch in den verschiedenen Hirnregionen organisiert sind, wobei die axonalen Endungen die gesamte kortikale Säule umfassen. Interessanterweise beschreibt diese Studie zum ersten Mal einen nicht vernachlässigbaren Anteil von heterotopischen, transkallosalen Neuronen, die im Vergleich zu den homotopischen Neuronen ein etwas weniger strenges Schichtverteilungsmuster aufweisen.

Nach der ersten Charakterisierung der transkallosalen Neuronenorganisation untersuchte Ich, wie diese Neurone, die zu einem fokalen SHT projizieren, zu verschiedenen Zeitpunkten nach der Verletzung betroffen sind. Ich habe GFPM-Mäuse verwendet, um Dendriten und deren Dornen von transkallosalen und nicht-transkallosalen Neuronen zu visualisieren und deren

strukturelle Integrität zu verschiedenen Zeitpunkten nach einer Verletzung zu untersuchen. Ich stelle signifikante und zeitabhängige Unterschiede in der Dichte und Morphologie der dendritischen Dornen zwischen Kontrollen und verletzten Mäusen fest. Bereits 7 Tage nach der Verletzung war die Dichte der dendritischen Dornen in transkallosalen Neuronen stark verringert. Interessanterweise wird die Dichte in nicht transkallosalen Neuronen durch das SHT nicht verändert. In Bezug auf die Form der dendritischen Dornen fande Ich nur für das apikale Segment der Dendriten eine morphologische Veränderung. Diese Ergebnisse deuten auf eine generelle Empfindlichkeit der transkallosalen Dornen für SHT-induzierte Schäden hin, bei denen der Verlust der Dornen (vorzugsweise reif) 1-2 Wochen nach der Verletzung stattfindet und sich 3-6 Wochen nach der Verletzung auflöst, was auf ein spätes Auftreten von Plastizitätsprozessen hindeutet.

Um weiter zu untersuchen, ob eine transkallosale Remodulierung nach dem SHT stattfindet, habe Ich den monotranssynaptischen retrograden SADΔG-FP (EnvA)-Tollwut-Virus verwendet. Auf diese Weise konnte Ich transkallosale Neuronen und ihre präsynaptischen Partner eindeutig identifizieren und einen Überblick über die präsynaptische Population in mehreren Hirnregionen und zu verschiedenen Zeitpunkten gewinnen. Diese Studie zeigt, dass die Plastizität der dendritischen Dornen nicht zu adaptiver Schaltungsplastizität mit Rekrutierung anderer Hirnregionen geführt hat, sondern dass die ursprünglichen Kreisläufe wiederhergestellt wurden.

Zusammengefasst habe ich in dieser Doktorarbeit die adaptiven plastischen Fähigkeiten von Neuronen mit axonalen Endungen in Gehirnverletzungen demonstriert. Ich glaube, dass dieses Wissen dazu beitragen kann, weitere kompensatorische plastische Mechanismen aufzuklären, die dann therapeutisch anvisiert werden könnten, um das Ergebnis nach einer Hirnverletzung zu verbessern.

Chapter 1: Introduction

1.1 Traumatic Brain Injury

1.1.1 Introduction and history of the disease

The human brain, a ~1.3 kg structure with its 10^{11} neurons and the 1 quadrillion synapses they form is unquestionably the most complex organ. The brain's importance is reflected by the enormous diversity of its tasks, from controlling our basic survival and behavior to enabling us exchange ideas and grasp the physical laws of the universe. The brain's power is even more greatly manifested by its ability to understand itself and its own evolution as well as to create new forms of intelligence. Yet, in spite of its significance and eminence, the brain is not invulnerable. On the contrary, the brain is very prone to intrinsic degeneration (as happens in Alzheimer's, Parkinson's, ALS and Huntington's disease), intrinsic injury (as happens in case of stroke) and extrinsic injury, with the latter being the focus of this study.

The definition of Traumatic Brain Injury, as most commonly found in the literature is "a disruption of normal brain function due to brain damage, caused by an external mechanical force" [1]. Disruption of normal brain function can manifest as absence or reduced levels of consciousness, difficulties with speech or sleep, sensory problems and cognitive issues such as memory, concentration deficits or mood swings. Mechanical forces causing TBI can be a direct impact, penetration, abrupt acceleration/deceleration or blast wave. The resulting damage involves disruptions in cerebral blood flow and abnormal pressure levels inside the skull and is usually detected using Computed Tomography (CT) scan or Magnetic Resonance Imaging (MRI).

Although such imaging techniques were not largely available before 1970, brain injury was not an unknown condition to ancient cultures. Scripts from Ancient Mesopotamia reveal knowledge of head injury and some of its results such as seizures, hemiparesis, aphasia and loss of vision or hearing. The Egyptian papyri of Edwin Smith (1650–1550 BC) presented an extensive characterization of 27 head injuries providing clinical symptomatology observations, but very little advice on possible treatment strategies [2] . Hippocrates, the famous Greek physician of 460BC-370BC recorded thoroughly his observations on head injuries, describing in detail the form of the intact cranium as well as 6 types of cranial fractures, their clinical outcomes and which of them required trepanation [3]. Not only did he understand the impact of elevated intracranial pressure but he also supported the idea that the brain is the origin of thought and

behavior [4]. Later on, the Alexandrian school further evolved the clinical evaluation of head trauma incidents setting the basis of what we today call the Glasgow Coma Scale [4]. In the Middle Ages and Renaissance trepanation was still the main intervention after head injury [5] and during that time the term *concussion* gained popularity [6]. Not until the18th century was intracranial pressure considered as the main cause of pathology post-TBI and only in the late 19th century was craniotomy suggested as typical treatment for reducing pressure [7].The medical definition of blast wave brain injury is a more recent development, since the frequency of such incidents increased in the past decades during wars. In addition to war-related blast wave injuries, the every-day use of cars and the increasing popularity of competitive sports have made TBI the leading cause of death and disability in young adults globally [8].

1.1.2 Epidemiology of TBI

Currently, TBI is an enormous socio-economic burden since it's the primary cause of coma worldwide [8] with about 10 million people being injured annually [9] and men being twice as likely to suffer from it as women [10]. Within Germany, the estimated annual number of brain injured patients is about 280,000 and 10,000 of them die as a direct or indirect consequence of their TBI [11]. According to the American Centre of Disease Control the incidence of TBI in the US is 2.8 million cases per year, with falls, transportation accidents, violence, sport injuries and explosive blasts constituting the most common causes of TBI. Children from 0 to 4 years old, older adolescents from 15 to 19 years old, and adults above 65 years old have higher rates of TBI hospitalization [12]. A European epidemiological study including data from 2012 for 24 countries identified 1.37 million hospital discharges and 33.415 deaths related to TBI, and showed that it was responsible for 37% of all injury-related deaths in the analyzed countries [13]. In Europe, TBI is responsible for the highest total number of years lived with disability and is thus a main contributor to injury-related medical costs [14] [15]. Besides causing disability, TBI is known to increase the risk for cognitive impairment and neuropsychiatric disorders. Patients surviving TBI are more vulnerable to dementia [16], Alzheimer's disease [17] [16] [18] and Parkinson's disease [19] as well as depression [20] [21] [22], anxiety and post-traumatic stress disorder [23] [24] and personality changes [24]. Therefore, the resulting psychiatric-related medical costs and psychological suffering add to the already immense socio-economic burden of TBI. However, the proportion of TBI-caused deaths is significantly reduced compared to 1970s [25] leaving more patients with life-long disability. Interestingly, the World Health Organization estimated that 70 -90% of head injuries receiving treatment are mild [26] in

agreement to another US study showing that only 10% of the TBI cases are moderate-severe [27]. The criteria for severity classification will be discussed in the following paragraph.

1.1.3 Classification of TBI

TBI is classified into 3 categories based on its severity: mild, moderate and severe, according to an international grading system called the Glascow Coma Scale (GCS) [28]. The GCS is comprised of three basic elements: the eye, verbal and motor response. The severity assessment is following the criteria described on Table 1. A total GCS score from 3 to 8 indicates severe TBI, a score between 9 and 12 suggests a moderate TBI while scores above 13 are considered indicators of only mild TBI.

Table 1

EYE RESPONSE	Score points
No eye opening	1
Eye opening as response to pain	2
Eye opening as response to speech	3
Spontaneous eye opening	4
VERBAL RESPONSE	
No sound production	1
Incomprehensible sounds	2
Incoherent speech	3
Confused, disoriented conversation	4
Normal conversation	5
MOTOR RESPONSE	
Complete absence of movement	1
Decerebrate response to pain (extension)	2
Decorticate response to pain (abnormal flexion)	3
Withdrawal as response to pain	4
Purposeful localization to painful stimuli	5
Performance of commanded movement	6

Although GCS is quite reliable for early prioritization of patients [27] it does not provide a perfectly accurate prediction of the underlying pathophysiology [29]. Another problem is the very short time window in which the test needs to be performed [30]. Moreover, the GCS is often not sensitive enough to detect mild TBI which is the most common type [31]. Therefore, the Department of Defense and Department of Veterans Affairs suggested a more complete grading version which besides the GCS elements contains the duration of post-traumatic amnesia (PTA) and loss of consciousness (LOC) as criteria [32].The use of more accurate classification criteria could improve the prediction of the TBI underlying pathophysiological mechanisms and facilitate the selection of an appropriate treatment.

Subsequently, TBI is further classified based on the mechanics of the injury. A closed TBI occurs when the skull remains intact and an open TBI when the skull is fractured or penetrated. In addition, TBI can be focal or diffuse depending on whether the injury occurs in a restricted part of the brain volume (i.e. cerebral contusion/ laceration, epidural/subdural/intra-parenchymal hematoma) or whether the injury is multifocal, spread throughout different brain regions (i.e. diffuse axonal injury, diffuse edema, hypoxic-ischemic injury) [7] [33] [34]. Focal brain damage is created by direct collision force on the head and the affected tissue is underneath the site of impact (coup) or at the opposite site (contra-coup) [35]. In focal injuries the damage is observable even by naked eye (macroscopic lesion) [36]. Common causes of diffuse TBI are acceleration/deceleration and rotational forces and diffuse injuries are hard to detect by eye or even imaging (microscopic lesion) [37]. Often, both focal and diffuse damage can be induced by a single injury and it is therefore not uncommon that a patient will have features of both types of injury [38]. Eventually, focal and diffuse damage can result in secondary pathology that may exacerbate neurologic dysfunction, as described in the following paragraph.

1.1.4 Pathophysiology of TBI

Primary and secondary injury are the terms used to differentiate between the initial damage which is the direct effect of the insult (tissue compression) and the following biochemical cascade of cellular and molecular processes which is the indirect result of the injury [33], respectively. Primary injury occurs immediately at the moment of the traumatic incident while secondary injury takes place minutes, hours and days after the primary injury [39]. Ischemia (inadequate blood flow) [40] [41], hypoxia (insufficient oxygenation) [42] [43], edema (swelling) [44] and increased intracranial pressure [7] are common secondary injury processes.

1.1.4.1 Excitotoxicity and Cell damage

As a consequence of injury-induced disruptions in blood flow and the resulting hypoxia in the affected brain tissue, there is a switch to anaerobic metabolism which is not energy efficient, resulting in the depletion of ATP and dysfunction of ion pumps on the cell membrane [45]. Subsequently, there is an abnormal cell membrane depolarization leading to disproportionate release of excitatory neurotransmitters, such as glutamate [46], and therefore NMDA and AMPA receptors become excessively activated, starting a vicious circle of events known as excititoxicity [47]. The resulting influx of Na+ and Ca2+ [48] initiates the activation of enzymes such as proteases [49] [50], endonucleases [51], phospholipases and lipid peroxidases [52].

These enzymes induce direct damage on several cell structures including cytoskeletal components, phospholipid membranes and the DNA itself. Moreover, the elevated Ca2+ levels and the aforementioned activated enzymes increase the production of free radicals and reactive oxygen species (ROS) [53] [54] further deteriorating the damage in the cell. In addition, mitochondrial function is significantly impaired due to the abnormal Ca2+ and ROS concentration levels [55] further contributing to elevated oxidative stress [56]. Ultimately, all these factors combined create a strong signaling for apoptosis or necrotic cell death [57] [58]. Unfortunately, not only grey matter but also white matter suffers secondary damage.

1.1.4.2 Axonal Damage

Severe injury of white matter has been detectable since 1960's in patients with closed TBI, including damage in the corpus callosum and cerebral peduncles. Degeneration of the white matter in long-survivors occurs even in absence of focal lesions and is defined clinically as diffuse axonal injury (DAI) [59]. More recently, atrophy within the corpus callosum was found in 63%-86% of severe TBI patients at 5 months and 20 months post- TBI, as revealed by MRI scanning [60]. Several studies showed that axonal damage is a predominantly common outcome of rotational head injuries [34], [61], [62].This further supported the idea that rotational acceleration of the head induces shear stress that stretches/ tears the axons at the moment of injury, which subsequently experience secondary degeneration. The underpinnings of axonal pathology have been extensively investigated by Povlishock [63] [64] and all of his studies detected axonal swelling due to disrupted axoplasmic transport along the extent of the axons. The mechanical forces during the injury either directly disrupt the axoplasmic cytoskeletal components or create a higher axolemmal permeability that makes the axons prone to Ca2+ influx. As a consequence, protease pathways become activated and break down the local cytoskeletal network inside the axon [65]. This in turn, impairs the local axonal transport leading to organelle and vesicle accumulation and increased axonal swelling. The swelling has been shown to happen not immediately after injury but rather gradually: Axonal swelling is reported to peak at 2 to 6 hours post-injury in animal models [66] and at 3 to 12 hours post-injury in humans [63]. Swollen axons may then either undergo the later stages of Wallerian degeneration, leading to a phase of irreversible axon fragmentation or remain swollen for days and recover spontaneously [67]. In case of complete Wallerian degeneration, disconnection usually occurs at 12h post-injury in human patients [68]. However, DAI doesn't always manifest as swelling, which is the case when a conversion of anterograde to retrograde transport takes place that blocks the occurrence of swelling. In such an occasion, DAI can be detected by the

accumulation of β-amyloid precursor protein at the axotomy site. Moreover, non-myelinated axons are more prone to secondary injury [69] [70] and in myelinated axons the initial segment, which lacks myelin, is also more susceptible to axotomy [71]. Interestingly, it has been shown in animal models of TBI that axonal injury (whether it is followed by complete axonal fragmentation or not) does not necessarily induce death of the corresponding neuronal cell body [72] [73]. Inflammation however, is a TBI-induced process that promotes both cell death and axonal damage.

1.1.4.3 Inflammatory response

The thorough clinical and preclinical TBI research of the past decades has pinpointed neuro-inflammation as a main contributor of secondary damage cascade following TBI [74]. TBI-caused inflammation implicates microglial activation, infiltration of circulating neutrophils, lymphocytes and monocytes into the CNS, upregulated secretion of mediators such as cytokines, chemokines and complement proteins by both resident neurons, astrocytes and microglia [75] [76].

Microglia, the brain's resident immune cells that constitute 10–12% of the CNS cell population respond rapidly to immune threat or CNS injury, for instance they have been detected in autopsy 2–10 days following severe TBI [77]. The responses to injury comprise phagocytosis, debris scavenging, angiogenesis, and wound healing. For example, when spinal cord is injured microglia react by phagocytizing damaged myelin, stimulating other immune cells, and eliminating synapses from damaged axons [78]. Classic M1 (pro-inflammatory) and alternative M2 (anti-inflammatory) microglia is present acutely after injury contributing to tissue damage and repair [79] [80], respectively. Therefore, acute TBI-induced microglia activity can be pro-inflammatory and neuroprotective. However, if inflammation is persistent in long-term after injury, the prolonged M1-related microglial response may be detrimental for recovery by promoting lesion volume expansion and cell death [81] [82].

The levels of pro-inflammatory cytokines such as IL-1 and IL-6, as well as tumor necrosis factor α (TNF-α) elevate within hours after the injury [83] [84]. IL-1 is crucial in initiating the immune response and induces neuronal damage together with stimulating chemokine secretion [85], whereas, blocking of IL-1 following TBI has beneficial effects in rats [86]. On the other hand, IL-6 favors improvement after injury [87] [88]. TNF-α which is in principle released by activated microglia as a result of injury has a quite controversial role that depends on the time- window following TBI: Shortly, at an acute post-TBI phase TNF-α mediates the immune response, but later acts as neurotrophic factor that is essential for repair [89].

Chemokines such as IL-8, released by astrocytes, can recruit leucocytes and have been considered to promote secondary injury processes [90]. With regards to the complement cascade, several animal and human studies have demonstrated complement cascade activation as a consequence of TBI [91] [92] [93]. This activation has been reported to increase cell death and aggravate secondary damage [94] [95].

The secondary injury-related pathological processes described above could be responsible for the reported deterioration of 40% of TBI patients after hospitalization [27]. Neuronal populations that survived the primary injury might die due to secondary injury complications and this could have a detrimental effect on the neurological outcome following TBI [96]. Although scientists have gained significant insight into the pathophysiology of secondary damage they still haven't fully unraveled the complex molecular interactions involved [97] and hence there is no successful Phase III clinical trial of a therapy and no FDA-approved treatment for mitigating the outcomes of TBI up to date [98] [99] [100] [101].

1.1.5 Animal Models of TBI

Animal models of human disease are invaluable tools for understanding the causal mechanisms and pathophysiology of disease, enable hypothesis testing, and perform experiments to evaluate potential diagnostic and therapeutic approaches that would be infeasible or unethical in humans. Different animal models of TBI have been developed, mimicking the different types of injury. Several models are replicating the focal injuries induced by impact, such as the penetrating TBI model [102], the weight drop model [103], the fluid percussion injury model [104] and the controlled cortical Impact model. Other TBI models are focused on mimicking the diffuse injuries caused by impact-caused acceleration/deceleration forces, such as the impact acceleration model [105]. Additionally, there are models for diffuse injuries in absence of impact such as the rotational TBI model [34] and various blast models, such as the open field exposure [106], blast tube [107] and shock tube models [108]. Lastly, there are models that combine different types of injury, like the Closed Head Impact Model of Engineered Rotational Acceleration (CHIMERA) [109] and other models that don't belong to any of these categories, for example the cryogenic injury model [110] and a model of acute subdural hematoma [111]. To sum up, there is a large variety of TBI models, designed to imitate different features of the

injury. The present study is based on the CCI model which will be described in detail in the next paragraph.

1.1.5.1 Controlled cortical impact model

The CCI injury is generated by a pneumatic impact device which drives a steel impactor tip onto the exposed by craniotomy, undamaged dura of an anesthetized animal. The craniotomy is most often unilateral, with location between bregma and lambda. CCI has been used mostly in rats and mice but also swine [112] [113]. Mechanical properties such as the speed, duration and depth of impact can be easily controlled and adjusted, providing the ability to induce different degrees of damage, from mild to moderate and severe focal injury. This is one of the factors that make CCI very practical and popular.

This model mimics many clinical features of the human TBI such as concussion, loss of ipsilateral cortical tissue, subdural hematoma, extensive reactive gliosis, axonal injury, blood–brain barrier (BBB) dysfunction, and in some cases coma [114] [115] [116] [117]. There is a strong correlation between the level of cortical deformation and the histological damage to the brain [118] [119] as well as the resulting behavioral deficits [86] [120]. Behavioral deficits such as memory impairments detected by the Morris water maze test are significantly related to the depth of deformation and the speed of the impact in mice and rats [121] [122]. The cognitive problems are observed as early as 2 days [114] up to a year post CCI and correlate with brain atrophy [123] [124] and cerebral blood flow restriction [125]. CCI also causes deficits in emotional behavior, assessed using the forced swim test and elevated-plus maze test in mice [125].

There has been a debate on whether the small diameter impactor tip is efficient in creating a wide and extensive brain injury such as diffuse axonal injury, besides focal injury. To answer that, a larger diameter (5mm) impactor was implemented and its effects on behavior were studied: The larger tip induced significant neurological impairments including cognitive dysfunction, lower scores in the Rotarod test and higher latencies in the water maze test [126]. Therefore, for studies aiming to resemble the diffuse injury aspects, increasing the impactor size would be a good option for creating a more relevant model [127].

Another modified version of the CCI model was developed to mimic mild, repetitive closed head injuries like the ones occurring in competitive sports such as football. This version utilizes the same device but with an impactor tip of larger diameter (~7 mm) implemented with a softer plastic cover to ensure blunt impact. The impactor is driven directly on the skull, without craniotomy and the procedure can be repeated several times using various time intervals. This

model has demonstrated acute neuronal degeneration and gliosis accompanied by motor and memory deficits [128].

In conclusion, the CCI model's practicality, its reliability in replicating the features of clinical TBI and its broad use make it a great candidate for studying TBI. Thus, CCI is the model that was selected for my study and will be further discussed in this thesis.

The extensive implementation of reliable animal models in TBI research has allowed not only for testing the safety and efficiency of potential therapeutic treatment procedures and compounds but also for investigating whether the brain possesses innate ability for recovery, independently of exogenous therapeutic interventions. As possibly positive evidence for the latter, mild to moderate TBI patients are able to regain simple motor functions such as grip strength and finger tapping [129], which indicates that some compensatory mechanism is present to trigger recovery.

1.1.6 Brain's innate repair ability

According to Santiago Ramón y Cajal the brain possesses an intrinsic capacity to remodel, a concept later called restorative plasticity [130]. Some of the restorative mechanisms the brain bears are neurogenesis, synaptogenesis and axonal remodeling. A large amount of research has been dedicated to understanding and describing in detail these intrinsic repair processes after unilateral, focal damage by TBI or stroke. Especially stroke research has gained important insight regarding damage-induced plasticity and is extremely relevant to TBI: Stroke is a form of acquired brain injury, although non-traumatic and coming from inside, or is frequently caused by TBI [131] and has therefore many commonalities with TBI including the clinical outcome, pathophysiology and underlying mechanisms. Thus, it would be very worthwhile not to overlook the crucial findings of stroke studies regarding remodeling and functional recovery.

Back in 1914 von Monakow suggested that impairments induced by focal brain damage are a result of the disorganization of local and distal functionally interconnected neuronal populations. According to his "diaschisis" theory, brain injury generates a suppression of function in areas that are adjacent or distant but functionally connected to the primary region of injury but this diaschisis dissipates over time allowing for recovery [132] [133]. However, today it is broadly accepted that functional recovery can emerge not only due to dissipation processes but also due to remodeling mechanisms [134]. Recovery of an impaired function after stroke/traumatic injury can be mediated by spontaneous/ experience-driven remodeling of neuronal circuits that were involved in the function before (vicariation process, proposed by Ogden and Franz in

1917) or recruitment of new neural networks (compensation/substitution process, as described by Munk in 1881 [134] [135]). Subsequently, a key question is raised: Does remodeling occur in the spared perilesional tissue, invoking functional recovery after damage? Does remodeling also involve the contralesional, intact hemisphere and how does it influence functional recovery?

1.1.6.1 Remodeling in the ipsilateral (lesioned) cortex

In agreement with the diaschisis theory, several CCI studies found that CCI leads to degeneration of axonal [118] [136] and dendritic [137] cytoskeletal structures that extends rostro-caudally beyond the injury surroundings. Hall et al., showed that the number of affected axons increases throughout the first week post-CCI [118] in agreement to the observations of Chen et al., who demonstrated extensive axonal swelling and disconnection on day 7 post-CCI [138]. Moreover, various TBI studies have reported a significant loss of dendritic spines at the ipsilateral cortex and hippocampus [139] [140] [141] [142] as early as 24h post-TBI [143]. However, indicatively of dissipation, spine density increased 1 week after TBI. Interestingly, the increase was higher than control levels, suggesting there might be also remodeling processes involved [143]. Besides structural changes that suggest loss of function, suppression of cortical neuron responses has been observed at the first 24h after open [144] [145] and closed- skull [146] [147] TBI. However, this initial hypo-excitation is followed by hyper-excitation, more prominently in case of closed skull TBI [146] [147] [100] but also in studies of open skull TBI [148] [144]. Similar findings have been published in stroke research: The immediate response to cerebral ischemia is the loss of spines [149] and spine reduction has been detected as early as 2 hours after middle carotid artery occlusion (MCAO) in the ischemic area and penumbra [150]. This initial synaptic decline is considered to be transient and might be a compensatory mechanism to balance oxygen consumption for preserving neuronal structural integrity [149].

On the other hand, there is accumulating evidence supporting that in general, stroke-related damage increases excitatory neurotransmission [151] [152] and reduces inhibitory neurotransmission [153] [154] [155] [156] in local, perilesional connections. This creates hyper-excitability [157] [100] that peaks at 7 days and then declines but persists for at least a month post-stroke [158] [159]. TBI studies have also displayed an early increase in excitatory neurotransmission in the rat cortex [160] and extracellular glutamate levels are elevated in humans 24-h post-TBI [161] [162] According to another CCI study, increased glutamate responses peak at the area surrounding the injury and spread through deep cortical layers, while GABAergic activity is significantly and globally reduced in the cortex after CCI [163].

These results suggest that after stroke and TBI, the elevated excitatory activity is enhanced by the loss of GABAergic control, contributing to post-injury epileptiform activity. In terms of anatomical changes, ischemic lesions stimulate sprouting of axons within local ipsilesional cortical projections [164] [165] and TBI induces axonal sprouting [166] [167] in the ipsilesional cortex proximal to the injury site, up to 2 weeks after CCI [168]. In contrast to many aforementioned TBI studies reporting dendritic spine reductions after injury, other TBI studies have found increased synaptogenesis in cortex and hippocampus [169], especially when combined with enthorinal cortex lesions [170] [171]. In the same vein, stroke studies that looked at structural changes in dendrites of ipsilesional cortical neurons showed that stroke increased spine formation on apical dendrites of Layer V neurons in the peri-infarct region [172] and the elevated spine formation was present for up to five weeks [173]. The total dendritic branch length did not change but dendrites with orientation towards the damaged tissue showed a tendency to retract while the opposite was observed for dendrites oriented away from the infarct [174]. These findings might explain why an increase in ipsilesional cortical thickness has been reported in the ventral postcentral gyri of chronic stroke patients [175]. Nevertheless, a direct association between such morphological alterations and functional responses in the remodeled area has not yet been fully established.

With regards to damage-induced functional changes, evidence for remodeling comes mainly from stroke studies: perilesional remapping has been exhibited by several studies [176] [177] [178] [179] [173] and is based on altered distribution of neuronal receptive fields (RF). Electrophysiological recordings displayed an expansion of cutaneous RF [180] [181] already detectable a few hours after infarction in the primary sensorimotor area, indicating an immediate unmasking of excitatory connections that were previously not expressed [181]. According to the study of Winship and Murphy [179], responsiveness of cortical neurons became broader one month after stroke but returned to normal two months post-stroke, suggesting a synaptic input segregation mechanism over time.

Moreover, several studies showed that local remodeling is an adaptive procedure, promoting restoration of the lost function in mice, rats and monkeys [182] [183] [184] [173] [177].

To sum up, significant synaptic changes in the ipsilateral hemisphere have been reported as a result of focal brain damage, including both dendritic spine reduction and suppression of activity as well as spine gain and increased excitation. These events seem to be time-dependent: There is an initial synaptic loss that is followed by spine recovery and hyper-excitability. The ipsilateral hyper-excitability may be beneficial for recovery if it is not persistent.

1.1.6.2 Remodeling in the contralateral (intact) hemisphere

The effect of unilateral focal brain damage on the intact hemisphere's plasticity is still under debate. Some studies have found no change in dendritic spine numbers at the contralateral cortex [141] or hippocampus [158] after TBI, while another found 25% spine reduction in the contralateral cortex and 23% reduction in the contralateral hippocampus [140].

On the contrary, a number of stroke studies have shown lesion- induced morphological changes in the intact hemisphere that are suggestive of plasticity. A higher dendritic arborization of layer V pyramidal neurons in the intact homotopic cortex was observed in rats after stroke up to 18 days post-lesion, followed by pruning of dendritic processes [185]. Moreover, a transient increase in the turnover rate of mushroom synaptic spines, which are normally stable, was detected at 7days after stroke while the mushroom spine density did not change, indicating plasticity [186]. In agreement to these findings, Schaecther et al [175] observed higher cortical thickness in the contralesional hemisphere (ventral post-central gyrus, area 1) of stroke patients.

In animal models of stroke, the intact cortical hemisphere displays elevated excitability similar to what has been observed in the ipsilateral cortical region surrounding the infarct [187] [188] [189] [186]. The contralesional hyper-excitability has been attributed to impaired inhibition from the affected homologous cortex [190] [151] as well as to elevation of excitatory neurotransmission [189]. It is though important to note that these similar excitatory changes develop with a different time-course in ipsilesional and contralesional areas [189].

The hyper-excitability and structural changes identified in the intact homologous cortex seem to translate to remapping and changes in representation of both the non-affected [180] [191] [192] and affected limbs [177] [186] [192]. Interestingly, considering the mechanism underlying the expansion of non-affected limb representation Mohajerani et al., [192] showed that mice without a corpus callosum also exhibit this effect after focal stroke, suggesting that the observed modifications are not mediated by transcallosal but subcortical interhemispheric projections. With regards to the reported expansion of affected limb representation in the contralesional cortex, it might indicate that disinhibition of the intact hemisphere results in strengthening of sub-threshold ipsilateral inputs from the affected limbs and this might provide some compensation for the loss of representation in the damaged cortex.

Whether the disinhibition and remodeling of the intact cortex is adaptive or detrimental for recovery of function remains controversial. There is compelling evidence supporting that recruitment of the contralesional cortex is positively contributing to recovery of the paretic limb [193] [194] [195]. However, the duration of the enhanced activity of the intact cortex is an important factor: Several studies claim that improved motor skill recovery is characterized by a gradual reduction in the initial hyper-excitability of intact cortex over the months after stroke [196] [197] [198] while others suggest that persistent over-activation of the intact hemisphere in chronic stroke patients enhances sensorimotor recovery [199] [200] [201] [202]. The latter findings are contradicting the popular interhemispheric competition model according to which, the hyper-excited contralesional hemisphere inhibits the ipsilesional hemisphere via the transcallosal neurons (Transcallosal Inhibition-TCI) [203] [204] [205] [206], thus adversely affecting sensorimotor recovery. A substantial part of trans-magnetic stimulation (TMS) research supports this theory [207] [202], including repeated-TMS (rTMS) studies showing that inhibition of the intact hemisphere improved motor performance of the paretic limb [208] [209] [210].

Until today, no major conclusions have been reached regarding the contribution of the intact hemisphere to functional recovery after focal lesion [211]. A potential interpretation would be that after brain damage, perilesional, remote and contralesional areas are immediately but shortly suppressed and then hyper-activated, providing some compensation. Over-activation of the intact hemisphere, may though be detrimental in long term by persistently inhibiting activity in the spared perilesional tissue and ipsilesional cortex [159]. A very crucial component that could be responsible for exerting this inhibition and may in various ways impact the activity and plasticity of the lesioned hemisphere is the population of transcallosal projection neurons (TPN). Investigating the time-dependent structural and synaptic changes at the contralateral cortex after TBI, with focus on the population of TPN, constitutes the main subject of this study.

1.1.7 Transcallosal Projection Neurons

The Corpus Callosum (CC) is an exclusive property of placental mammals, even serving as a means of distinguishing placentals from other mammals, as is the presence of placenta itself [212]. The CC, a bundle of commissural fibers just below the cortex is the biggest white matter formation of the human brain [213] [214] and its general function is to enable interhemispheric communication. The corpus callosum is quite non-homogeneous, meaning that distinct cortical areas are connected via fibers travelling through distinct callosal regions. For example, connection between anterior cortical areas is mediated by the anterior corpus callosum, and

more posterior areas are connected through the posterior corpus callosum. This topographic organization is more pronounced in primates [215], but less defined in rodents [216]. Although in primates there are regional differences in callosal fiber size, myelination and conductivity, such differences are less evident in other mammals, including rodents [216].

Transcallosal Projection Neurons (TPN) are mainly large pyramidal, excitatory cells whose myelinated axons comprise the corpus callosum, allowing integration of information between the two cortical hemispheres. According to early anatomical and electrophysiological studies, the majority of transcallosal neurons has been detected in layers II/III and layer V [217] [218].

TP neurons send their axons to the homotopic area of the contralateral cortex, therefore the location of a transcallosal neuron in the cortex determines the position of its axon terminal at the contralateral cortex [219] [213] [220]. Based on the rostro-caudal location of the regions the callosal axons connect, there is a broad classification of the corpus callosum in six regions: frontal, motor, somatosensory, auditory, temporal-parietal, and visual CC [220].

All TPN extend an axon to the contralateral cortex in a homotopic fashion but some TPN have and extra projection to another brain area (dual projection-TPN). Distinct subpopulations of TPN have been identified and classified based on the target area of their long-range dual axonal projections. Subpopulations of TPN extend dual projections rostrally to contralateral or ipsilateral frontal areas (referred to as forward projecting neurons or FPN), caudally to contralateral or/and ipsilateral primary somatosensory areas (backward projecting neurons or BPN) [221] and subcortically to contralateral or ipsilateral striatum (striatum projecting neurons or StrPNi) [222]. Dual-projection TPN are mainly located in the deeper cortical layers: In adult mice roughly 40% of layer V TPN send dual axonal projections to the frontal premotor cortex, which is the case for only 4% of layer II/III TPNs [221] and StrPNi are also almost exclusively found in layer Va [222]. Moreover, Layer II/III TPN form also local networks within individual cortical columns [223].

Interestingly, there are even more different types of transcallosal neurons besides those mentioned above. Transcallosal projection neurons that are non-pyramidal have been identified in the cat brain, comprising 10-32% of the non-pyramidal cell population at the area 17/18 border region [224]. A few years later Gonchar et al., [225] detected inhibitory, GABA-positive TPN in the rat neocortex, constituting 1% of all retrogradely labeled transcallosal neurons. A following study [226] found a similar proportion of GABAergic (GAD+) transcallosal neurons in the cat and rat brain (0.8% and 0.7% of all retrogradely-labelled TPN, respectively). More recent studies also reported the presence of sparse GABAergic CC fibers [227] and layer V (PV+) transcallosal neurons in the mouse brain [228]. In summary, TPN are quite diverse regarding

their location (upper or deeper layers), projections (single or dual with various target areas) and function (excitatory vs inhibitory), thus distinct populations can differentially influence the connection and integration between homologous areas of the two hemispheres.

The anatomical findings regarding the location and distribution of TPNs in the cortex have been based on retrograde tracing methods such as cortical injection of horseradish peroxidase (HRP) [229] [230] [226], lectin-conjugated colloidal gold [225] or Fluorescent Protein- expressing viruses [228] to label and study the cells of origin. In addition, anterograde tracing techniques such as cortical injection of biotinylated dextran amines (BDAs) [219] [213] [231] have been used to identify and inspect the TPN axonal terminals at the opposite hemisphere. Nevertheless, before the study of Chovsepian et al., [232] no systematic analysis of the TPN population using uniform methodology had been accomplished, that would enable comparing the organization of transcallosal connections between different functional regions of the mouse brain such as the primary motor and somatosensory cortex. Such a functionally segregated anatomical dissection of inter-hemispheric connectivity is crucial, considering that intrinsic or injury-related abnormalities in callosal projections can result in impaired connectivity, which is known to play a major role in autism and related disorders [233] [234] [235]. As discussed in the previous paragraphs, regarding plasticity after lesion, transcallosal neurons are essential for restoring the balance in interhemispheric activity [236] [237] and can be a key factor in functional recovery after focal brain damage. Therefore, understanding how distinct regional populations of transcallosal neurons are differentially affected by or reacting to damage in the area where their axon terminals reside, is of outmost importance for a TBI study. A necessary step to answer this question is to define and illustrate how transcallosal populations fluctuate over region across the mouse cortex, which was the first goal of my study [232]. Furthermore, studying the connectivity of transcallosal neurons and their integration in local circuitry is the following topic I am interested in.

1.1.8 Neuronal circuit reconstruction: Implementation of poly-trans-synaptic viral tracers

The previously described anterograde and retrograde tracing methods do not provide the ability to map synaptic connectivity, since the conventional tracers are incapable of moving trans-synaptically. For the purpose of studying connectivity, poly-trans-synaptic tracers of viral and non-viral nature have been developed. Non-viral tracers, such as plant-derived lectin and bacterial toxins have been used and despite their many advantages they lack synaptic specificity and their expression potential gets weaker with every synaptic step [238] [239]. Regarding the viral poly-trans-synaptic tracers there are two types of viruses that can infect

neurons mainly in retrograde direction: Herpes (double-strand DNA) and rabies (single-strand RNA) viruses [240]. Both virus types provide high infection efficiency and stronger expression with each synaptic step. However, a disadvantage of herpes virus is the lack of specificity as it doesn't spread exclusively through synapses, thus labeling adjoining neurons that may not be synaptically connected. On the contrary, the rabies virus (RABV) has been reported to spread only through synapses and explicitly in a retrograde fashion [241] [242] [243]. Although these poly-trans-synaptic viruses are very useful, it is difficult to infer how many synaptic jumps have been made at any given time and dissect precise pathways of neural connectivity. Poly-trans-synaptic viruses are efficient in tracing a circuit but distinction between first-order and higher-order connections remains a challenge [244]. In order to minimize this problem, Wickersham et al [244] developed a RABV tracer with a spread that can be restricted to one synaptic step (mono-trans-synaptic).

1.1.8.1 Mono-trans-synaptic Rabies Virus Tracing

Wickersham et al. utilized a deletion mutant RABV (SADΔG-FP) [245], lacking the expression of the RABV envelope glycoprotein (G), where the G- encoding gene is replaced by a coding sequence for a fluorescent protein (FP). The G protein is necessary for the assembly of infectious virus particles [245] and for mediating trans-synaptic transfer of the virus [245] [246]. Therefore, SADΔG-FP RABV can infect an initial population of cells (starter cell population) and replicate its viral core, expressing adequate levels of the fluorescent protein, but cannot travel through synapses and infect the pre-synaptic partners of the starter cell population, thus acting as a single-cycle tracer. The capacity of the SADΔG-FP RABV for trans-synaptic infection can be restored by selectively trans-complementing the starter cell population with exogenous expression of G. Since the G gene is not present in the trans-synaptically infected cell population (the pre-synaptic partners of starter cells), the virus is unable to spread beyond them. In that way, the infection is restricted to only first order connections (mono-trans-synaptic spread).

Moreover, restricting the infection of RABV to a specific cell population is crucial for precisely tracing a distinct neuronal circuit. In order to target the initial SADΔG-FP RABV infection to a defined starter cell population, Wickersham et al. [244] utilized the subgroup A avian sarcoma and leukosis virus receptor due to its high- specificity-interaction properties. The envelope protein of this virus (EnvA) can target viral infection exclusively into cells that express the analogous TvA viral receptor, which is present in birds but not mammals [247] [248] [249]. Therefore, according to Wickersham et al. [244], pseudotyping the RABV with EnvA enables the

restriction of infection to a particular population of neurons that are engineered to express the TvA receptor. The complete name of the resulting pseudotyped mutant virus is SADΔG-FP (EnvA) rabies virus. To sum up, SADΔG-FP (EnvA) RABV is a great tool for neuronal circuit tracing, allowing scientists to selectively study neuronal sub-populations of their choice and define their direct pre-synaptic connections. This meticulously designed viral tracer is utilized in the present study to exclusively infect transcallosal neurons and identify their presynaptic connections, revealing the first pre-synaptic step of the transcallosal circuitry, as illustrated in Scheme 1.
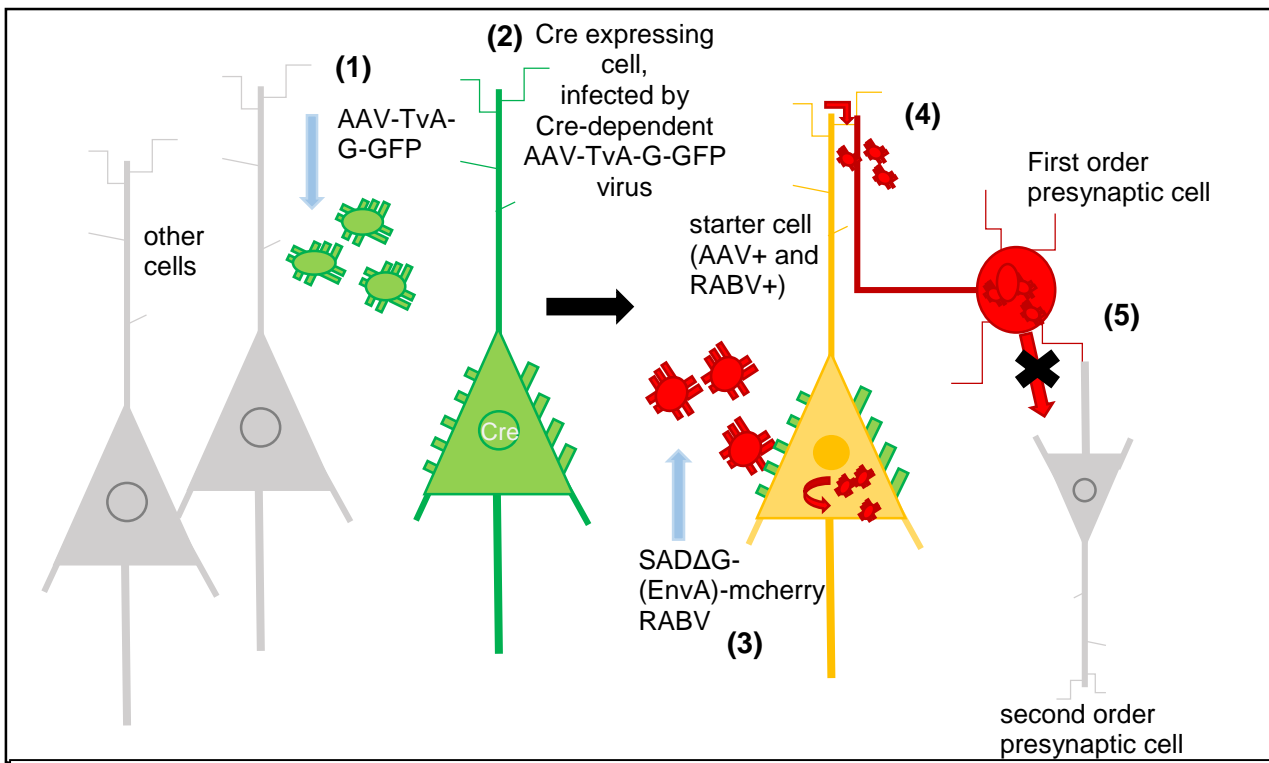
Scheme 1. Schematic representation of RABV mono-trans-synaptic tracing with initial restriction to a Cre-expressing (in this case Transcallosal) population of cells:

(1) Only the selected Cre-expressing neurons are infected with the injected AAV-TvA-G-GFP virus (green cells). **(2)** Following that, the majority of green cells are infected by the injected SADΔG-(EnvA)-mcherry RABV. Cells not expressing TvA (not green) cannot be infected by the SADΔG-(EnvA) RABV. **(3)** The population containing both viruses (starter cells) will be positive for both GFP and mcherry (yellow). Inside the starter cells, since the G protein is expressed, the RABV can replicate, assemble infectious viral particles and **(4)** transfer trans-synaptically to the first order presynaptic cells (red cells). **(5)** Having no G protein complementation in these cells, the RABV loses its trans-synaptic transfer ability. Therefore, the RABV labeling is restricted to the first-order presynaptic population (mono-trans-synaptic tracing).

1.2 Aim of the thesis

The overarching aim of my PhD thesis was to understand the remodeling capacities of anatomically connected contralateral areas following brain injury. For that purpose, it was important to specifically determine a cell population that would be anatomically connected to the brain injury- affected cortex. Transcallosal neurons that link the two cortical hemispheres were chosen to be studied in order to define the differential remodeling of an anatomically connected neuronal population following brain injury. To do so my thesis is divided in three separate aims:

Aim 1: The aim of the first project was to characterize the regional variability of transcallosal connections across the mouse cortex and answer the following questions: Are transcallosal neurons and their projections strictly homotopically organized and do they follow the same laminar distribution in different regions?

Aim 2: The aim of the second project was to investigate the effect of TBI (CCI) on the structural integrity (dendritic branching and spine density) of neurons at the intact cortex, focusing on the previously-studied population of transcallosal neurons, in a time-dependent manner (2, 7, 14, 21, 42 and 84 days post-injury)

Aim 3: The aim of the third project was to identify TBI-induced transcallosal circuit remodeling after reconstructing part of the transcallosal circuitry with the use of a monosynaptic rabies virus tracer.

Chapter 2: Materials and methods

2.1 Animals

32 female, six to twelve weeks-old C57/Bl6 mice (Janvier SAS) were used for the description of transcallosal neuron distribution across the mouse cortex. 39 male homozygous GFPM mice (The Jackson laboratory), six to twelve weeks-old were used for studying time-dependent effects of TBI on structural integrity of transcallosal neurons at the intact cortex. 37 female, six to twelve weeks-old C57/Bl6 mice were used for reconstruction of transcallosal neuron circuitry using rabies virus. All experiments were carried out according to the German guidelines on animal welfare and approved by local regulatory committees (''Aktenzeichen'' der Tierversuchsgenehmigung der Regierung von Oberbayern: 55.2-2532.Vet_02-15-135). Details on the animals' genetic background and their housing conditions are provided in Table 2.

Table 2

Mice	Vendor	Background/Origin
69 x C57BL/6JRj (Inbred)	Janvier SAS	CSAL (Orleans) - 1993 (F172)
39 x GFPM Tg(Thy1-EGFP)MJrs/J	The Jackson Laboratory	(C57BL/6J x CBA)F1
Housing conditions for all mice Premises: The rooms are designed as special livestock rooms (walls and ceilings are epoxy resin-coated, lighting via controllable artificial light, defined air exchange rate, filtered supply and exhaust air. Hygiene Rules: The mouse rooms of the Mouse Breeding Barrier and the Mouse Experimental Barrier can only be accessed by personnel after going through an air shower. Cages and enrichment enter the barriers sterilized. Radiation-sterilized food is fumigated into the barriers. Water is ultra-filtered, irradiated and acidified within the barriers from a special drinking water circulation system. Barrier system: The animal husbandry rooms are organized in closed barriers. The access to the barriers is limited for persons (mouse breeding barrier only animal keeper). Between the barriers there is a hygiene gradient (breed to experiment). Housing systems: Mice (breeding and experiment in general) are housed in individually ventilated cage systems (Techniplast, Type II long cages). To protect the animals from contamination, the cage systems are driven with overpressure. For the diversified design of the animal cages (Enrichment), game tunnels (which can also be gnawed), nestlets as nesting material and a mouse house (red plastic) are used in each cage. Climate: 22 +/- 2 ° C room temperature and 55 +/- 10% relative humidity are maintained in the animal husbandry rooms by the ventilation system. Radiation-sterilized food and sterilized water is provided ad libitum. Stocking density of cages: Occupancy is in accordance with EU Directive (2010/63)		

2.2 Surgical procedures

Anesthesia was induced by injecting of Midazolam (5.0 mg/kg bodyweight)/Medetomidine (0.5 mg/kg bodyweight)/Fentanyl (0, 05 mg/kg bodyweight) IP, in accordance with recommendations by the local animal welfare. Anesthesia was confirmed by the loss of pedal reflex. After surgery completion, mice were allowed to recover from anesthesia on a heating pad (38∘C) and orally received analgesic treatment with Metacam (0.05 mg/kg, Boehringer Ingelheim) up to 48 h post-surgery.

2.2.1 Tracer Injections

For all tracer injections, after fixation on the stereotaxic frame (World precision instruments, Germany), a small opening was drilled in the skull at the intended injection coordinates and then a glass capillary micropipette tip was slowly inserted into the brain through the opening. The pipette was removed at least 3 min. after the end of the injection to avoid backflow.

In order to label the axonal terminal fields of transcallosal neurons, I used the anterograde tracer BDA (1.5 µl, 10,000 MW; Life Technologies; [250]) which was injected with a finely pulled glass micropipette at −1.5 mm caudally from Bregma; 1.7 mm laterally from Bregma and in 0.3 mm depth to target layer II/ III or 0.6 mm depth to target layer V. To describe the location and distribution of transcallosal neurons, I labeled them by stereotactically injecting the retrograde tracer FluoroGold (0.5 µl of FG 1% in 0.1 M Cacodylate buffer, Fluorochrome LLC) in the primary motor cortex and the primary somatosensory cortex in and out of the barrel cortex area. More specifically, the following injection coordinates with respect to Bregma were selected: rostro-caudal +0.3 mm and −1.5 mm, lateral 1.3 mm, depth 0.3 mm; rostro-caudal +0.3 mm and −1.5 mm lateral 1.7 mm, depth 0.3 mm and rostrocaudal +0.3 mm and −1.5 mm, lateral 3.5 mm, depth 0.3 mm.

To study the time-dependent effects of TBI on structural integrity of transcallosal neurons at the intact cortex, transcallosal neurons were labelled by stereotactically injecting 0.3 µl of FluoroGold in the primary somatosensory cortex, trunk region, Layer II/III. The injection coordinates according to Bregma were the same for all mice: rostro-caudal −1.5 mm, lateral 1.7 mm, depth 0.3 mm. To retrogradely label Layer V CST projection neurons, as a control non-transcallosal population, laminectomy was performed at thoracic level 8 of the spinal cord and 0,5 µl of FluoroGold were stereotactically injected with a glass capillary into the right side of the spinal cord, 2 mm lateral from spinal midline at a depth 0.3 mm. Subsequently, the muscles and

skin were sutured with 3–0 Ethilon sutures (Ethicon USA, LLC) and saline was administered subcutaneously. Table 3 includes details on the tracers used in this part of the study.

Table 3

Tracers	Vendor	Catalogue number	Dilution
BDA 10,000 MW	Invitrogen	D-1956	undiluted
FluoroGold	Fluorochrome LLC	-	1% in 0.1 M Cacodylate buffer

The procedure for transcallosal circuit reconstruction started by retrogradely infecting transcallosal projection neurons via stereotactic injection of 0.5 µl of AAV1.hSyn.Cre.WPRE.hGH (titer: $5.048e^{13}$ vg/ml supplied by the Penn Vector Core; dilution 1:6 in 1x PBS) in the right primary somatosensory cortex, trunk region, Layer II/III. The injection coordinates according to Bregma were the same for all mice: rostro-caudal −1.5 mm, lateral 1.7 mm, depth 0.3 mm. The AAV-Cre retrogradely infected transcallosal population was then anterogradely labeled by injecting 0.5 µl of AAV1- synP-DIO-sTpEpB-eGFP (titer: $3.9 \times 10e^{12}$ GC/ml supplied by the Gene Therapy Vector Core, University of North Carolina; dilution 1:4 in 1x PBS), as described above. The injection was always performed at the left cortical hemisphere and the coordinates according to Bregma were the same for all mice: rostro-caudal −1.5 mm, lateral -1.7 mm, depth 0.3 mm. This virus is Cre-inducible and expresses the TvA and G protein selectively in the AAV-Cre infected transcallosal neurons. Finally, 1µl of SAD-ΔG-mcherry (EnvA) RABV (titer: 3×108 ffu/ml supplied by Prof- Karl-Klaus Conzelmann from Gene Center of the LMU; dilution 1:1 in 1x PBS) was injected as described above, in the left cortical hemisphere, at the same area where the AAV-TVA-G virus (rostro-caudal −1.5 mm, lateral 1.7 mm, depth 0.3 mm). This modified rabies virus can only infect the TvA-expressing transcallosal neurons. Because these neurons also express G protein, once the rabies infects them it can make a trans-synaptic jump to their direct pre-synaptic partners but not any further. As a result, the transcallosal neurons containing both AAV-TVA-G virus and RABV will display both red (mcherry) and green (eGFP) fluorescence (yellow, starter cells) and the direct pre-synaptic population will display only red (mcherry) fluorescence (red, presynaptic cells).

2.2.2 Induction of Trauma (Controlled Cortical Impact)

After fixation on the impactor's stereotaxic frame (Precision Systems & Instrumentation, LLC: see Table 4 for details) craniotomy was performed using a 0.3 mm tip drill over the right hemisphere starting from 0.2 mm up to 4mm from bregma epicenter on the mediolateral direction and up to 3mm caudally to bregma, creating a rectangular opening. The injury was inflicted by a TBI-0310 Impactor (Precision Systems & Instrumentation, LLC): the attached 3.0 mm beveled stainless steel tip piston was driven on the exposed brain through the rectangular opening with a velocity of ~6 m/s, impact duration of 150 ms, at depth of 0.5 mm. Immediately after the impact blood was cleared away from the injured tissue and the removed rectangular skull piece was glued back on its original place using Vetbond Tissue Adhesive (3M Animal Care, USA). Following that, the skin was sutured with 3–0 Ethilon sutures (Ethicon USA, LLC), saline was administered subcutaneously and *Temgesic*, (0.1 mg/kg, Schering-Plough) was administrated by Intraperitoneal injection upon recovery from anesthesia. The CCI took place five days after the injection of FluoroGold in the cortex or ten days after the injection of Fluorogold in the spinal cord.

In order to study the effects of TBI on contralateral transcallosal circuit remodeling using the rabies virus, the following injection and injury timelines were followed:

- **7d** TBI group

  (The 7d control group received no operation on day 14)

Injections:
AAV-Cre (lesion side)
AAV-TvA-G (contralateral side)

Rabies Injection (contralateral side)
CCI

Perfusion: 7 days
post TBI, n=9

Day 0   **Day 14 (CCI & Rabies)**   **Day 21**
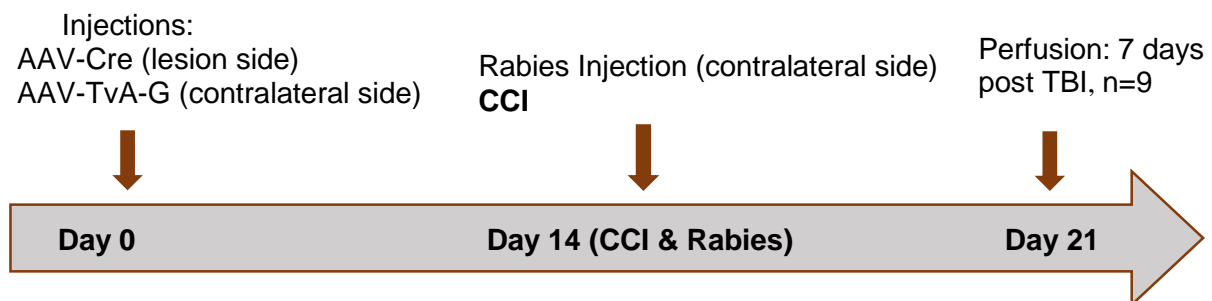
- **42d** TBI group

(The 42d control group received no operation on day 14)

| AAV-Cre injection (lesion side) | AAV-TvA-G injection (contralateral side) | Rabies injection (contralateral side) | Perfusion: 42 days post-TBI, n=10 |
| Day 0 | Day 14 (CCI) | Day 35 | Day 49 | Day 56 |
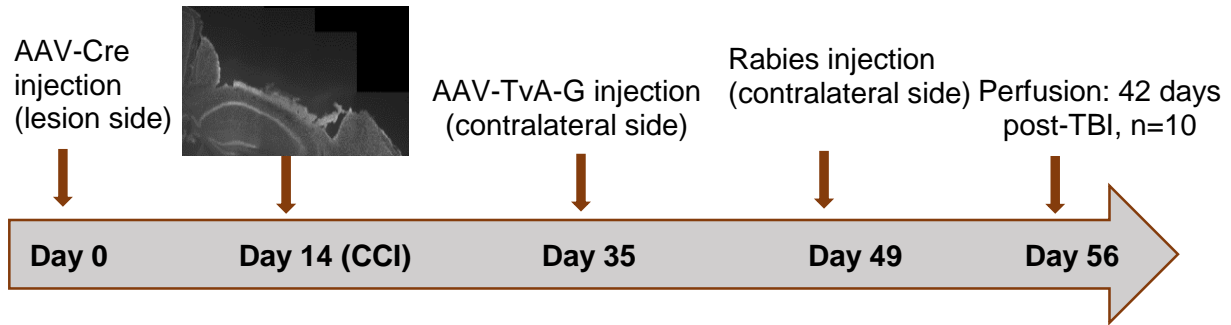
Table 4

Surgical equipment	Vendor	Website
Stereotaxic Frame, Single Manipulator for Mice	World precision instruments, Germany	https://www.wpiinc.com/502610-stereotaxic-frame-single-manipulator-for-mice-portable
TBI-0310 Impactor equipped with stereotaxic frame	Precision Systems & Instrumentation, LLC	http://www.presysin.com/Products/Head-Impactor.aspx

2.3 Tissue Preparation

All animals were deeply anesthetized with isoflurane and transcardially perfused with PBS-Heparin (1:500) solution followed by 4% paraformaldehyde (PFA, Sigma-Aldrich) in 0.1 M phosphate buffer. Brains were kept in the same fixative for 24 hours. Mice were perfused 10 days after the Fluorogold tracer injection to study the cortical distribution of TC neurons or 2/7/14/21/42/84 dpi to study TBI-induced structural changes and circuit remodeling. Brains were dissected and immersed in 3% low-melting-point agarose in order to acquire 100µm coronal sections using a Leica VT 1000s vibratome or incubated in 30% sucrose (Sigma-Aldrich) for 2-3 days (until sinking) and the tissue was then embedded in OCT (Sakura) and frozen at -20°C to be cut with a cryostat (Leica CM1850) in coronal plane, at a thickness of 60 µm.

2.4 Immunohistochemisrty

Neurotrace staining (for labeling all neurons in the study of transcallosal cell distribution): 100µm thick sections were washed 3 times with 1x PBS for 10 min. free-floating with NeuroTrace 435 (Invitrogen; 1:500 in 0.1% Triton-PBS) at 4◦C, overnight.

NeuN staining (for labeling all neurons in the study of TBI-structural changes): 100 µm thick sections were washed for 10min in 1x PBS three times followed by 1hour incubation in blocking buffer (1xPBS with 0,5% Triton and 10% goat serum [Invitrogen]) at room temperature. The

brain sections were then incubated overnight at 4° in the primary antibody solution: 1x PBS containing 0.1% Triton, 1% goat serum and mouse anti-NeuN Ab´ (1:500; Thermo Fischer Scientific). The next day the tissue was washed three times for 10min in 1x PBS -0.1% Triton before the application of the secondary antibody solution which contained 1x PBS -0.1% Triton, 1% goat serum and 1:500, goat anti-mouse AlexaFluor® 594 Ab´´(Thermo Fisher Scientific).

GFP-amplification + NeuroTrace staining (used in the circuit remodeling study) to reveal the TvA-GFP virus-transfected neurons and labeling all neurons, respectively: For free-floating anti-GFP staining, the sections were washed for 3x10min in 1x PBS, followed by 1hour incubation in blocking buffer (1xPBS with 0,5% Triton and 10% goat serum) at room temperature. The brain sections were then incubated overnight at 4° in the primary antibody solution: 1x PBS containing 0.1% Triton, 1% goat serum (Invitrogen) and 1:500 chicken anti-GFP Ab´ (Abcam). The next day the tissue was washed three times for 10min in 1x PBS -0.1% Triton before the application of the secondary antibody solution which contained 1x PBS -0.1% Triton, 1% goat serum and 1:500, Goat Anti-Chicken Alexa Fluor® 488 Ab´´(Abcam), as well as 1:500 NeuroTrace 435 (Invitrogen). In all cases, the day following the NeuroTrace or secondary antibody incubation, sections were re-washed three times in 1×PBS for 10 min and then carefully mounted on gelatin subbed slides, using VectaShield (Vector Laboratories) for coverslipping. Details on the equipment, chemicals, antibodies and viruses used can be found in Tables 5, 6, 7 and 8.

Table 5

Slicing equipment	Vendor	Website
Leica VT1000 S Vibratome	Leica Biosystems Germany	https://www.leicabiosystems.com/histology-equipment/sliding-and-vibrating-blade-microtomes/vibrating-blade-microtome/products/leica-vt1000-s/
Leica CM1850 cryostat	Leica Biosystems Germany	https://www.leicabiosystems.com/histology-equipment/cryostats/products/leica-cm1850/

Table 6

Chemicals	Vendor	Catalogue number	Dilution
Triton™ X-100	Sigma-Aldrich	X100-100ML	1:1000 in 1x PBS
Paraformaldehyde	Sigma-Aldrich	P6148-5KG	4% in 0.1M PB, pH~7.4
Sucrose	Sigma-Aldrich	S7903-1KG	30% in 1x PBS
Sakura Finetek™ Tissue-Tek™O.C.T.	Sakura, Fisher Scientific	4583	undiluted
VectaShield mounting medium	Vector Laboratories	H-1000	undiluted
Agarose	Sigma-Aldrich	A9539	3% in dH$_2$O

3M™Vetbond™ Tissue Adhesive	3M Animal Care, USA	https://www.3m.com/3M/en_US/company-us/all-3m-products/~/3M-Vetbond-Tissue-Adhesive/?N=5002385+3294397973&rt=rud	undiluted

Table 7

Antibodies, Serums, Stains	Vendor	Catalogue number	Dilution	Species
Normal Goat Serum	Invitrogen	10000C	3%	Goat
NeuN-AB (polyclonal)	Thermo Fisher Scientific	MAB377MI	1:500	mouse
Anti-GFP Antibody (polyclonal)	Abcam	ab13970	1:500	chicken
F(ab')2-Goat anti-Mouse IgG (H+L) Cross-Adsorbed Secondary Antibody, Alexa Fluor 594 (polyclonal)	Thermo Fisher Scientific	A-11020	1:500	goat
Goat Anti-Chicken IgY H&L (Alexa Fluor® 488) polyclonal	Abcam	ab150169	1:500	goat
NeuroTrace® 435/455 Blue Fluorescent Nissl Stain	Invitrogen	N21479	1:500	-

Table 8

Viruses	Vendor	Catalogue number	Dilution
AAV1.hSyn.Cre.WPRE.hGH 5.048e^{13} vg/ml	Penn Vector Core-Addgene	105553	1:6 in 1x PBS
AAV1- synP-DIO-sTpEpB-eGFP 3.9x10e^{12} GC/ml	Gene Therapy Vector Core	-	1:4 in 1x PBS
SAD-ΔG-mcherry (EnvA) RABV 3x108 ffu/ml	Prof- Karl-Klaus Conzelmann(Gene Center of the LMU)	-	1:1 in 1x PBS

2.5 Imaging

For the analysis of the homotopy and heterotopy of transcallosal neurons organization, retrogradely labeled transcallosal neurons were imaged with an FV1000 Olympus microscope with standard filter sets, using 10✕ objective, zoom 1✕ and resolution 1024 × 1024 and Kalman filtering. 10 µm of the total thickness were scanned in z-steps of 1 mm. Anterogradely labeled transcallosal axons and projections, were imaged with a Leica SP8 confocal microscope, using a 20✕ objective, zoom 1✕ and 1024 × 1024 resolution. Stacks of the total section thickness were acquired using 1.04 mm z-step size.

For the TBI lesion volume analysis I acquired 2D images of 26 sections per brain starting from Bregma 0.10 up to Bregma -2.5 with 100 µm distance between sections using the FV1000 Olympus microscope, a 4x Objective, resolution of 1024x1024 pixels and zoom 1✕.

For the evaluation of the cortical thickness, cell density and cell size at the contralateral cortex I acquired confocal stacks of 10µm of the total section thickness with a step size of 1µm using the FV1000 Olympus microscope. The images were taken with a 10× objective, zoom of 1× and resolution of 1024 × 1024 using Kalman filtering. Fluorogold labeling was imaged using the 405nm laser, GFP with 488 nm laser and NeuN with 543 nm laser, in sequential scans. For this analysis I scanned 4 brain sections per animal that were selected according to their distance from Bregma epicenter: section A (+0.7 mm from Bregma) section B (-0.7 mm from Bregma) section C (-1.7 mm from Bregma) and section D (-2.7 mm from Bregma). Transcallosal neurons were identified as Fluorogold and NeuN positive while non-transcallosal neurons were NeuN positive only. Complete reconstruction of the contralateral cortex was accomplished using the stitching plugin of the Fiji software [251].

For the dendritic branching and spine density/morphology analysis I took advantage of the intense and sparse labeling of Layer V cortical neurons provided by the GFPM mouse line. Transcallosal neurons were identified as GFP and Fluorogold positive, while GFP positive-Fluorogold negative neurons at the same area were considered non-transcallosal. In my CST-control group double positive neurons for Fluorogold and GFP were identified as CST projection neurons. For the dendritic branching analysis images of dendrites were acquired using the FV1000 Olympus microscope with 20x objective, zoom of 1×, 1024 × 1024 resolution and Kalman filtering. Following that, maximum z projections were generated from the 20x confocal stacks in Fiji [251]. In order to quantify the spine density/morphology of individual dendrites, the 60x objective, zoom of 3.5 and 800x800 resolution with Kalman were used. I obtained 3 images from each individual dendrite: A sample of the proximal segment (Layer V, at a distance of approximately 70-150 µm from soma), a sample of the distal segment (Layer II/III, at a distance of approximately 370-450 µm from soma) and a sample of the apical tuft segment (Layer I, at a distance of approximately 510-600µm from soma). The 60x magnification images for spine density/morphology analysis underwent deconvolution using the Huygens Essential software, v 15.10 (Scientific Volume Imaging, The Netherlands, http://svi.nl) [252] and z projections of the deconvoluted stacks were obtained using Neuron Studio (CNIC) [253].

To determine the presynaptic connectivity of transcallosal neurons following injury, I quantified the presynaptic neurons (m-cherry positive) and divided the counts with the total number of starter cells (m-cherry and GFP positive) in each brain. In order to image the starter cells, 6 sections per brain containing starter cells were imaged with Leica sp8 confocal microscope: 40 µm of each section were scanned with a step size of 1 µm using 20x magnification, zoom of 1

and 512x512 resolution with Kalman filter. Image stacks were processed using Fiji [251], 4 individual levels of which were used for quantification with an in-between distance of 13 µm. In order to image the presynaptic cells, 20 sections per brain were selected according to the Allen brain atlas (© 2011 Allen Institute for Brain Science. Allen Mouse Brain Reference Atlas. Available from: http://mouse.brain-map.org/static/atlas) starting from Allen level 44 (corresponding to roughly 1.15 mm distance from bregma, rostrally) up to Allen level 82 (corresponding to roughly 2.85 mm distance from bregma, caudally), and were imaged with Leica DM4 B microscope. The distance between two consecutive imaged sections was always approximately 200 µm. Using the Stereo Investigator software v 2017.03.2 (MBF Bioscience, Williston, VT USA), each complete section was scanned with a 2.5X objective. By sequentially applying different laser wavelengths I acquired images consisting of 3 channels: Blue channel displaying all neurons (NT435 staining), green channel displaying all AAV-TvA-G infected neurons (expressing GFP) and red channel displaying all the RABV infected neurons (expressing m-cherry). The resulting image quality was adequate for quantification of the areas with sparse labelling. The areas with denser labelling, due a large number of high-intensity m-cherry-positive cells, were additionally scanned with a 10x objective (again using the Leica DM4 B microscope) in order to achieve a better resolution. All acquired mages were processed in Fiji [251] and stitched using the pairwise stitching plugin provided in the software. Detailed list of microscopes used is included in Table 9.

Table 9

Microscopes	Vendor	Website
Stereotaxic Frame, Single Manipulator for Mice	World precision instruments, Germany	https://www.wpiinc.com/502610-stereotaxic-frame-single-manipulator-for-mice-portable
TBI-0310 Impactor	Precision Systems & Instrumentation, LLC	http://www.presysin.com/Products/Head-Impactor.aspx
Leica TCS SP8 Confocal microscope	Leica Microsystems, Germany	https://www.leica-microsystems.com/products/confocal-microscopes/p/leica-tcs-sp8/
Leica DM4 B microscope	Leica Biosystems Germany	https://www.leicabiosystems.com/clinical-microscopy-surgery-radiology/clinical-microscopy/routine-microscopy/dm4-b/
FV1000 Olympus microscope	Olympus	https://www.olympus-global.com/technology/museum/micro/2004/

2.6 Data Analysis

Quantification of BDA-labelled transcallosal axon distribution

The allocation of transcallosal axons in the cortical layers (contralateral to the BDA injection site) was quantified on 5 sections per brain. The sections were selected according to their rostro-caudal distance from the injection coordinate: section zero being at the center of injection (−1.5 mm from Bregma) and the two immediate sections rostral and caudal to section zero. The identification of cortical layers relied on the NeuroTrace staining. Using Fiji [251], the total area in which the terminal fields are localized was outlined across the full depth of the cortex and per each layer. Following that, I implemented the "measure tool" in Fiji [251] to calculate integrated densities for individual layers and across the entire cortical column (by definition, integrated density is the sum of the values of the pixels in a selected area and is therefore equivalent to the product of the area and Mean Gray Value in this area).To determine the percentage of terminal fields per layer, the Integrated intensity of each cortical layer was first calculated by the "measure tool" and then divided by the integrated intensity of the entire cortical column.

Quantification of Fluorogold-labeled transcallosal neuron distribution

The numbers and localization of transcallosal projection neurons in the cortical layers (contralateral to the FluoroGold injection site) were quantified on 5 sections per brain. The selection of the sections relied on their distance from the injection coordinate. First, the "section zero" determined as the section at the center of injection, which had the most intense labeling on the ipsilateral cortex. Thus, for injections caudal to Bregma I considered section zero as -1.5 mm from Bregma and for injections rostral to Bregma I considered section zero as +0.3 from Bregma. In addition to section 0, I imaged and quantified the two immediate sections rostral and caudal to section zero corresponding to the following coordinates: -2.1 mm, -1.8 mm, -1.2 mm, -0.9 mm from Bregma for the caudal injections and -0.7 mm, 0 mm, +0.3 mm, +0.6 mm, +0.9 mm from Bregma for the rostral injections, respectively. In all cases, only the cortex contralateral to the injected hemisphere was imaged and analyzed. Using Fiji [251], I generated maximum intensity projections of each stack for counting FG-labeled neurons. The quantification was performed manually, implementing the cell-counter plugin of Fiji [251]. To study the transcallosal neuron distribution in different parts of the cortex of a given coronal section I defined three separate areas according to their distance from section's midline: The homotopic area, HA (the center of HA was located at the same distance from the midline as the injection point), the lateral adjacent area (LAA) and medial adjacent area (MAA). All three areas had the same size

which was 1226 mm^2. TC neurons were counted separately in each area and related to the sum of TC neurons detected in all three areas (HA + LAA + MA) on a given section. In order to analyze the transcallosal neuron distribution in the different cortical layers, I used the NeuroTrace labeling to identify the layer borders. Then, the number of FG positive cells in a certain layer of a certain area was counted (HA, MAA or LAA) and was then related to the total number of FG positive cells found in the entire area.

Calculation of lesion volume

To calculate the lesion volume induced by Controlled Cortical Impact, consecutive sections of 100µm were used. The area of cortical tissue loss was manually outlined and measured for each section using Fiji [251]. For the calculation of lesion volume I implemented a previously described formula [254] : *Total lesion volume= [0.5A1 + 0.5(A1 + A2) +...+ 0.5(A_n − 1 + A_n) + 0.5An]` Y,* where A represents the lesion area (in mm^2) for each section, and Y is the distance (in mm) between 2 sections

Calculation of cortical thickness

To calculate the cortical thickness of sections A, B, C and D the distance between the bottom of Layer VI and top of Layer I was measured, using the straight line tool in Fiji [251], at three different points in the mediolateral direction (1 mm, 1.5mm and 2mm from midline) and these measurements were averaged for each section (fig. 1)
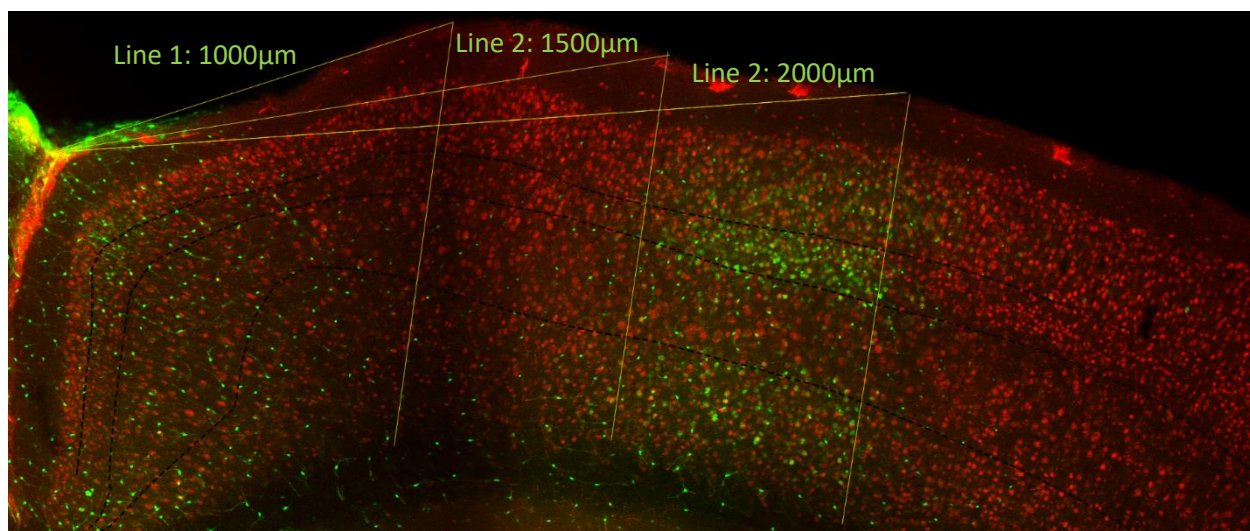
Figure 1. Example of cortical thickness calculation for one section. The distance between the end of layer VI (white arrow) and beginning of layer I (green arrow) was measured at three different points in the mediolateral direction (1000µm, 1.500µm and 2000µm from midline). These measurements were averaged for each section and sections A, B, C and D were analyzed per mouse, corresponding to +0.7, -0.7, -1.7 and -2.7 mm rostrocaudal distance from Bregma, respectively. Scale bar: 500 µm

Cell density and cell size calculation

Images containing the contralateral cortex from midline up to 2.00 mm lateral to midline including the NeuN and Fluorogold channels were processed and analyzed with the help of Mario Kreuzfeld using the Definiens Developer XD, Version 2.7.0. software. Application of a custom rule-set in this software enabled the automatic identification and differentiation between Fluorogold positive (transcallosal or TC) cells and Fluorogold negative (non-tanscallosal or NTC) cells, as shown in fig. 2, right panel. In brief, regions of interest (ROI) were drawn in manually and Fluorogold positivity inside the ROI was automatically quantified. NeuN positive cells within each ROI were then detected and quantified based on anti-NeuN antibody positivity. Each NeuN+ cell was also considered fluorogold positive only when the fluorogold signal intensity was at least 1.5 times above background level and above a minimum size cut-off value. The cell counts were then divided by the size of the ROI to obtain the cell density results. Information regarding the area size of each counted cell (in µm²) was also provided by the software for subsequent cell body size analysis.
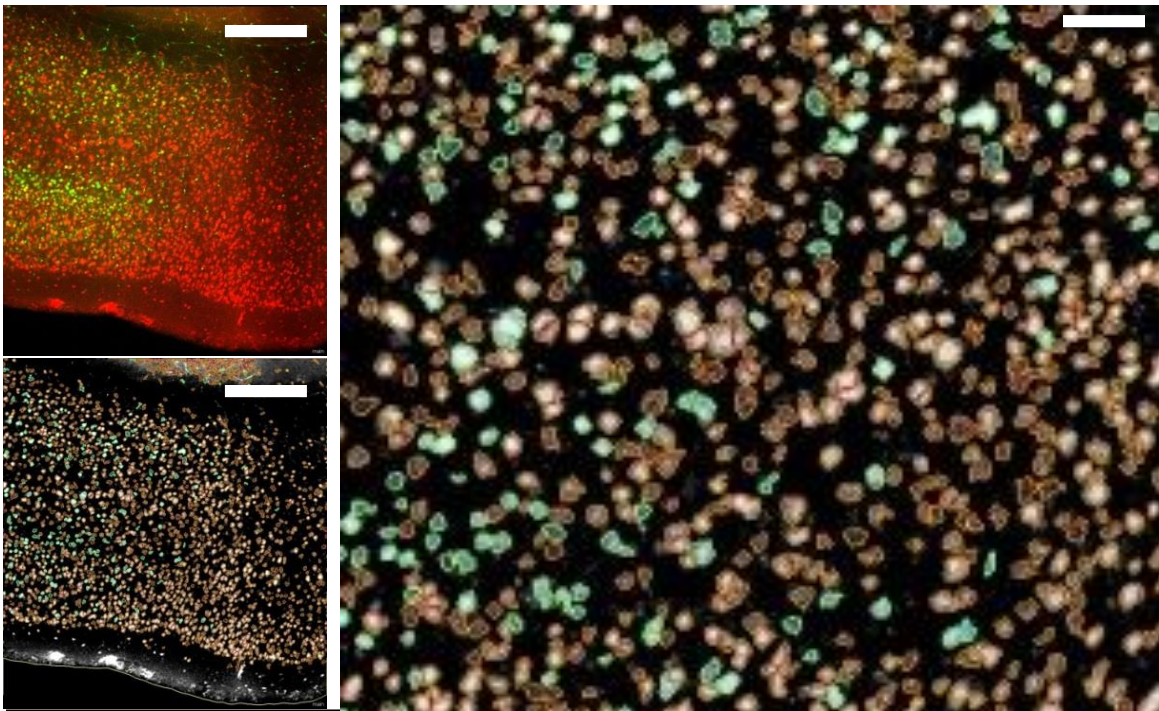
Figure 2. Original image to be quantified (upper). Same image after software processing (lower). Right: Closer view of the processed image, showing the recognized by the program Fluorogold and Neurotrace positive (TC) cells as green and the Fluorogold negative and NeuroTrace positive cells as red (non-TC cells). Scale bars (left): 500 µm, (right): 150 µm

Dendritic Arborization Quantification

In order to calculate the number of dendritic branches, the cell counter plugin in Fiji [251] was used through the confocal stack to count only branches emerging directly from the main apical dendritic trunk, as displayed in fig. 3. The length of each dendrite was measured using Neuron Studio (CNIC) [255] and then used for normalization (number of branches/μm).
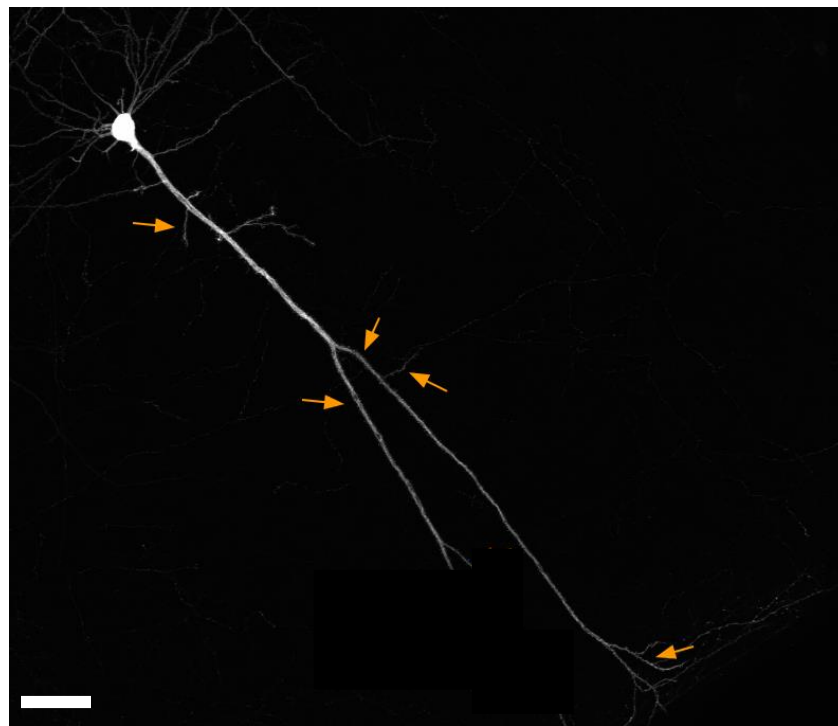
Figure 3. Example z-projection image of a Layer V GFP-expressing neuron's dendrite (20x magnification) used for quantification of dendritic branches. Yellow arrows show some of the branches that were counted. Scale bar: 100 μm

Spine Density and Morphology analysis

In short, each deconvoluted stack containing one proximal, distal or apical tuft dendritic segment (fig 4.A.) was opened in Neuron Studio (CNIC) [253] (fig 4.B.) and the dendritic trunk was semi-automatically traced resulting in a series of green vertices superimposed on volume-rendered data (fig4.C). Following that, the program detected and classified the dendritic spines in 3 categories according to their shape: Thin, stubby and mushroom [256] (fig 4.D) and the quantification was performed in 3D, marking spines in x, y and z axis (fig 5.A). Neuron studio (CNIC) provides the possibility to look at the marked spines in each axis separately and manually remove erroneously counted spines or add missing spines.
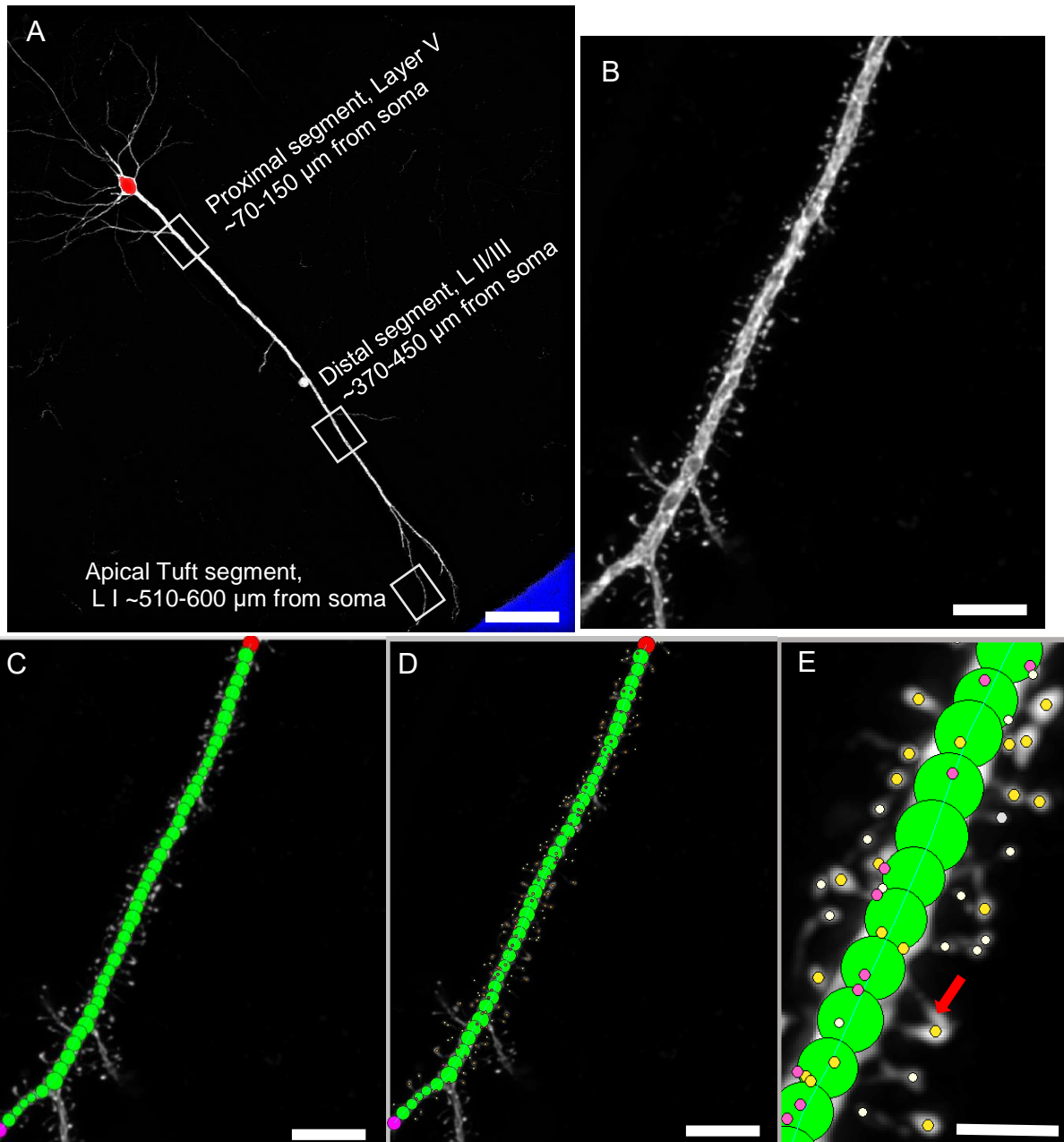
Figure 4. A. Illustration of dendritic segment selection for spine quantification. B. 60x image of a distal dendritic segment opened in Neuron Studio (CNIC) for quantification. C. Segment displayed in B with semi-automatic dendrite tracing. Red circle shows the beginning and magenta circle shows the end of the dendritic segment to be quantified. D. Same segment, with spines automatically quantified by the program and manually corrected by the user. E. Closer view of D, showing the stubby (pink), mushroom (yellow) and thin (white) spines as recognized and quantified by the program. Red arrow shows a spine that was not identified by the software but added later by the user. Scale bars (A):150 μm, (B, C, D): 10 μm, (E): 5 μm.
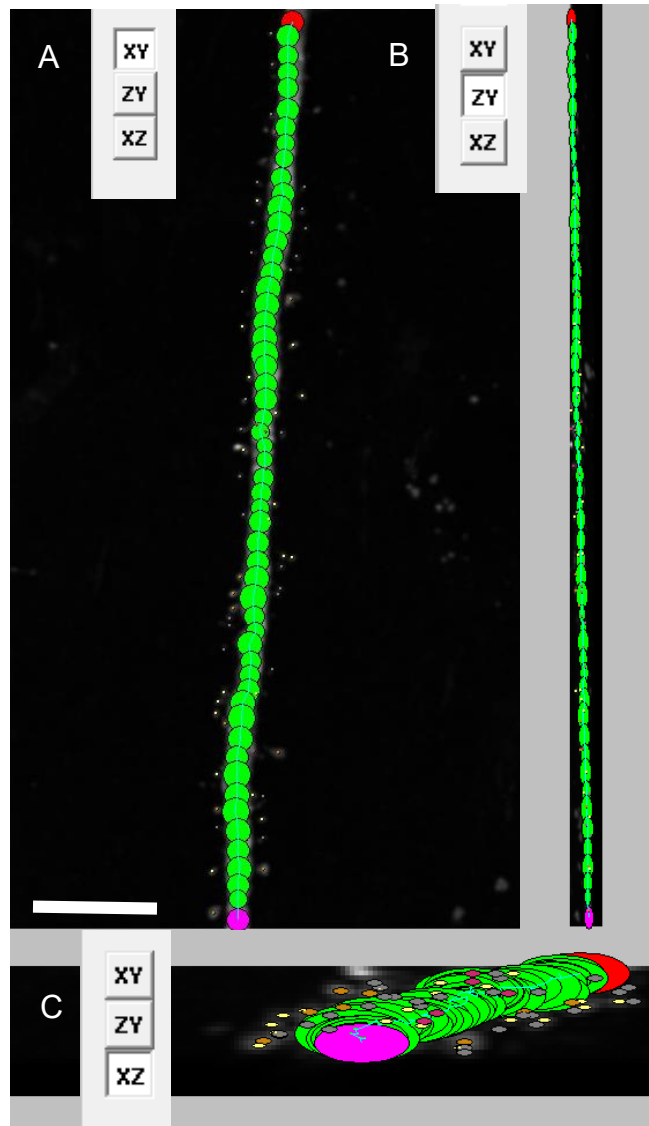
Figure 5. Illustration of dendritic segment quantification in 3 dimensions. A. XY view of the quantified segment. B. ZY view of the quantified segment C. XZ view of the quantified segment. Red circle shows the beginning and magenta circle shows the end of the dendritic segment to be quantified. Stubby spines are marked in pink, mushroom in yellow, thin in white and gray spines are those added by the user, before classification. Scale bar: 10 μm

Therefore, I examined every quantification for errors in x (fig 5. A), y (fig 5.B) and z (fig 5.C). Falsely detected spines were removed, falsely undetected spines (i.e. fig. 4 E) were added and misclassified spines were given their correct classification. The resulting numbers of spines were divided by the length of the dendritic segment as calculated by the program.

Interpolation of starter cells counts

Starter cells were identified as m-cherry and GFP positive and quantified using the cell counter plugin in Fiji [251]. Due to small but unavoidable variability between viral injections, the distribution of starter cells differed between mice. Therefore, the selected 6 sections did not always correspond to the same distance from bregma across mice. Thus, to more accurately estimate the number of starter cells in a brain, extrapolation of cell counts at certain points of distance from Bregma (which had not been imaged) was essential. The least biased approach was to fit the data points with a polynomial curve and then infer the values of the missing data points, according to the curve. This procedure is known as interpolation [257] and is very often used in biological studies. Interpolation makes the assumption that there is a function f(x) that passes through the data points and precisely depicts the value of interest at all non-data points, generating an artificial data set that represents the original data set in its entirety, including all the in-between values that were not actually quantified. The purpose of this procedure is to estimate a good fit to the original data points using an approximating function. In linear interpolation, the least complex form of interpolation, two original data points are connected through straight lines. The result of linear interpolation is quite indented and might not validly represent the original function. The best approach, when the data points are not expected to follow a linear trajectory, is to fit the data points with polynomial curves. The original data set of starter cells had six data points which were unevenly spaced. Therefore, in order to provide a "good fit" to the data, cubic spline interpolation was implemented. We call spline a special function defined piecewise by polynomials, while a cubic spline is a spline constructed using third degree polynomials to smooth curves through a set of data points. This system provides a curve with a continuous second derivative [258]. The function S_i, which is the cubic spline can be written as: $S_i(x) = a_i(x-x_i)^3 + b_i(x-x_i)^2 + c_i(x-x_i) + d_i$, where x ranges from x_i to x_i+1. The starter cell counts were interpolated using cubic splines in Python and the resulting curves seemed to give a realistic approximation of the original data (fig. 6). The total starter cell estimations were then acquired by extracting the number of cells at artificially inserted nodes, represented by x in fig. 6, and summing them all together for each brain. Importantly, the model assumes that the starter cell counts were zero beyond the range of the original data points. This method provided a comprehensive estimation of starter cells which were differentially distributed along the same range for every brain.
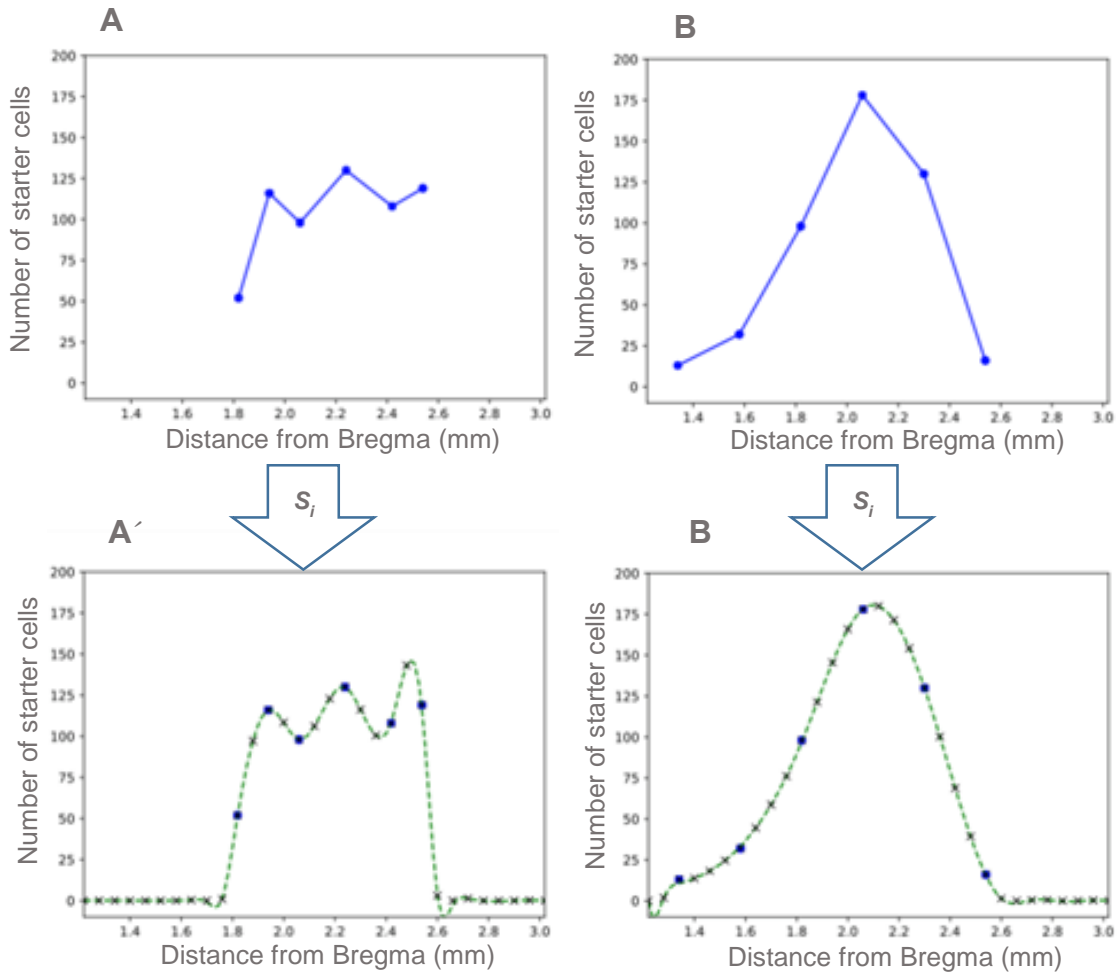
Figure 6. A, B. Example Original starter cell counts plotted as a function of the distance from the bregma. **A´, B´.** Interpolated starter cell counts plotted as function of distance form bregma, corresponding to A and B. The green curve is the fitted cubic spline function S_i. The blue dots represent the original data points and the x's represent the artificially interpolated data points. *Script in Python provided by Sanofer Abdul Salaam.*

Quantification of presynaptic cell population

The main quantitative goal was to obtain information about the number of presynaptic cells in distinct brain areas, in order to identify which regions are involved in potential remodeling. Therefore, the quantification on every imaged brain section was performed per area, and the areas were defined according to the corresponding coronal section of Allen brain atlas (© 2011 Allen Institute for Brain Science. Allen Mouse Brain Reference Atlas. Available from: http://mouse.brain-map.org/static/atlas, fig.7).
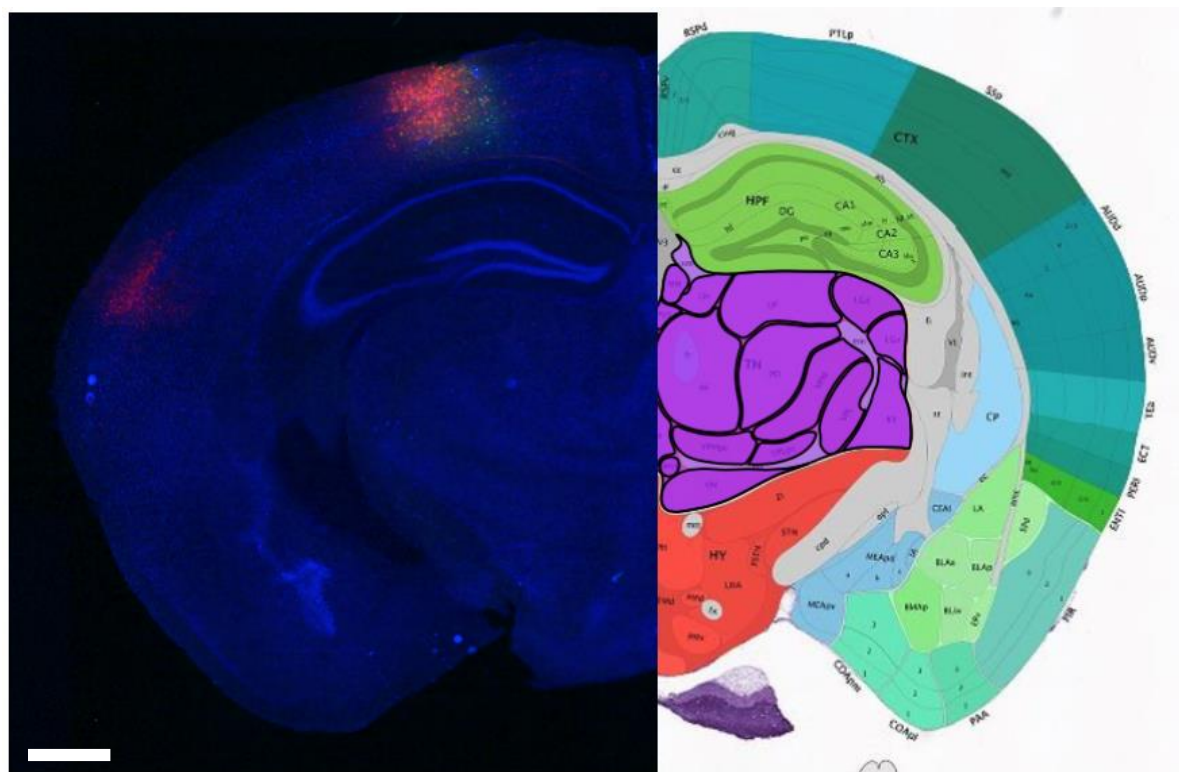
Figure 7. The stitched image of a brain section (left) is quantified by comparing it to the Allen brain atlas image (right: Image credit: Allen Institute) at the corresponding level and then defining areas accordingly. Scale bar: 500 µm.

The presynaptic cells (red) in each area were counted using the Cell Counter plugin and directly noted down in an Excel sheet. This method was sufficiently accurate for areas with not very dense labeling. However, in highly crowded areas such as the one shown in fig. 8, this method was not valid enough, as it was very difficult to physically differentiate the cells from one another. In this case, the higher magnification images (10x) were implemented, and a preprocessing procedure was performed to improve their quality. Fiji's [251] particle analyzer was then utilized for automatic quantification. Cells that were both red and green (starter cells)

were always subtracted from the counts as the goal of this part of the study was to exclusively quantify presynaptic cells.
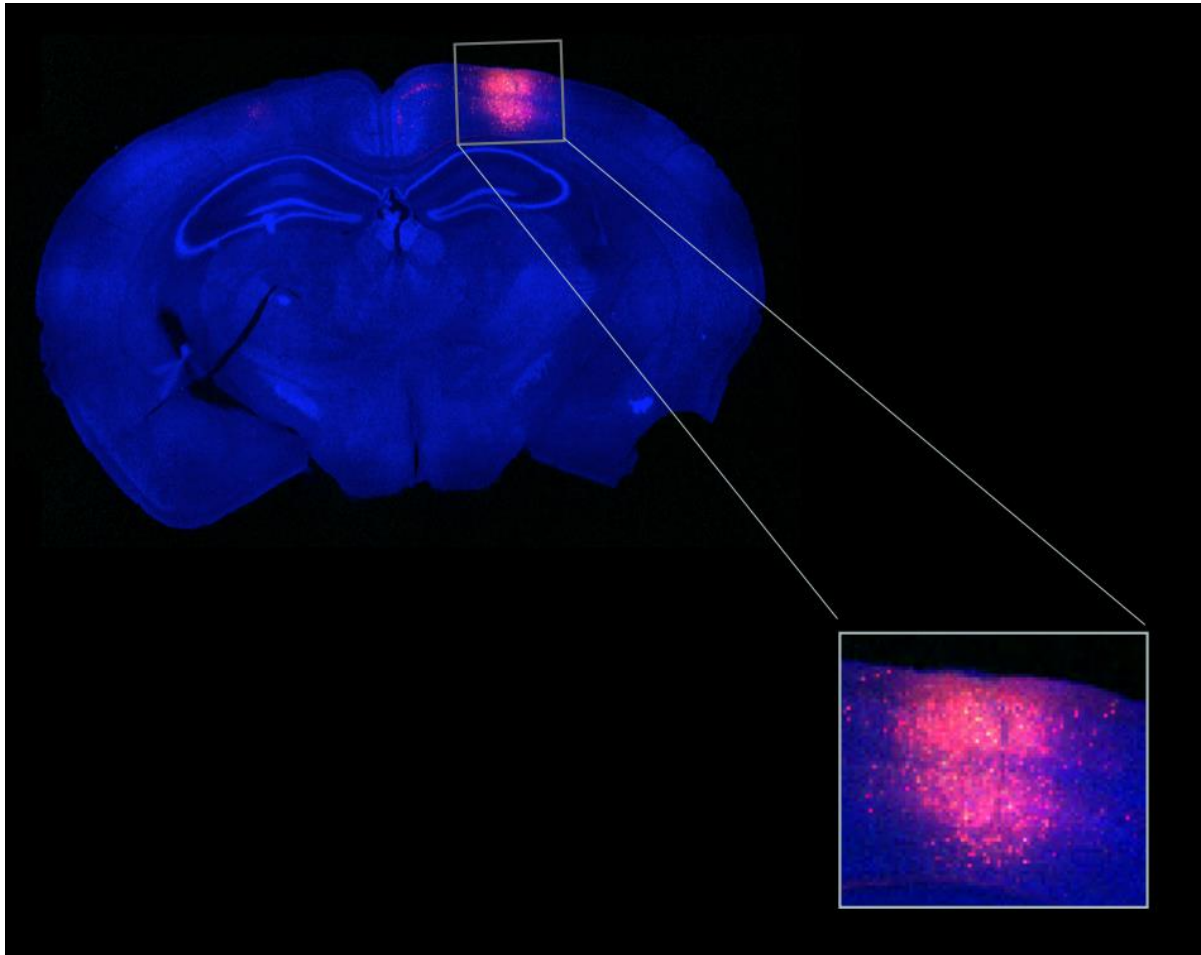
Figure 8. Example image for illustrating problems with manual quantification. The zoomed in portion shows that the cells look aggregated and it is impossible to physically isolate the cells for counting manually.

The image preprocessing started with subtraction of background, to get rid of potential noise (fig. 9):

1) The image was separated into the three channels (Image > Colors > Split Channels) and only the red channel image (displaying RABV positive cells) was used for further preprocessing.

2) The resulting one-channel image was then duplicated (Image > Duplicate).

3) The duplicated image underwent smoothing (Selection of duplicate > Process > Filter > Mean) The mean was set to a radius of 75 pixels, roughly 3 times more than cell diameter, in order to ensure that no cell will be eliminated by the following subtraction

4) The smoothed image was subtracted from the original red channel image (Process > Image calculator>Subtract).

5) As a result of the subtraction, an image with reduced noise and cell aggregation was generated. This improved image was again subjected to smoothing with a mean radius of 3 pixels (Process> Filter > Mean).

6) Regions of interest (ROI) were defined, outlining the exact area to be quantified and separate the cortical upper layers (L I-IV) from deeper layers (V-VI).

The preprocessed image was then adjusted for local contrast (Plugins > Integral Image Filters > Adjust Local Threshold). Then the image is subjected to Automatic thresholding (Image > Adjust >Threshold; method: triangle, dark background, apply). Thresholding is the simplest form of image segmentation but has the disadvantage that sometimes when two or three cells are very close together, they get segmented as one large cell. This can be corrected by running a watershed algorithm on the grey-scale image to split the contiguous cells ((Process > Binary > Watershed). Fig. 10 shows the preprocessed image which is subjected to thresholding resulting in the segmentation of cells. Regions of interest as previously defined were selected (ROI manager) and the particle analyzer was set to run using size of 30-1200 and circularity of 0-1.0. The number of presynaptic cells in the defined ROI's appeared in the results window.
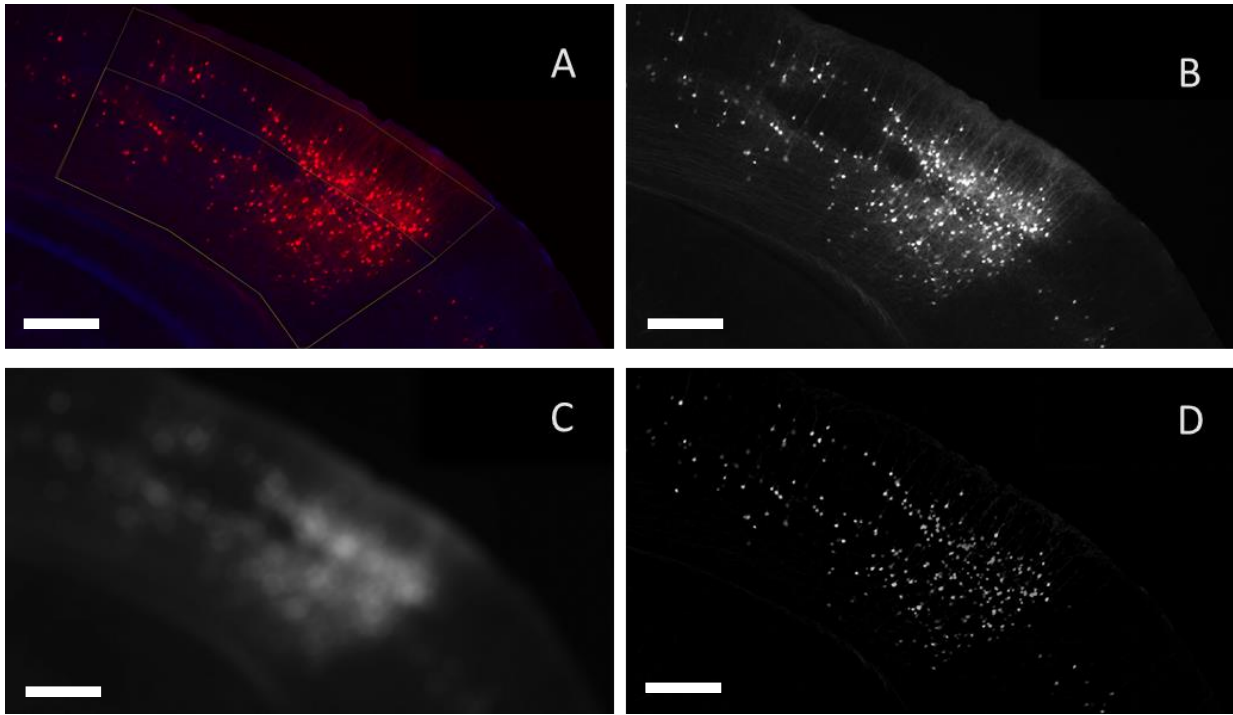
Figure 9. A. Original image with ROIs defined. **B.** Red channel image of the original image. **C.** Blurred image of the red channel image which is subtracted from **B** to give **D**, which is the final preprocessed image ready to be automatically quantified. Scale bars: 500 µm.
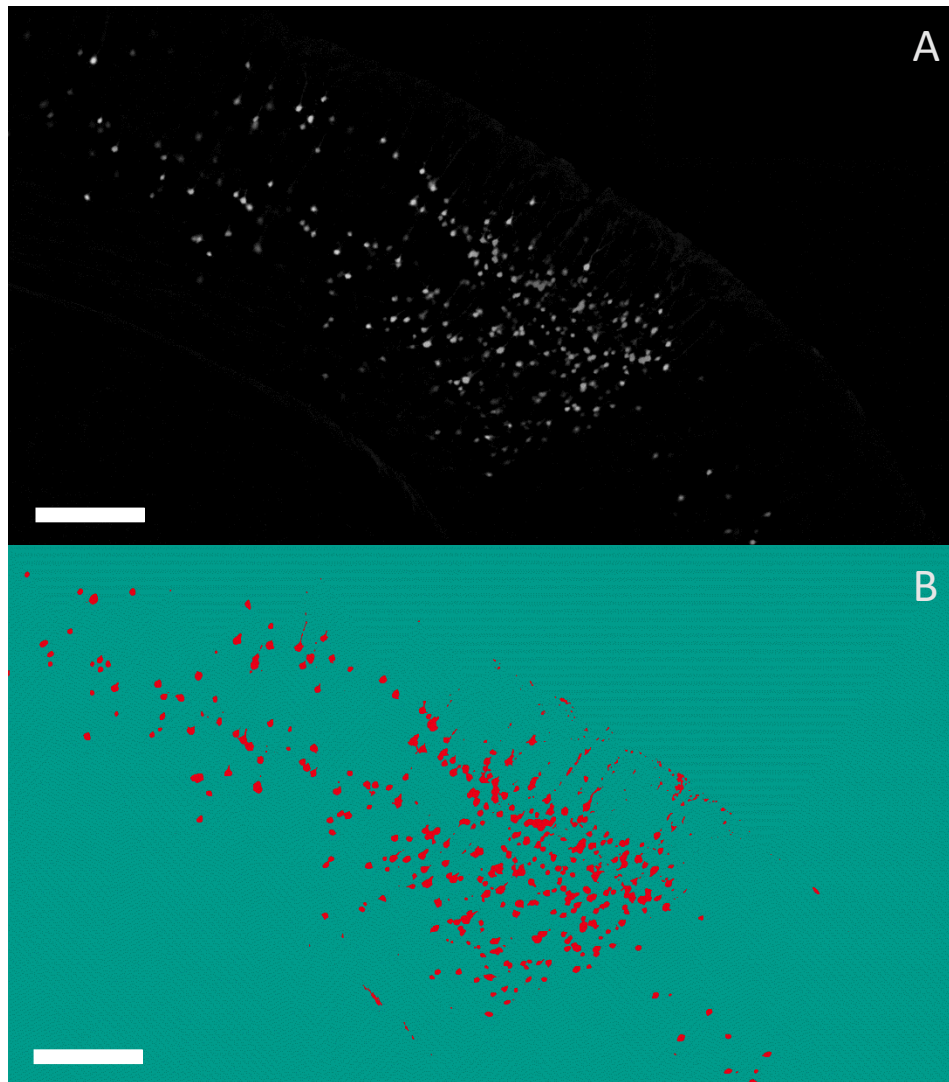
Figure 10. Example of automatic quantification. **A.** Preprocessed image. **B.** Post-thresholding: Segmented image showing the segmented cells (red). The segmented cells are then counted using the particle analyzer in ImageJ. Scale bar: 500 µm.

2.7 Statistical Analysis

Results are presented as mean ± SEM. Statistical evaluation was performed using GraphPad Prism 7 for Windows. For the analysis of the projection pattern of transcallosal neurons in the contralateral hemisphere, the location of the cell bodies of transcallosal axons and their general layer distribution I performed 1-way ANOVA followed by Tukey's post hoc test. The laminar distribution of transcallosal neurons in the three different areas across the mouse cortex was evaluated using 2-way ANOVA followed by Bonferroni's post-hoc test. Cortical thickness, cell density, cell size, dendritic and axonal branching were evaluated with 1-way ANOVA. Furthermore, I used 1-way ANOVA followed by Dunnet's, Tukey's or Sidak's multiple comparisons test for the analysis of proximal, distal and apical tuft spine density. Spine density across the different neuronal populations (transcallosal vs non-transcallosal) was evaluated using 2-way ANOVA and subsequent Sidak's post.hoc test. Spine morphology was evaluated with 1-way ANOVA per spine category followed by Tukey's post-hoc test. Lastly, the statistical test I used for evaluating the connectivity ratios in different brain regions and the connectivity along the rostro-caudal axis was 2-way ANOVA followed by Tukey's post-hoc. Significance degrees are indicated as follows: $*p < 0.05$; $**p < 0.01$; $*** p < 0.001$. All programs used are listed in detail in Table 10.

Table 10

Programs	Version	Website
LAS X	3.5.018371	http://www.leica-microsystems.com/products/microscope-software/p/leica-las-x-ls/app/
FV10-ASW Viewer software	v4.2b	https://www.olympus-lifescience.com/en/support/downloads/
Fiji		http://fiji.sc/
Neuron Studio(CNIC)	ns0.9.9.2	http://research.mssm.edu/cnic/tools-ns.html
Huygens Essential (Scientific Volume Imaging, The Netherlands)	15.10	https://svi.nl/Huygens-Essential
Stereo Investigator (MBF Bioscience, Williston, VT USA)	v2017.03.2	http://www.mbfbioscience.com/stereo-investigator
Definiens Developer XD	v 2.7.0	https://www.definiens.com/tissue-phenomics
Graph Pad Prism	7	https://www.graphpad.com/scientific-software/prism/

Chapter 3: Results

3.1 Descriptive study of transcallosal neuron distribution across the mouse cortex.

Based on the publication*: Chovsepian A*, Empl L*, Correa D, Bareyre FM. Heterotopic Transcallosal Projections Are Present throughout the Mouse Cortex. Frontiers in Cellular Neuroscience. 2017;11:36. doi:10.3389/fncel.2017.00036.* <u>Copyright</u> © 2017 Chovsepian, Empl, Correa and Bareyre.*equal contribution.*

The details on the specific contribution to the results presented in this chapter are presented in Table11 below.

Table 11: Specific contribution to the data presented in 3.1

Conception and design of study	Florence Bareyre	Alexandra Chovsepian	Laura Empl
Acquisition of data included in this dissertation Stereotactic brain injections Animal perfusions and tissue processing Image acquisition Image processing and analysis	Alexandra Chovsepian Alexandra Chovsepian Alexandra Chovsepian Alexandra Chovsepian	Laura Empl	
Data analysis and statistical evaluation	Alexandra Chovsepian	Laura Empl	
Drafting of manuscript	Alexandra Chovsepian	Laura Empl	Florence Bareyre
Critical revision	Florence Bareyre		

The overall goal of this project was to describe the regional variability of transcallosal connections in anatomically and functionally distinct brain areas. In order to do so, I implemented an anterograde and a retrograde tracing method. Anterograde tracing was used to reconstruct the global distribution of transcallosal axons in the cleared brain and to further determine the laminar distribution of transcallosal projection terminals at the contralateral hemisphere. Retrograde tracing was employed to pinpoint the location of transcallosal projection neurons across an extensive cortical volume, including motor and somatosensory regions.

3.1.1 Anterograde tracing showing that transcallosal neurons located in different layers similarly innervate the entire contralateral cortical column

In this experimental part I used the tracer BDA 10,000 MW for anterograde labeling of transcallosal connections. The first question was whether transcallosal neurons of cortical layer II/III or V would innervate the contralateral cortex in a different pattern. For answering that, I injected BDA either in layer II/III (fig. 11 left upper) or layer V (fig. 11 left lower).
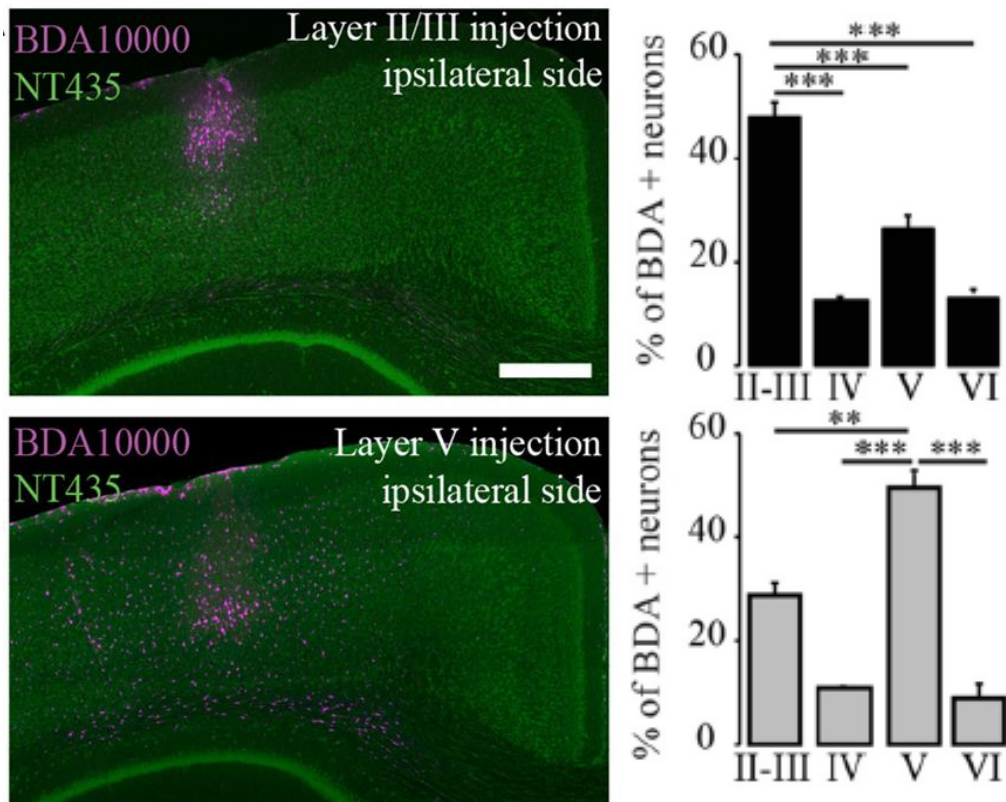
Figure 11 (Left) confocal images of the ipsilateral cortex following anterograde tracer injections (biotinylated dextran amine-BDA 10,000 MW) in layer II/III (upper, N=4) and layer V (lower, N=4). (Right) quantification of neurons labeled with BDA in the different layers following injections in layer II/III (upper) and layer V (lower). N=4 Scale bars: 500 µm. Statistical evaluation: 1-way ANOVA, followed by Tukey's post hoc test. **p < 0.01, ***p < 0.001. Error bars: SEM. Figure citation: Chovsepian, A., et al., 2017

To control the laminar specificity of my injections, I measured the proportion of BDA labeled neurons at the site of injection in each cortical layer, as defined by NeuroTrace counterstaining (fig. 11 left). Layer II/III injections resulted in a predominant localization of labeled cells in the corresponding layer (p < 0.001) and in a similar fashion, layer V injections induced labeling of cells mainly in the corresponding layer (p < 0.01).

Following that, I analyzed the projection pattern of transcallosal neurons in the contralateral hemisphere. I saw that after layer II/III or layer V injections the transcallosal axons projected predominantly to the homotopic area (HA), displaying a strong columnar organization with terminal fields of the axons spanning the entirety of the cortical column (fig. 12 B,C). Besides these homotopic projections, I noticed a number of transcallosal axon branches appearing more medially or more laterally from the main columnar projections (white arrows, fig. 12 A right). The observed ectopic projections were more often a result of layer V injections, but were also detected after layer II/III injections. As a last step, I examined the laminar location of transcallosal axon terminal fields that were labeled by each of the two types of injections. That was achieved by separately measuring the integrated fluorescence intensities in each cortical layer of the homotopic contralateral cortex. In general, no differences were seen between the two injection sites. Furthermore, averaging all injections sites, 48.4 ± 3.4% of the total projections were located in layers II-IV, 35.1 ± 2.8% in layer V and 16.4 ± 1.8% in layer VI (fig. 12 C).

These results suggest that transcallosal neurons project to the contralateral cortex in a homotopic fashion (although some heterotopic axonal projections exist) and exhibit similar contralateral projection patterns, independently of their laminar location. However, it should be highlighted that those projections are not rigorously restricted to layers II-IV and V but are also, in a smaller extent, found in layer VI, therefore spanning the full extent of the cortical column (Figure 12 B).
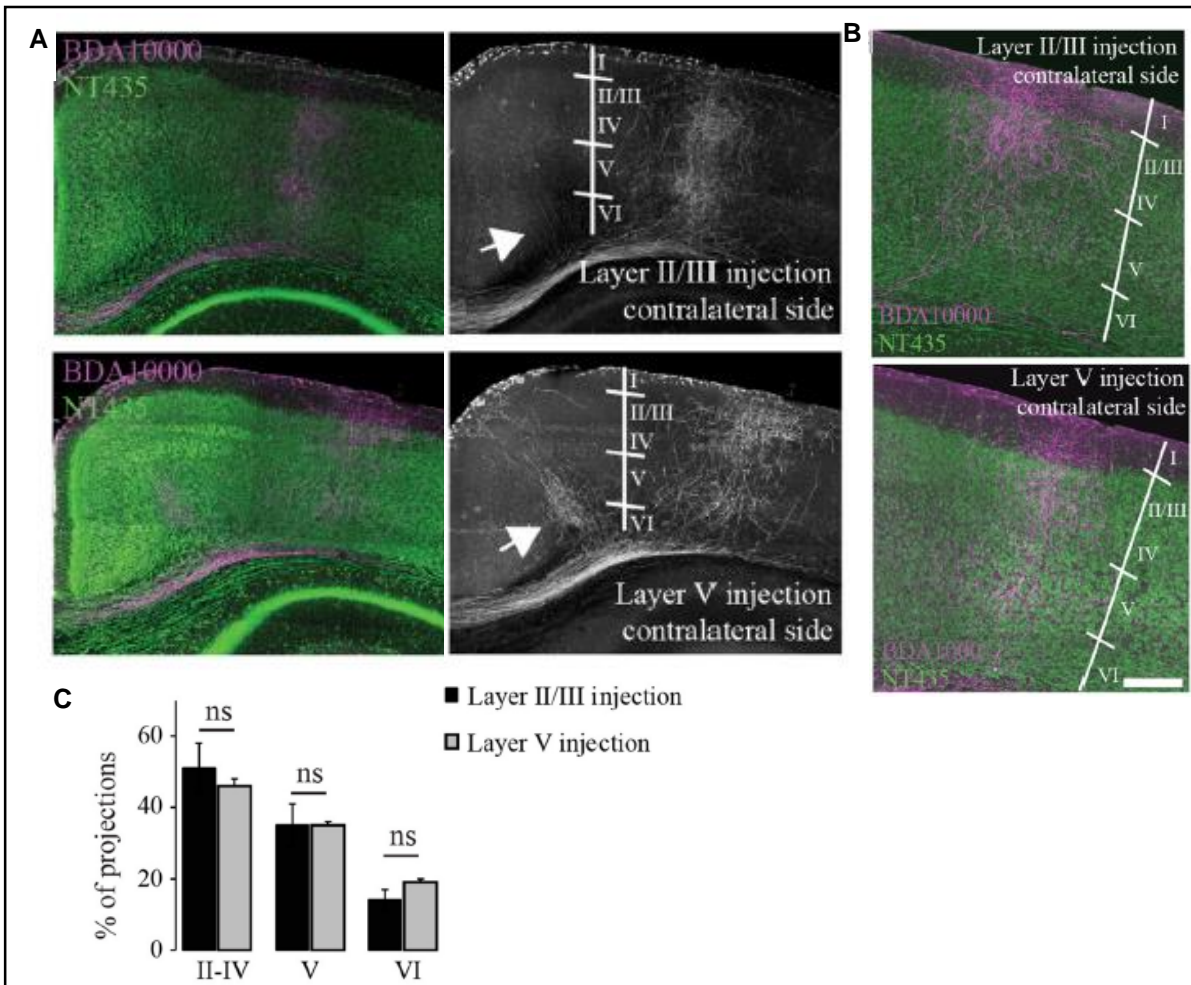
Figure 12. (A, left) Confocal images showing transcallosal projections in the contralateral hemisphere after injection of BDA 10,000 MW in layer II/III (upper) and V (lower) of the ipsilateral cortex (NeuroTrace: green, BDA 10,000 MW: purple). (A, right) BDA channel only for better contrast. White arrows indicate the existence of axonal projections outside of the homotopic area after layer V injections and to a smaller extent after layer II/III injections. (B) Higher magnification images of the contralateral cortex displaying the transcallosal axon-terminal fields following injection in layer II/III (upper, N=4) or layer V (lower, N=4). (C) Quantification of the position of transcallosal axon terminals in the contralateral cortex and their distribution across cortical layers. No differences detected between injections in layer II/III and V. Scale bars: 500 μm in (B), 200 μm in (C). Statistical evaluation: 1-way ANOVA, followed by Tukey's post hoc test. Error bars: SEM. Figure citation: Chovsepian, A., et al., 2017

3.1.2 Retrograde labeling verifies the homotopic organization of transcallosal projection neurons but also manifests distinct heterotopic connections

In this part of the study, I aimed to define the location of the cell bodies of transcallosal axons using fluorogold (FG) as a retrograde tracer [259] [260]. I implemented six different injection coordinates, covering the primary motor cortex and primary somatosensory cortex. According to the quantification, most transcallosal axons originate from cells that are located in the homotopic area of the contralateral cortex. To quantitatively confirm this observation, the following three areas were separately analyzed for each injection: the area homotopic to the contralateral site of injection (HA), as well as the equally-sized medial (MA) and lateral (LA) areas (fig. 13, fig 14 left). When pooling all animals (and thus injection coordinates) together, the findings showed that the majority of transcallosal neurons are mainly located in the HA ($p < 0.001$). More precisely, $63.8 \pm 9.3\%$ of the total number of cells of origin of transcallosal axons belonged to the HA. Interestingly, an important portion ($21.9 \pm 6.1\%$) of transcallosal cells were detected in the LAA and a non-negligible $14.7 \pm 7.2\%$ in the MAA (fig. 14, right), indicating the significance of such heterotopic connections. Moreover, some cells were located ectopically outside all three defined areas (fig. 13 lower; white arrows) especially at the region of the perirhinal cortex (fig 13 lower; white arrowhead).
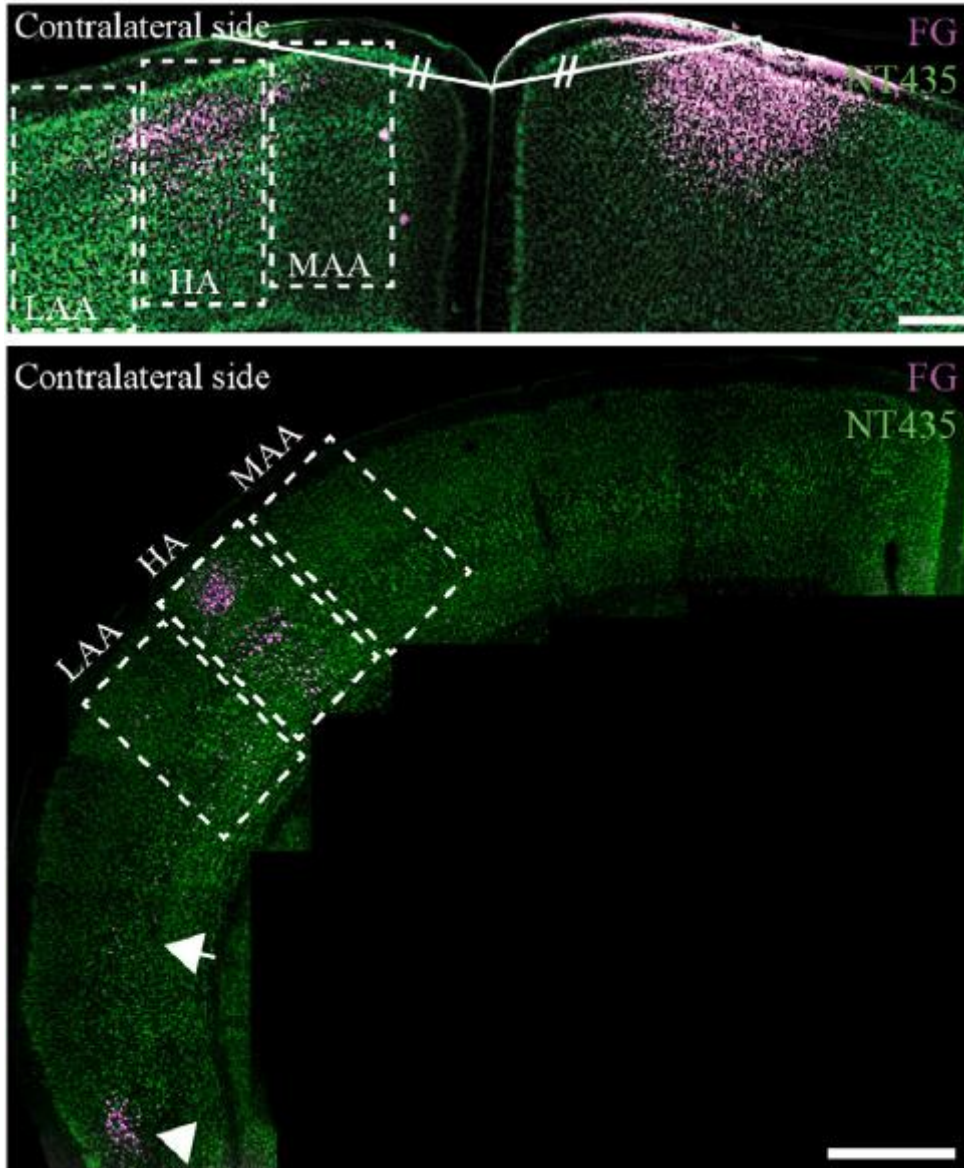
Figure 13. Upper: Confocal image showing transcallosal projection neurons retrogradely labeled by injection in the motor cortex rostral to Bregma. Illustration of the area definition used for analyzing the homotopic organization of the transcallosal projection neurons: homotopic area (HA), lateral adjacent area (LAA), medial adjacent area (MAA). **Lower:** Confocal image showing transcallosal projection neurons retrogradely labeled by injection in the barrel cortex caudal to Bregma. Transcallosal projection neurons are located mainly in the area homotopic to the contralateral point of injection (HA) and are found in a smaller extent in the two adjacent areas. Transcallosal projection neurons are also detected in the S2 (white arrow) as well as the lower perirhinal cortex (white arrowhead). Scale bars: 200 μm in upper, 500 μm in lower. Figure citation: Chovsepian, A., et al., 2017
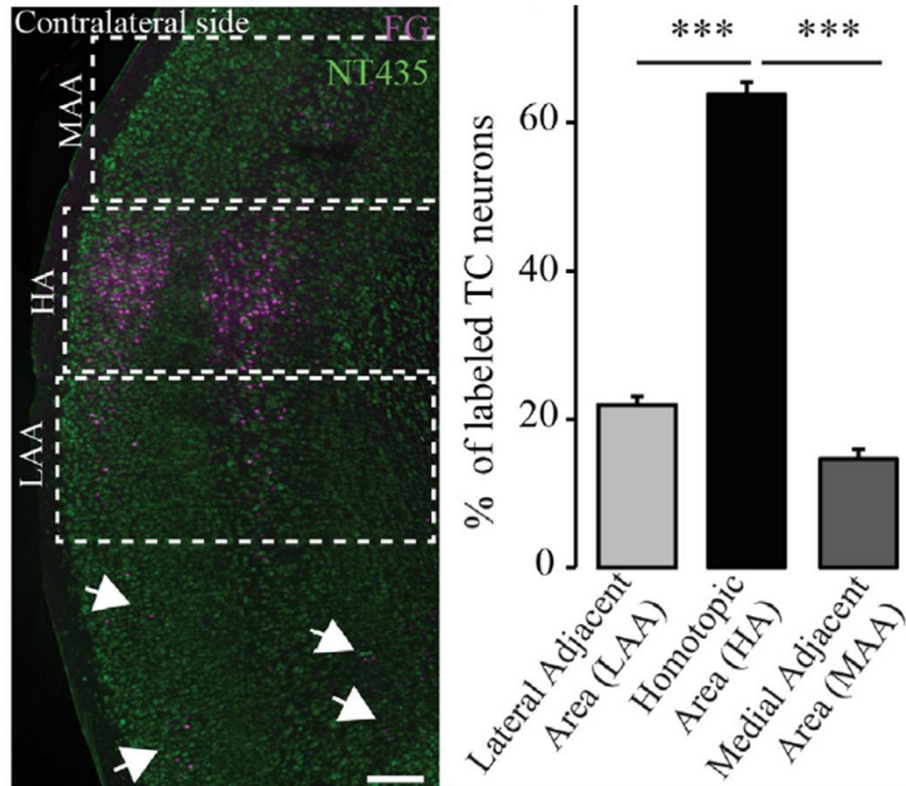
Figure 14. Left: Confocal image showing transcallosal projection neurons retrogradely labeled by injection in the barrel cortex caudal to Bregma. Transcallosal projection neurons are located mainly in the area homotopic to the contralateral point of injection (HA) and are found in a smaller extent in the two adjacent areas, as well as outside the adjacent areas in the barrel field. Scale bars: 200 μm. **Right:** Quantification of the repartition of transcallosal projections neurons in the three defined areas. 1-way ANOVA followed by Tukey post hoc test. N=12; Error bars: SEM, ***p < 0.001. Figure citation: Chovsepian, A., et al., 2017

Subsequently, animals that received retrograde injections at different coordinates were analyzed separately. The results showed that the homotopic organization of transcallosal neurons is present independently of the site of injection (fig.15 A–J). Regarding the rostral coordinate injections, 68.5 ± 4.2% of the transcallosal neurons traced from the M1 cortex were found in the HA, 69.4 ± 5.3% of the neurons traced from the S1 cortex were located in the HA and 62.2 ± 4.7% of the neurons traced from the barrel cortex were localized in the HA. Similarly, in the case of caudal coordinate injections, 57 ± 1.7% of the neurons traced from the M1 cortex, 63 ± 4.8% traced from the S1 cortex and 61 ± 2.2% traced from the barrel cortex were detected inside the HA (fig. 15 H). Moreover, the percentages of transcallosal cells located in the lateral and medial adjacent areas were in a similar range across all coordinates tested in this study. Therefore, these results further verify that, while the homotopic organization pattern is

preserved throughout the cortex, there is a substantial proportion of transcallosal neurons that are located heterotopically (fig. 15 I, J).
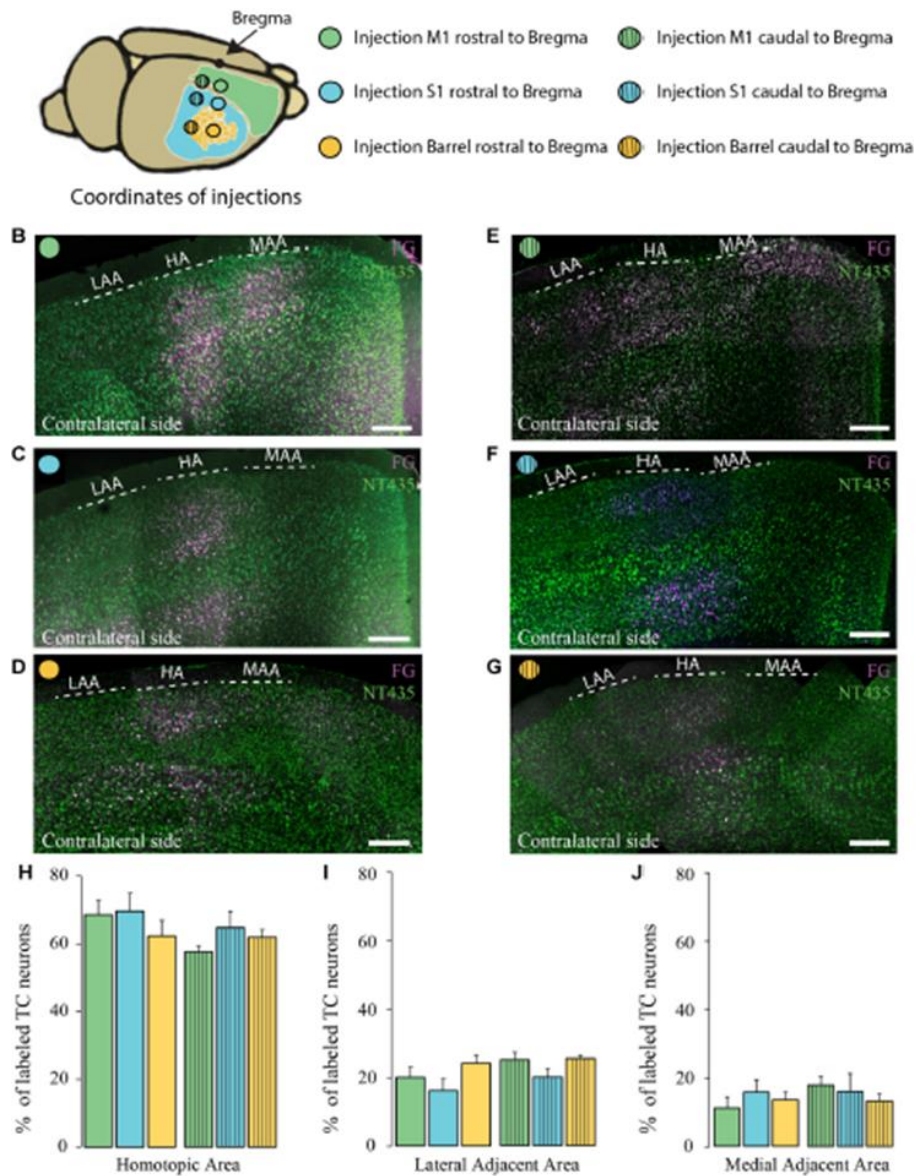
Figure 15. Analysis of the homotopic organization of transcallosal projection neurons in different brain regions. (A) Schematic illustration of the stereotactic injection coordinates selected for retrograde labeling. (B–G) Confocal images of the contralateral cortex after Fluoogold injection *rostral* to Bregma in motor cortex (B), somatosensory cortex (C), barrel cortex (D) or *caudal* to Bregma in the motor cortex (E), somatosensory cortex (F), barrel cortex (G) showing the homotopic organization of transcallosal projection neurons. Scale bars: 250 µm.

(H–J) Quantification of the distribution of the transcallosal projection neurons in the three different areas of the contralateral cortex, HA (H), the LAA (I) and the MAA (J). Full bars: injections *rostral* to Bregma, dashed bars: injections *caudal* to Bregma. Green: injection in the motor cortex, Blue: injection in the somatosensory cortex, Yellow: injection in the barrel cortex. One-way ANOVA followed by Tukey's test per area, N=4 (per coordinate); Error bars: SEM. Figure citation: Chovsepian, A., et al., 2017

3.1.3 Localization of transcallosal neurons mainly in layers II/III and V but also in ectopic layers especially in heterotopic areas

As a following step, the laminar distribution of transcallosal neurons in the HA, LAA and MAA, was examined separately. I based the layer identification on NeuroTrace staining and all FG positive neurons in each layer were counted (fig. 16 A–C). When all animals were pooled together, independently of injection coordinates, the results showed that transcallosal neurons in the HA are primarily located in layer II/III ($42.3 \pm 1.0\%$ of FG positive neurons) and in layer V ($31.8 \pm 1.4\%$ of FG positive neurons). However, smaller but not negligible percentages of FG labeled cells were detected in layer IV ($11 \pm 0.9\%$) and in layer VI ($14.9 \pm 1.2\%$; fig. 16 A, D). Regarding the adjacent areas, these percentages were slightly different and the layer specific organization seems generally less strict, particularly in case of the LAA (fig. 16 B,F).
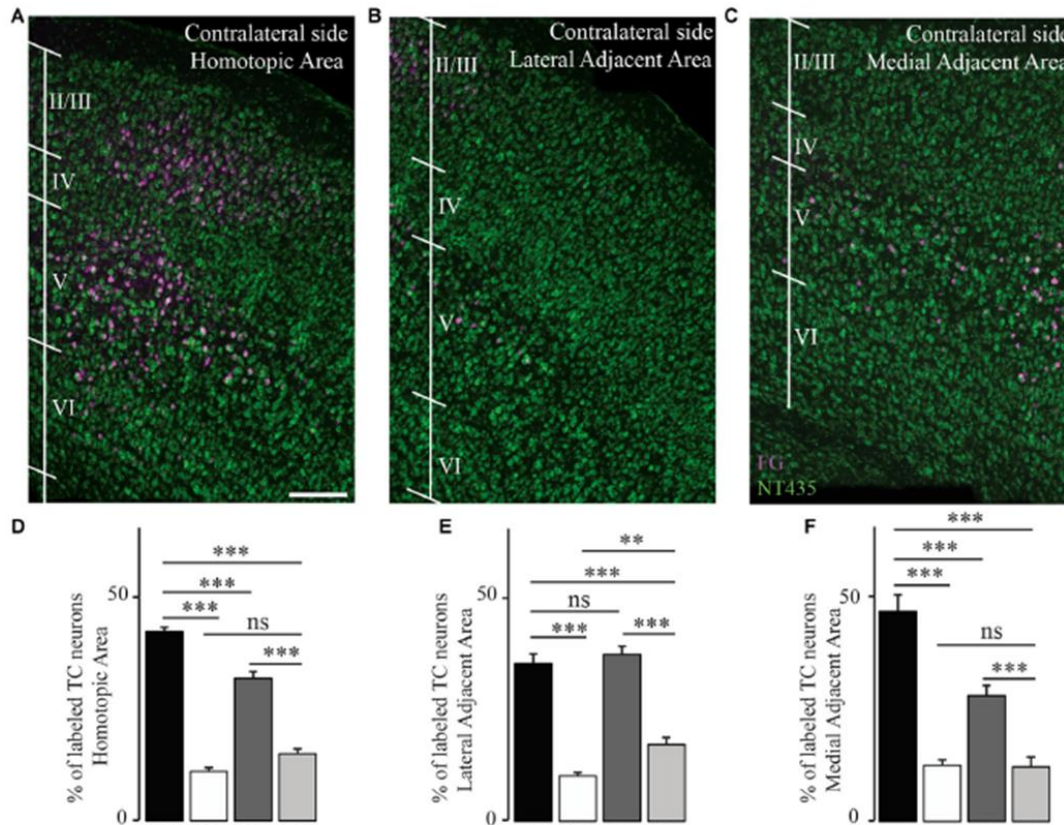
Figure 16. Transcallosal projection neurons reside mainly in layer II/III and layer V of the contralateral cortex. (A) Confocal image of the homotopic cortical area (HA) showing the majority of the labeled transcallosal projection neurons in layer II/III and layer V. (B) Confocal image of the lateral adjacent projection area (LAA) showing comparable numbers of transcallosal projection neurons in layer II/III and layer V. (C) Confocal image of the medial lateral adjacent projection area (MAA), showing the distribution of transcallosal projection neurons across cortical layers. Scale bars: 200 μm. (D-F) Quantification of the partition of transcallosal projection neurons across the different cortical layers in the HA (D), LAA (E), MAA (F). 1- way Anova followed by Tukey post hoc test: **p<0.01, ***p< 0.001. N=12; Error bars: SEM. Figure citation: Chovsepian, A., et al., 2017

Lastly, I investigated whether the laminar distribution of transcallosal neurons varies according to different regions of the cortex by analyzing different coordinate injections separately, as shown in fig. 17. For all coordinates, when looking at the HA, the majority of FG positive neurons was located in cortical layer II/III and V (fig. 17 B–D). Considering the LAA, FG injections in the motor and somatosensory cortices induced a HA-like distribution but with small marginal differences (fig. 17 B, D). On the other hand, both rostral and caudal to Bregma injections into the barrel cortex revealed the presence of higher numbers of transcallosal neurons in layer V than in layer II/III of LAA (fig 17 C). With regards to the MAA, especially for primary motor cortex injections, a relatively high percentage of transcallosal neurons were found in layer II/III. As shown in fig. 17 D, layer II/III contained more than 50% of FG positive cells in case of rostral injections and more than 70% of FG positive cells in case of caudal injections.
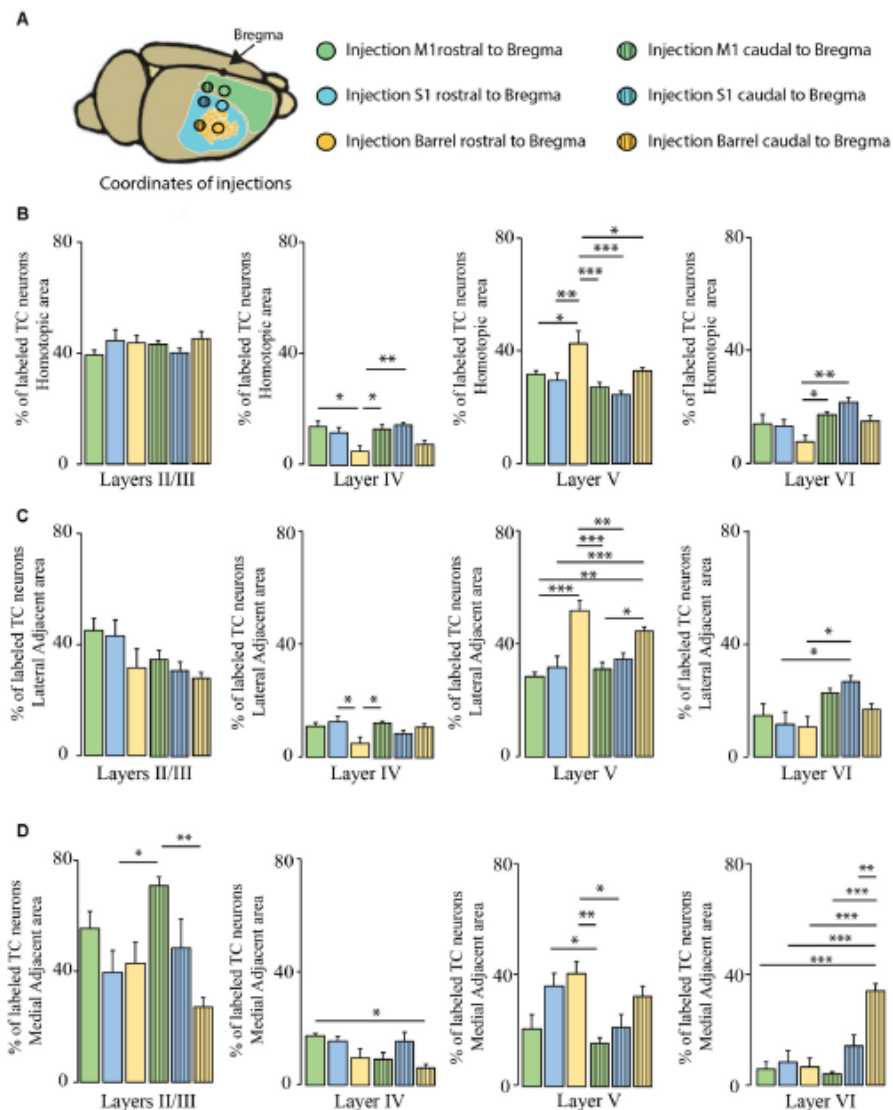
Figure 17. Analysis of laminar distribution of transcallosal projection neurons in the three different areas across the mouse cortex. (A) Schematic illustration of the stereotactic injection coordinates selected for retrograde labeling (B-D) Quantification of the distribution of transcallosal neurons across the different cortical layers of the HA (B), LAA (C), MAA (D) following injections rostral to Bregma (full bars) and caudal to Bregma (dashed bars). Green: injection in the motor cortex, Blue: injection in the somatosensory cortex, Yellow: injection in the barrel cortex. 2- way ANOVA (independent variables: areas of labeling and injection sites) followed by Bonferroni post hoc test per dataset. $*p < 0.05$, $**p < 0.01$, $***p < 0.001$. N=4 (per coordinate); Error bars: SEM. Figure citation: Chovsepian, A., et al., 2017

Overall, the results indicate a uniform organization of transcallosal connections. Interestingly, this organization is distinctly homogenous in the HA and displays higher regional variability in the adjacent medial and lateral areas.

3.2 Effects of TBI on the structural integrity of transcallosal neurons located in the contralateral intact cortex

The details on the specific contribution to the results presented in this chapter are presented in Table12 below.

Table 12: Specific contribution to the data presented in 3.2

Conception and design of study	Florence Bareyre	Alexandra Chovsepian	
Acquisition of data Stereotactic brain injections and trauma induction	Alexandra Chovsepian		
Animal perfusions and tissue processing	Alexandra Chovsepian		
Image acquisition	Alexandra Chovsepian		Mario Kreuzfeld
Image processing and analysis	Alexandra Chovsepian	Maite Marcantoni	
Interpretation of data and statistical evaluation	Alexandra Chovsepian		

After acquiring significant insight into the cortical and laminar distribution of the aforementioned population of interest (transcallosal neurons-TC), I implemented this knowledge to study the effect of focal TBI (controlled cortical impact-CCI) on the structural integrity of this anatomically connected neuronal population, in a time-dependent manner (2, 7, 14, 21, 42 and 84 days post-injury-dpi). Following an initial characterization of the focal cortical damage my mild CCI produced, I investigated the effects of TBI on the general state of the contralateral, intact cortex. First, I looked for potential TBI-induced changes at the contralateral cortical thickness, as well as the contralateral cell density and the average cell size, differentiating between the TC population and the general neuronal population. I then examined whether TBI alters the contralateral dendritic structure, in terms of branching and spine density, and how such changes are evolving with time, in TC and non-TC (NTC) neurons.

3.2.1 Lesion volume estimation after mild TBI

First, to characterize my mild-TBI (0.5mm penetration) model I estimated the lesion volume 3 days after the impact. In a series of 4-injured mice the average lesion volume was 7.063 ± 0.603 mm^3.
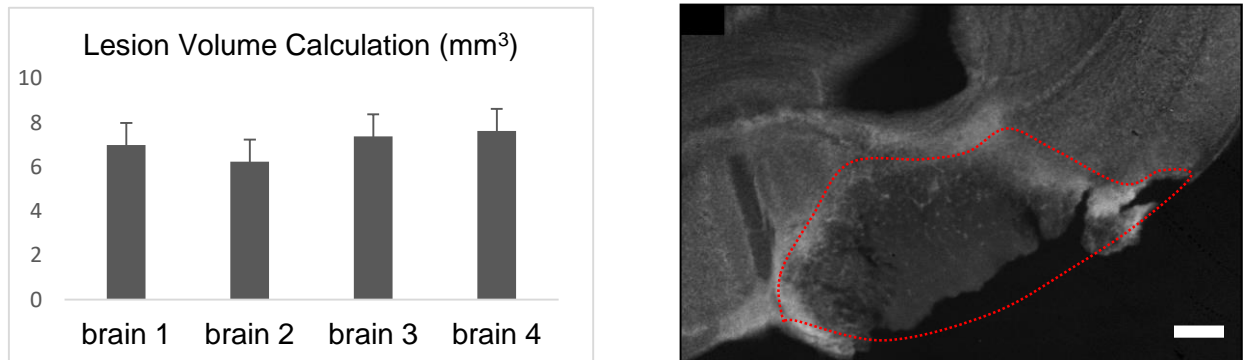
Figure 18. Left: Calculated lesion volumes and SD according to the formula described by Yu et al. **Right:** Example of lesion area outlined using image J. Scale bar: ~ 500μm. Error bars: SEM

3.2.2 No significant changes in cortical thickness of the contralateral cortex after TBI

I measured the thickness of the intact cortex at four different rostro-caudal coordinates: sections A (+0.7mm from Bregma), B (-0.7mm from Bregma), C (-1.7 mm from Bregma) and D (-2.7mm from Bregma), spanning the entire injured area (fig. 19, upper). Section A was only used as an 'internal control', since it is located rostrally to the start of the TBI lesion.

Overall, as an average of sections B, C and D, the contralateral cortical thickness was not significantly different between control and all the post-injury timepoints, despite a tendency for higher thickness at 2dpi (1-ANOVA [$F_{(6, 27)}$ = 0.9039, p=0.5067] (fig 20, A). In addition, the thickness of each layer was separately measured and there was no significant change in laminar thickness after TBI at any timepoint. Therefore, according to my results TBI does not induce cortical thinning or swelling in the contralateral cortex and does not affect the distinct cortical layers differently.
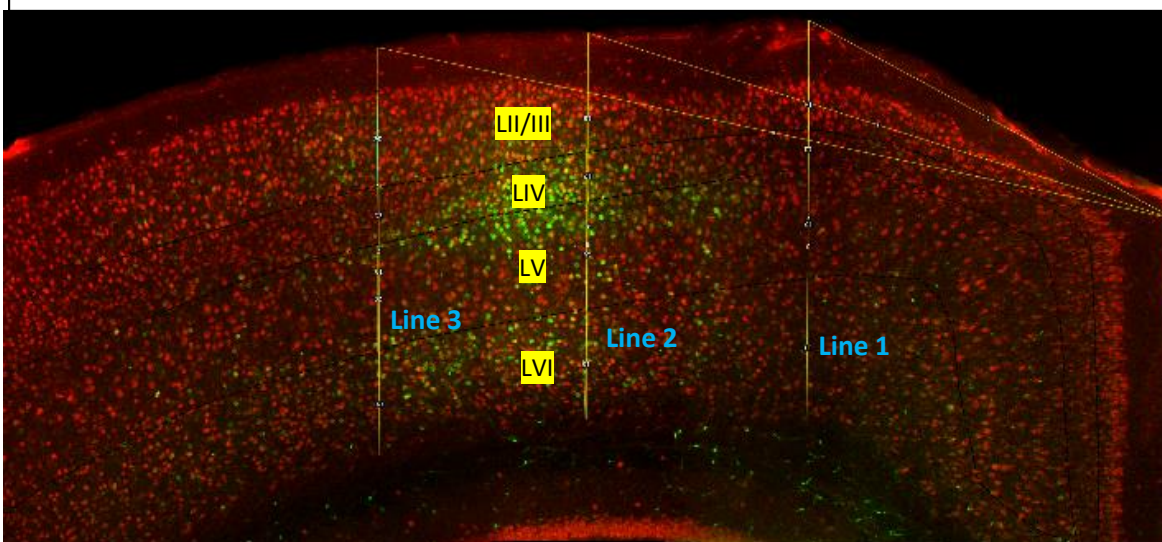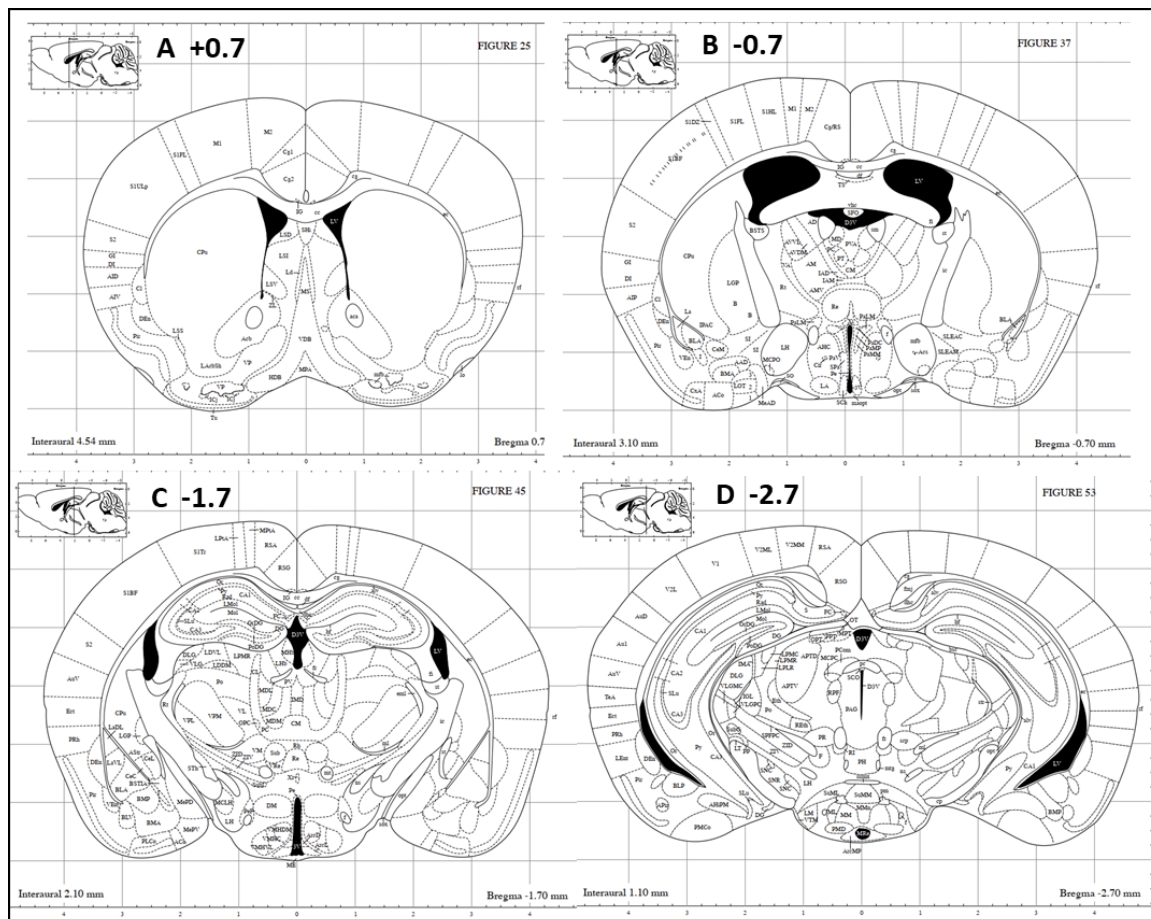
Figure 19. Upper: Sections A, B, C and D selected according to Paxinos mouse brain atlas (Image credit: Franklin, K.B.J. & Paxinos, G. (1997). The mouse brain in stereotaxic coordinates) **Lower:** Example image of section C showing the 3 lines that were measured and averaged to obtain the mean cortical thickness of this section. Scale bar: ~ 500 μm
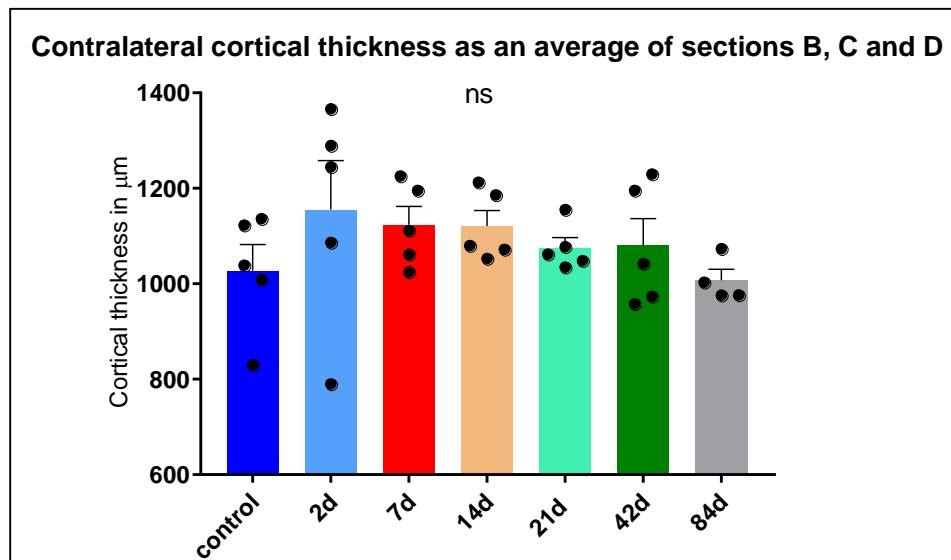
Figure 20. Mean contralateral cortical thickness, as an average of sections B, C and D. Despite tendency for higher thickness at 2dpi compared to control, the difference is not statistically significant, as shown using 1-way ANOVA. Each dot represents one animal (N=5). For 84d N=4. Error bars: SEM

3.2.3 No general changes in cell density and cell body size at the contralateral cortex after TBI

Following the cortical thickness analysis, I examined how cell density in the intact cortex is affected by TBI at different timepoints post-injury. I focused on sections B, C, D (see figure 19) as these were the ones directly opposite to the lesion, spanning its full extent. The 84dpi group is excluded from this analysis since important data points were missing due to technical limitations. TBI did not induce any significant changes in contralateral cell density when sections B, C and D were averaged, despite an observable but non-significant reduction at 2dpi compared to control and other post-injury timepoints (1-way ANOVA: $F_{(6, 19)}$ = 1.996, p=0.1097), as shown in fig. 21, middle, left.

The next parameter I explored in terms of TBI-related changes at different post-injury timepoints was the size of the cell body in the contralateral cortex, distinguishing between TC (anatomically connected to the lesioned area) and NTC neurons (not connected to the lesioned area; fig 21 upper). For this analysis, I again took the average of sections B, C and D. Looking at the general contralateral population, I detected no significant effect of the injury at any timepoint on cell body size (1-way ANOVA: $F_{(5, 19)}$ =1.173, p=0.3585). For NTC neurons, I observed a tendency for increased cell body size at 2dpi that is not statistically significant (1-way ANOVA: F

(5, 19) = 2.496, p=0.0672) as shown in fig. 21 lower, left. In case of TC neurons (fig. 21 lower, right), I found no significant difference across the different groups [F (5, 19) = 1.68, p=0.1879].
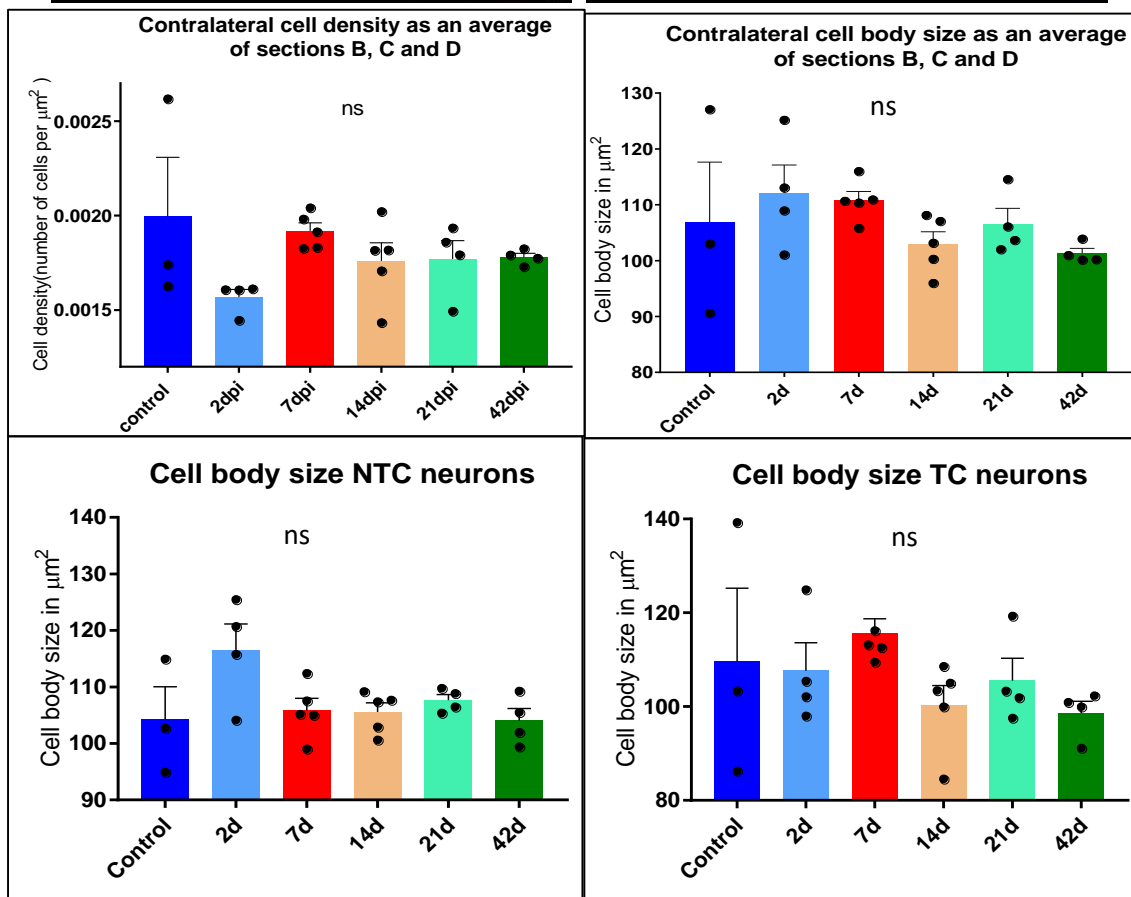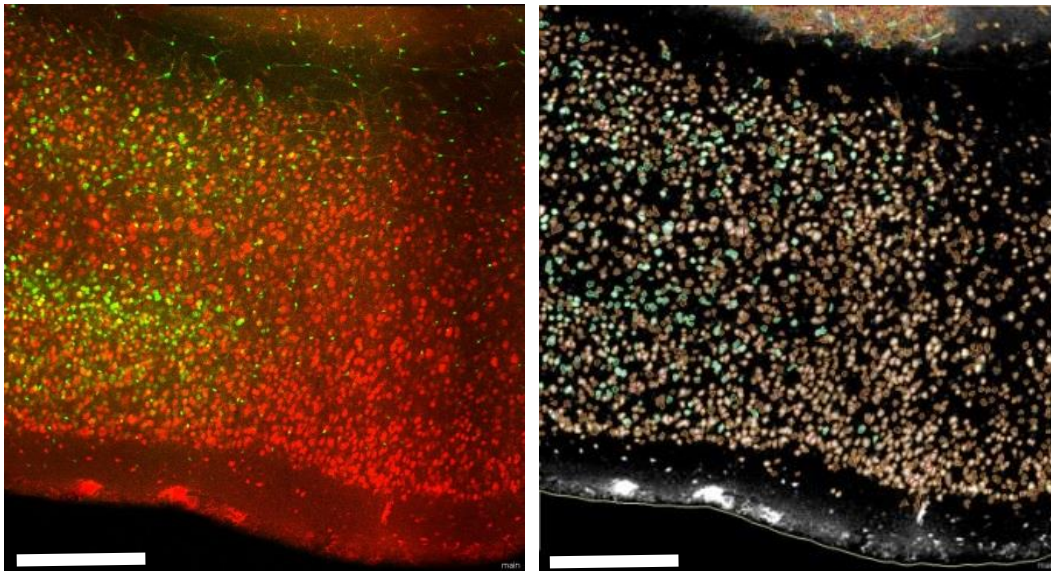
Figure 21. Upper: Example of automatic quantification at the contralateral cortex, used for both cell density and cell body size evaluation. Original image **(left)** and processed image **(right)**. Non-transcallosal neurons show in red and transcallosal neurons show in green. Scale bars: ~ 500 μm. **Middle, left:** Cell density at the contralateral cortex (averaging sections B, C and D), calculated as the number of cells automatically counted, divided by the size of the area (μm²) that was quantified. No significant difference between groups as shown using 1-way ANOVA. **Middle, right**: Mean cell body size in μm², averaging sections B, C and D. Lower, **Left:** Contralateral cell body size in NTC neurons. Tendency for enlargement at 2dpi, but difference not significant (1-way ANOVA). **Right:** Cell body size of TC neurons not significantly different between control group and post-injection timepoints (1-way ANOVA). Each dot represents one animal (N=3-5) Error bars: SEM

Collectively, TBI did not significantly change the contralateral cell density and the average cell body size of neurons in the contralateral cortex at any post-injury timepoint. The observed minor cell density reduction at 2dpi is a transient effect that could be a result of early contralateral edema. This is further supported by the also minor and transient cell body enlargement at 2dpi, particularly in NTC neurons, indicating cytotoxic edema. These observations are in line with the slight increase in cortical thickness occurring only at 2dpi, mentioned in the previous paragraph.

3.2.4 Dendritic and axonal branching of TC and NTC neurons at the contralateral cortex is not significantly altered after TBI.

Another morphological property of neurons in the intact contralateral cortex that could be influenced by TBI in a time-dependent manner, is the dendritic branching, also referred to as dendritic arborization. Higher dendritic arborization could be regarded as a sign of complexity since it enables the formation of more synaptic connections. I investigated the dendritic branching of TC and NTC neurons up to 42dpi. The clear and detailed visualization of dendrites and quantification of their branches was possible thanks to the GFPM mouse line I selected to use throughout this study. I examined GFP-positive neurons of layer V, since it is a layer with high numbers of TC neurons, as this mouse line does not have enough GFP-positive neurons in layer II/II. The selection of GFP-positive TC neurons was based on their positivity for FG labeling, while GFP-positive & FG-negative neurons were considered NTC (fig. 22). Furthermore, I investigated a different cell population, the corticospinal tract or CST neurons, as a clear control population of neurons: These neurons might differ from the initial NTC population, since the latter could contain a small amount of TC neurons that was not labeled by the FG tracer injection. For that purpose, I retrogradely labeled the CST neurons of the intact cortex for the control and the 7dpi group and initially compared them with the original NTC

population, in terms of their dendritic branching. The number of branches of each dendrite was always normalized to the length of the dendrite and therefore expressed as branching points per µm. The CST and NTC population did not significantly differ, for both the control (mean diff = 0.001187 ± 0.004813, p=0.8073) and the 7dpi group (mean diff. = 9.091e-010 ± 0.003599, p>0.9999), as shown using unpaired t-tests. Therefore, for both those groups I pooled the NTC and CST neurons and I will refer to the resulting population as NTC+CST. Overall, using 1-way ANOVA I identified no significant effect of TBI at any post-injury timepoint on the number of branches per µm in case of TC neurons [F (5, 78) = 0.7583, p=0.5826] (fig. 23 lower, left) and NTC +CST$_{control, 7dpi}$ neurons [F (5, 80) = 1.503, p=0.1982] (fig. 23 lower, right). Moreover, there was no significant variance in dendritic branching among neuron types as shown by 2-way ANOVA [F (1, 158) = 0.02328, p=0.8789] (fig 23 upper, left).
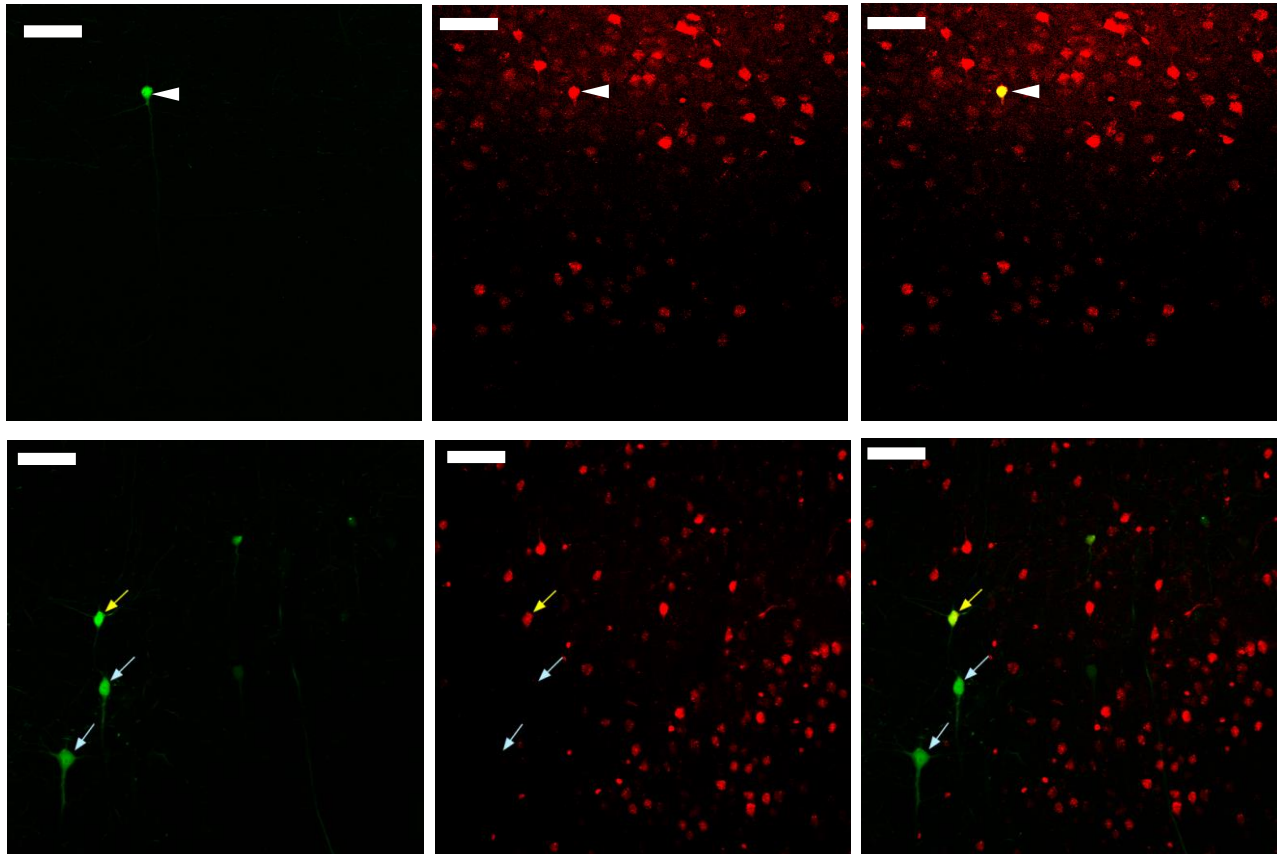
Figure 22. Example imeges for identification of FG+ (TC) and FG- (NTC) neurons in layer V. Acquired with Olympus confocal using 20x objective, zoom of 1.0 and 1024 × 1024 resolution. (Left) GFP, (Middle) FG, (Right) Merged. **Upper:** GFP+ and FG+ double positive neuron (TC, white arrowheads), example of a brain section with sparse GFP expression. **Lower**: Example of a double positive (yellow arrow) neuron and FG- neurons (white arrows) in the same brain section. Scale bars: ~ 200 µm
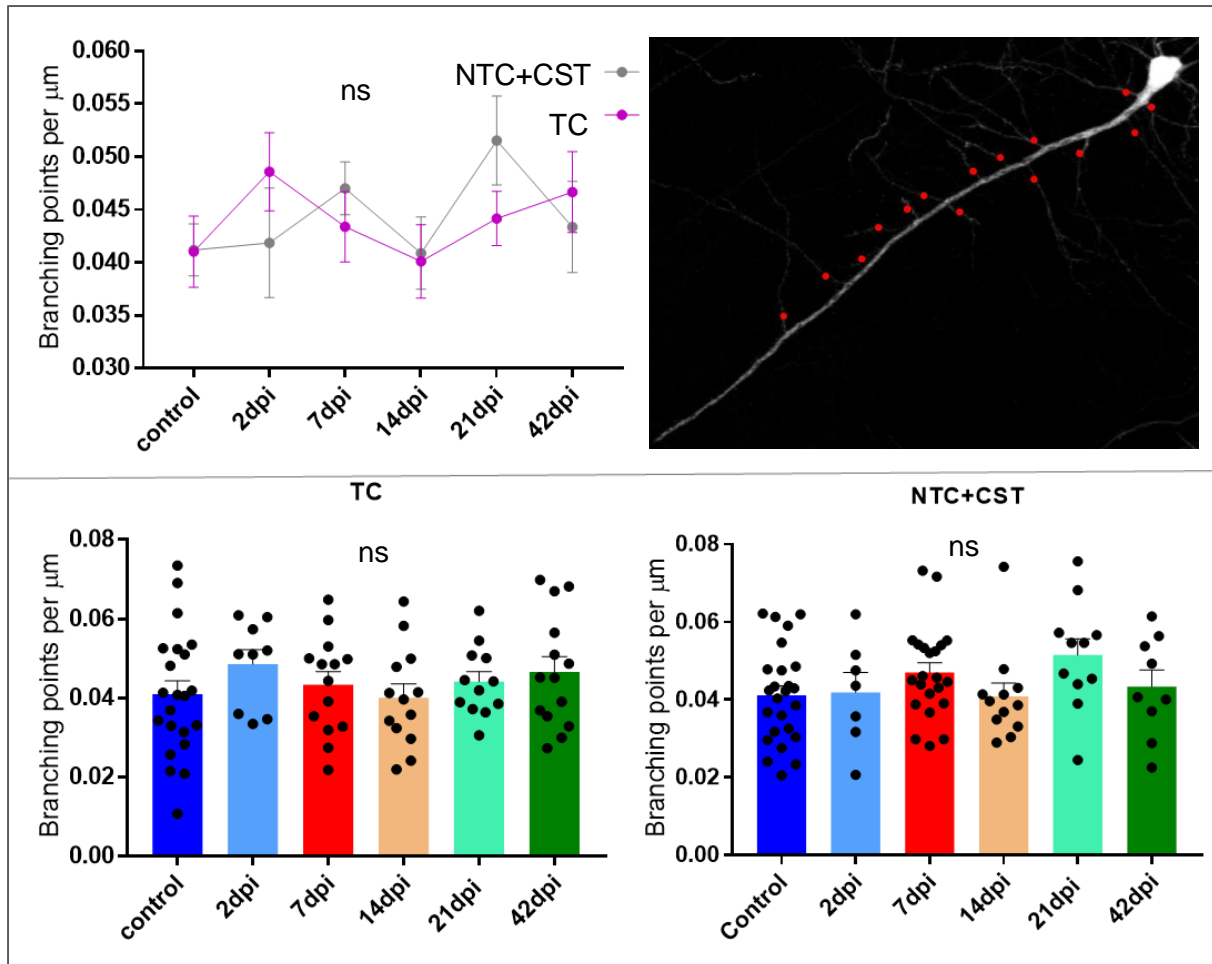
Figure 23. Upper: (Right) Example image of branching point quantification (ImageJ) of a 14dpi layer V dendrite. Red dots represent counted branches. Maximum Z-projection of Olympus confocal scan, acquired with 20x objective, zoom of 1.0, 1024 × 1024 resolution, Kalman filter of 2. (Left) Mean number of branching points per μm. TC population plotted against NTC population across timepoint groups. Control and 7dpi groups contain NTC+CST neurons. **Lower:** (Left) No significant difference between groups for TC determined by 1-way ANOVA. (Right) No significant difference between groups for NTC identified by 1-way ANOVA. Black dots represent individual dendrites. N (TC): control=6 mice/n=22, 2dpi=4mice/n=9, 7dpi=6 mice/n=14, 14dpi=5 mice/n=13, 21dpi=5mice/n=12, 42dpi=4 mice/n=14. N (NTC+CST$_{control,\ 7dpi}$): control=8 mice/n=25, 2dpi=4 mice/n=7, 7dpi=9 mice/n=21, 14dpi=5 mice/n=12, 21dpi=3 mice/n=11, 42dpi=4 mice/n=9. Scale bar: ~ 100μm. Error bars: SEM

Moreover, another question I aimed to answer is whether axonal branching of neurons at the contralateral cortex is altered by TBI. Axonal branching allows individual neurons to connect with multiple targets, enabling the integration of information and the increase of complexity in the nervous system. To understand whether TBI affects the axons of the population directly connected to the injury in a higher extent, I looked at TC versus NTC axons from the beginning

of the neurite up to the point it enters the white matter tract and becomes indistinguishable from other axons. I then counted the branching points and divided the number by the length of the axon, similarly to my dendritic branching quantification. I quantified axonal branching densities in the control animals, 7dpi and 42dpi groups to detect possible differences between an early and a late post-injury stage. I found no statistically significant changes in axon branching induced by the TBI neither at the early nor at the late timepoint, for both neuronal populations (see fig 24).
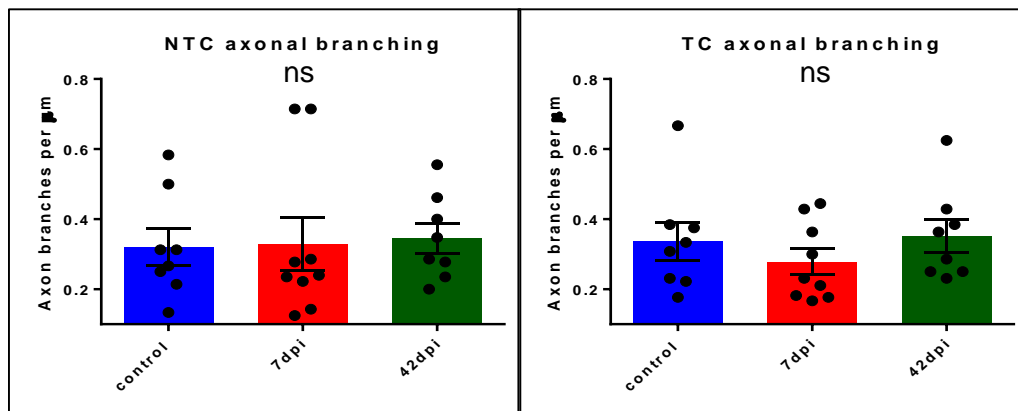
Figure 24. Axonal branching points per µm. **Left:** Axon branching in NTC neurons is not affected by the post-injury timepoint (1-way ANOVA: $F_{(2, 22)} = 0.04015$, p= 0.9607). **Right**: No effect of post-injury timepoint on axon branching in TC neurons (1-way ANOVA: $F_{(2, 22)} = 0.7623$, p = 0.4785). Each dot represents an individual axon. N=5 mice per group. Control, 42dpi: n=8, 7dpi: n=9; Error bars: ±SEM

3.2.5 Dendritic spine density of TC neurons at the contralateral cortex is significantly altered after TBI in a time-dependent manner.

Following the dendritic arborization analysis that revealed no changes after TBI and no significant differences between contralateral TC and NTC+CST neurons, I investigated the effect of TBI on the spine density of those dendrites. Dendritic spines are protrusions of the dendritic shaft, playing the role of synaptic recipients, with an individual spine receiving normally one excitatory synaptic contact. Thus, the number of spines is directly related to the synaptic potential of a dendrite and gives valuable information about the connectivity capacity of a neuron. Moreover, the formation, maturation and maintenance of spines depends on synaptic activity and can be affected by neurodegeneration but also mediate plasticity. Therefore, measuring the spine density at different timepoints after TBI is essential for determining injury-

induced adaptive or maladaptive changes at the intact cortex. For my spine analysis I selected the dendrites that were already examined for their dendritic branching, when possible, as well as additional dendrites originating from neurons located in layer V. Instead of imaging the entire dendrite for spine quantification, I acquired high magnification scans from 3 different areas: the proximal to the cell body area (~70-150 μm from soma, located in layer V), the distal to the cell body area (~370-450 μm from soma, located in layer II/III) and the apical tuft area (~ 510-600 from soma, located in layer I). The number of spines was always normalized to the length of the dendritic segment counted, giving the spine density (spines per μm).

First of all, I examined whether the NTC and CST populations differ in terms of dendritic spine density (see fig. 26 for representative images) and via unpaired t-tests I found that they are not significantly different in both the control group (mean diff. = 0.256 ± 0.1663, p= 0.1383) and the 7dpi group (mean diff.= 0.2635 ± 0.1407, p=0.0642). Therefore, for these two groups I pooled the NTC and CST neurons and I will refer to the resulting population as NTC+CST.

With regards to the proximal dendritic segment, there was no effect of neuron type [2-way ANOVA; $F_{(1, 155)} = 0.2428$, p=0.6229] on spine density across groups (fig. 25 A). Performing a 1-way ANOVA for each neuron type separately, I observed a significant effect of the TBI on the dendritic spine density of TC neurons [$F_{(5, 60)} = 3.039$, p=0.0164] but that was not the case for NTC neurons [$F_{(5, 95)} = 0.7345$, p=0.5994]. More specifically, using a subsequent Dunnett's multiple comparisons test I revealed that 7dpi and 14dpi groups had significantly lower spine density compared to the control group (mean $diff_{control-7dpi.}$ =0.7162 ± 0.2508, p=0.0250, mean $diff_{control-14dpi}$ =0.6995 ± 0.2452, p=0.0252), as can be appreciated in fig. 25 B and fig. 27). On the contrary, NTC+CST proximal dendrite spine density (fig. 25 C) did not significantly differ between the control group and post-injury timepoints ($F_{(5, 95)}$ =0.7345, p=0.5994).

Considering the distal segment, I observed a significant interaction effect of neuron type and TBI on spine density (2-way ANOVA: $F_{(5, 172)} = 3.369$, p=0.0063) (fig. 28 A). NTC+CST distal dendrites have higher spine density than TC at 7dpi (Sidak's post-hoc: mean diff. = 0.7742 ± 0.2021, p=0.0011), as illustrated by representative images in fig. 29 C, D. Subsequently, looking at TC neurons I found significant variance in distal spine density among post-injury timepoints (1-way ANOVA: $F_{(5, 63)} = 3.91$, p=0.0038). More specifically, spine density at 7dpi is significantly lower than 2dpi (Tukey's post-hoc: mean diff. =0.9249 ± 0.2331, p=0.0025), as shown in fig. 28 B and fig. 29 B, C. On the other hand, NTC+CST neurons (fig. 28 C) did not

significantly vary in distal spine density across post-injury timepoints (1-way ANOVA: $F_{(5, 109)}$ = 0.7119, p=0.6158)
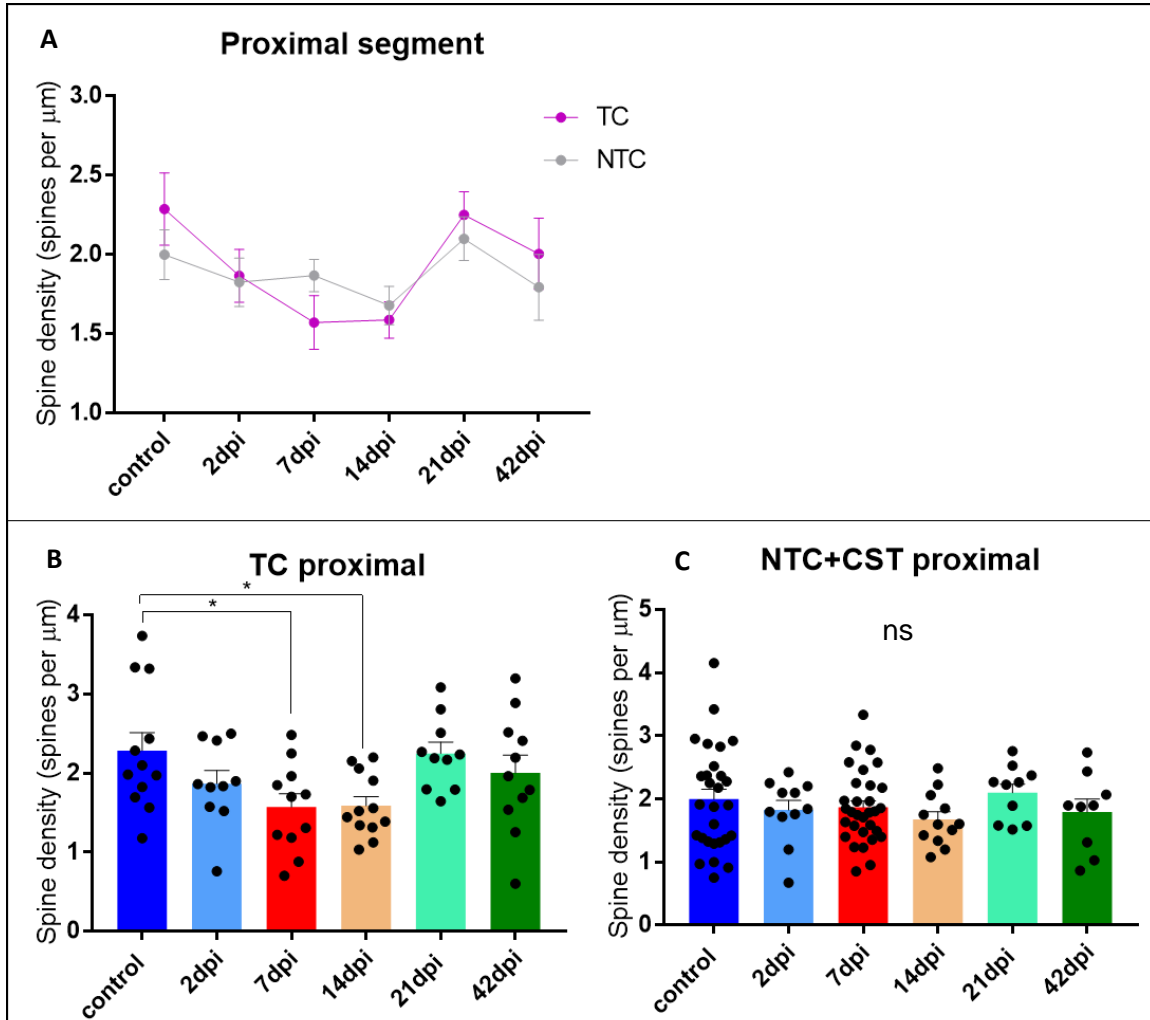
Figure 25 A. Mean proximal dendrite spine density of TC population plotted against NTC+CST$_{control,7dpi}$ population across post-injury timepoint groups. No significant difference between the two populations was detected using 2-way ANOVA. **B.** Lower mean spine density at 7dpi and 14dpi compared to control for TC proximal dendritic segments (Dunnett's multiple comparisons test). **C.** No significant difference between timepoint groups for NTC+CST shown using Dunnett's multiple comparisons test. Control and 7dpi groups contain NTC+CST neurons. Each dot represents one dendritic segment. N (TC): control=5 mice/ n=13 2dpi=5 mice/n=10, 7dpi=5 mice/n=11, 14dpi=5 mice/n=12 21dpi=5 mice/n=10 42dpi=4 mice/n=11. N (NTC+CST): control=10 mice/n=29, 2dpi=5 mice/n=11, 7dpi=9 mice/n=32, 14dpi=5 mice/n=12, 21dpi=4 mice/n=10, 42dpi=4 mice/n=9. Error bars: SEM * p<0.05, **p<0.01
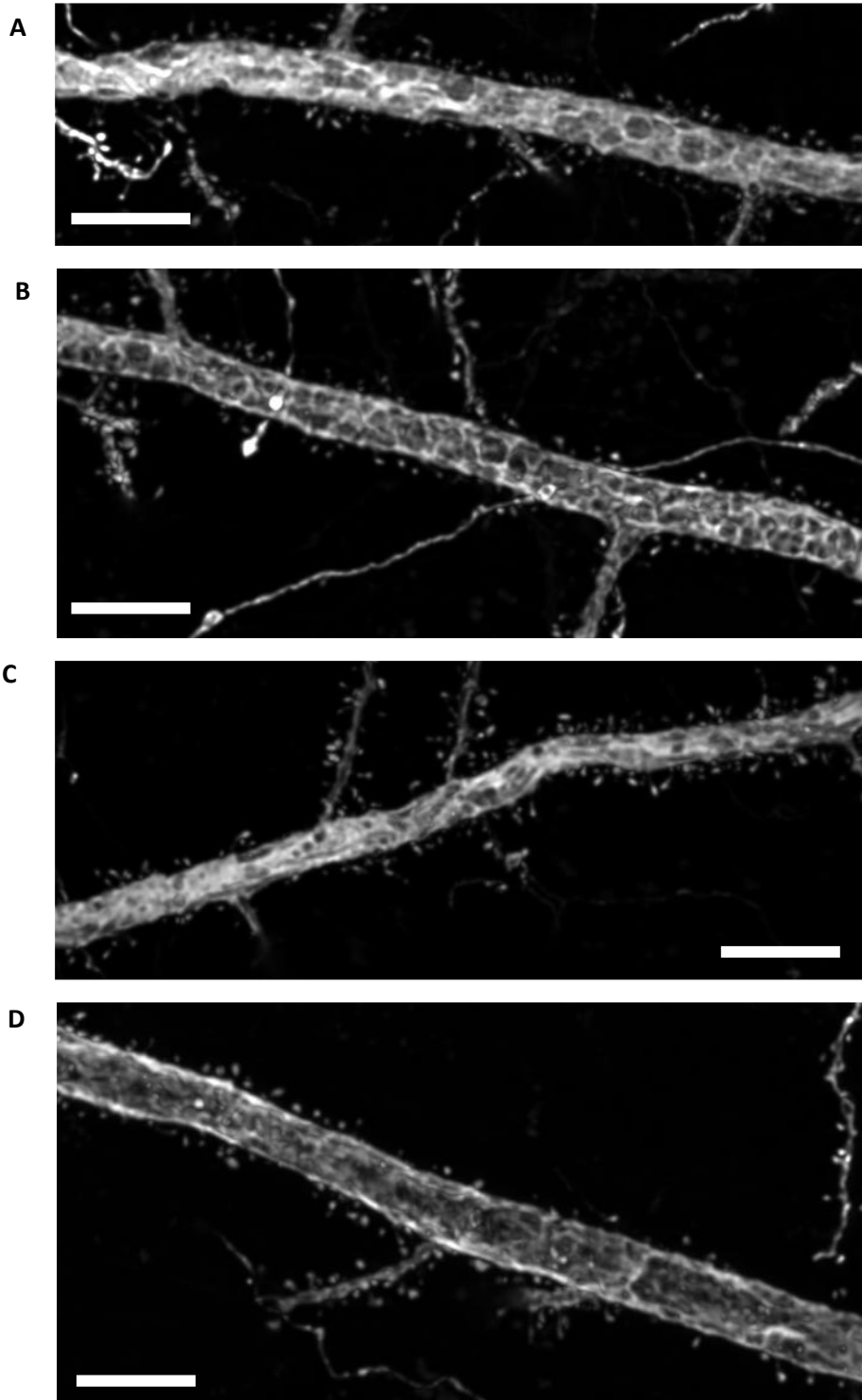
Figure 26. Representative images of proximal dendrite segments. (A) Control group, CST neuron (B) Control group, NTC neuron. (C) 7dpi group, CST neuron (D) 7dpi group, NTC neuron. De-convolved Z-projection of Olympus confocal scans acquired with 60x objective zoom of 3.5 and 800x800 quality, Kalman of 2. Scale bars: ~ 10 μm
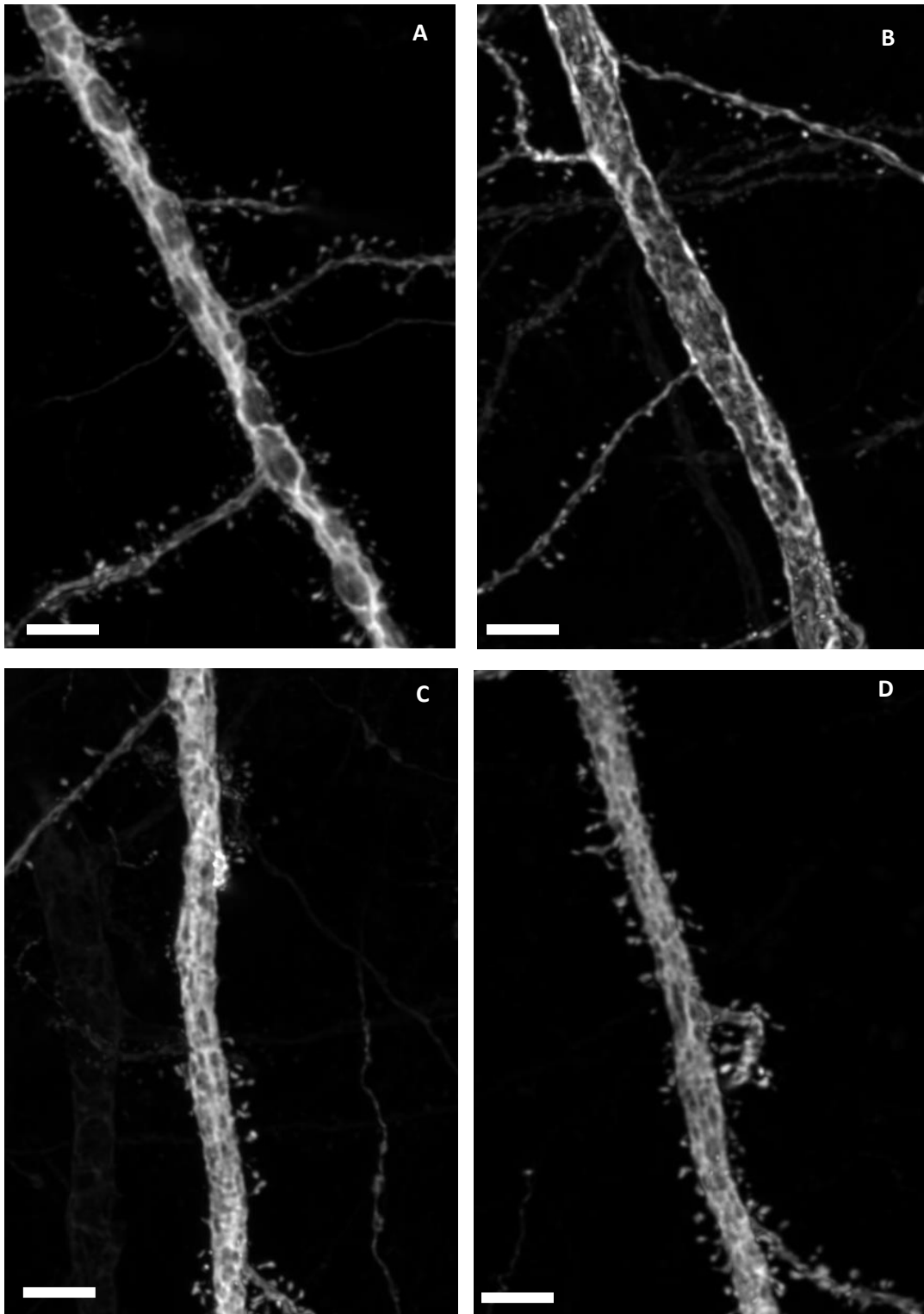
Figure 27. Representative images of TC proximal dendrite segments for control (A), 7dpi (B), 14dpi (C) and 21dpi (D) groups. De-convolved Z-projection of Olympus confocal scans acquired with 60x objective zoom of 3.5 and 800x800 quality, Kalman of 2. Scale bars: ~ 5μm
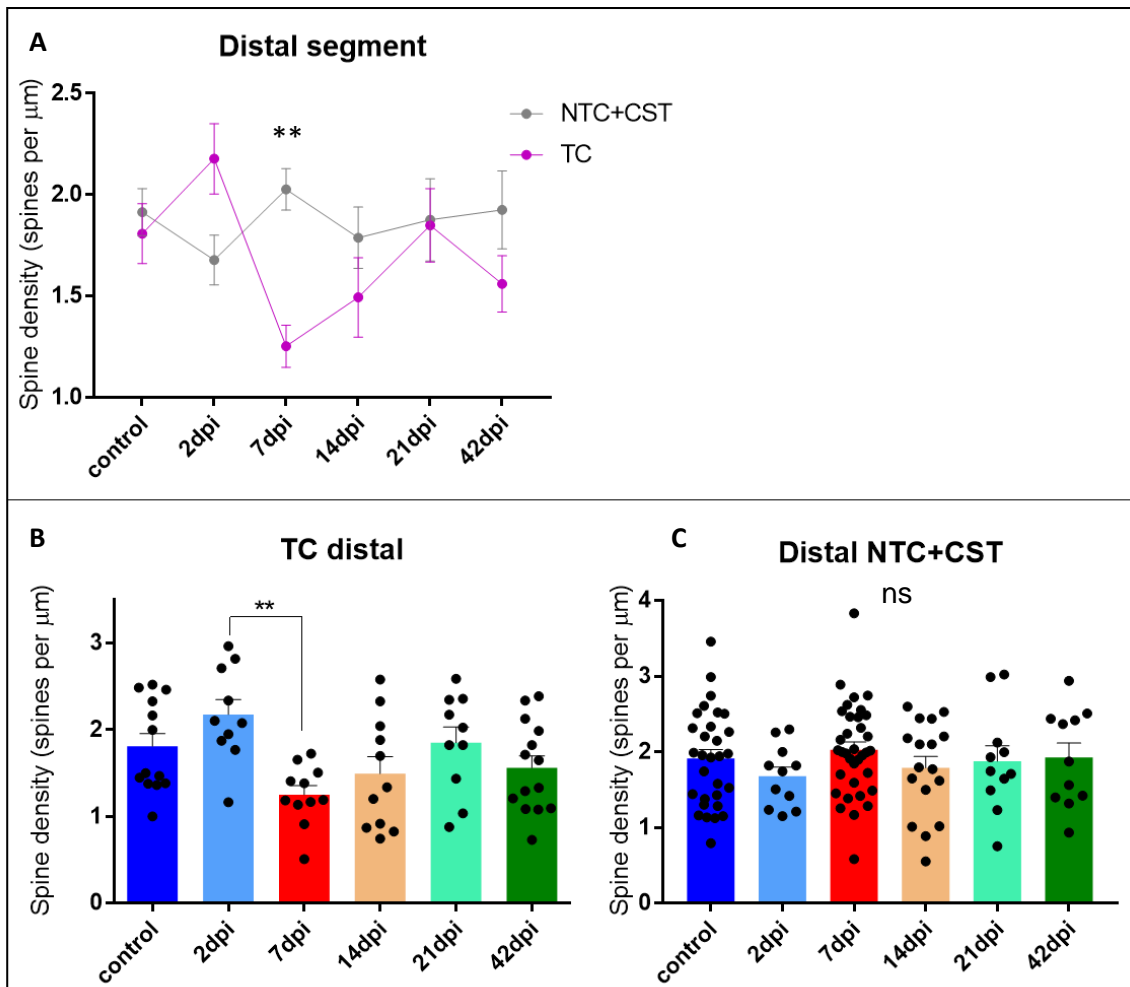
Figure 28. A. Mean distal dendrite spine density of TC population plotted against NTC+CST$_{control, 7dpi}$ population across post-injury timepoint groups. Significantly higher spine density in NTC compared to TC at 7dpi identified using 2-way ANOVA followed Sidak's post hoc test. **B.** Significant effect of post-injury timepoint on distal spine density detected by 1-way ANOVA. Lower mean spine density at 7dpi compared to 2dpi for TC distal dendritic segments (Tukey's multiple comparisons test). **C.** No significant variance in distal spine density among post-injury timepoint groups for NTC+CST identified with 1-way ANOVA. Control and 7dpi groups contain NTC+CST neurons. Each dot represents one dendritic segment. N (TC): control= 5 mice/n=13, 2dpi=5 mice/n=10, 7dpi=4 mice/n=11 14dpi=4 mice/n=11, 21dpi=5 mice/n=10, 42dpi=4 mice/n=14. N (NTC+CST$_{control,7dpi}$): control=9 mice/n=30, 2dpi=5 mice/n=11, 7dpi=9 mice/n=33, 14dpi=6 mice/n=16, 21dpi=5 mice/n=11, 42dpi=4 mice/n=10. Error bars: SEM; **p<0.01
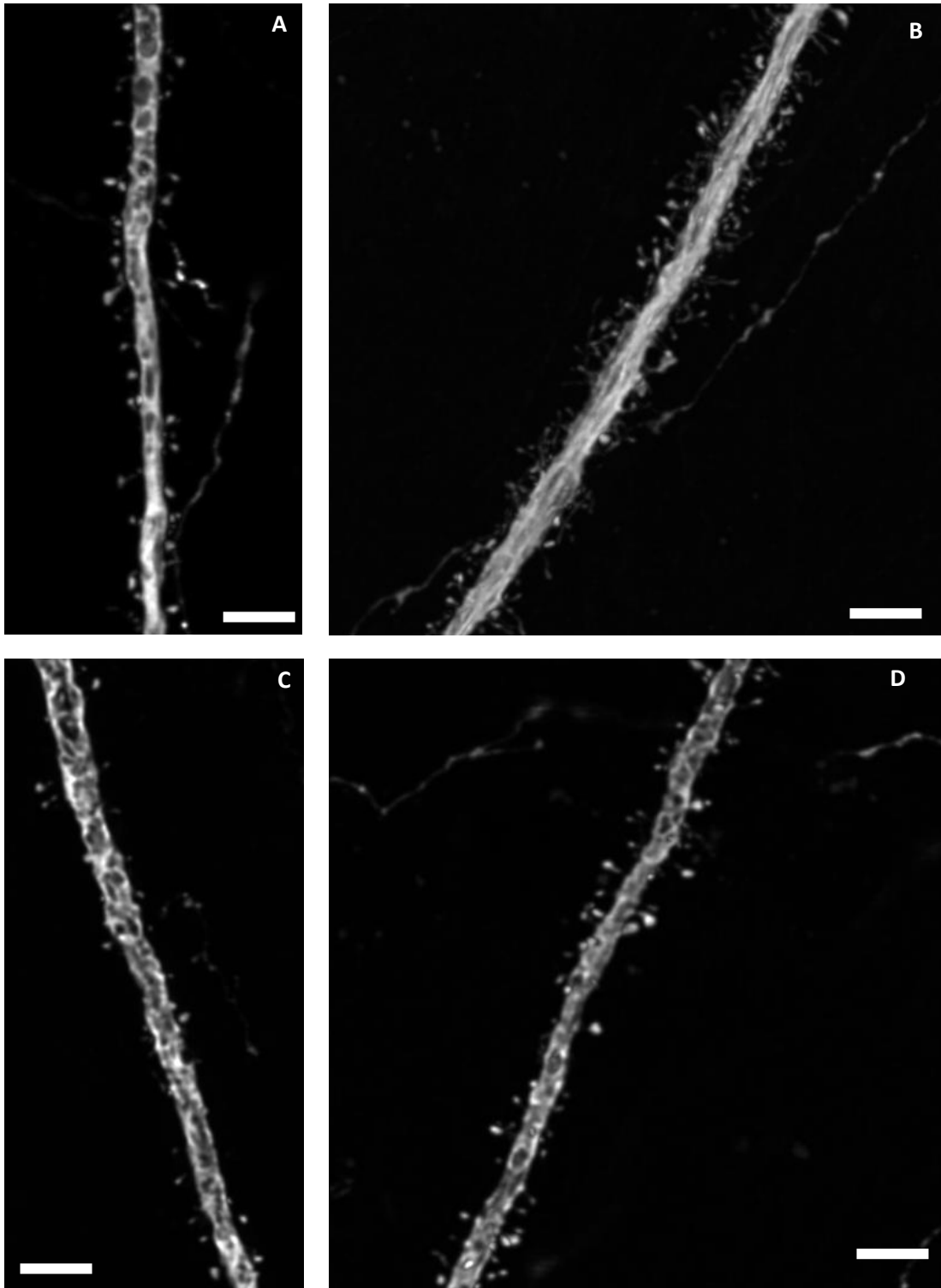
Figure 29. Representative images of TC distal dendrite segments for control (A), 2dpi (B) and 7dpi (C) and NTC distal segment at 7dpi (D). Deconvolved Z-projection of Olympus confocal scans acquired with 60x objective zoom of 3.5 and 800x800 quality, Kalman of 2. Scale bars: ~5µm

Finally, with regards to the apical tuft segment, I showed that neuron type is a source of variation in spine density (2-way ANOVA: $F_{(1, 138)} = 7.535$, p=0.0069) and that there is an interaction between neuron type and TBI (2-way ANOVA: $F_{(5, 138)} = 2.313$, p=0.0471). Using subsequent multiple comparisons, I detected significantly higher spine density for NTC compared to TC neurons at 14dpi (Sidak's post-hoc: mean diff= 0.4809 ± 0.1425, p=0.0058), as can be appreciated in fig. 30 A and fig. 32. Examining the populations separately, I found a significant effect of TBI (1-way ANOVA: $F_{(5, 51)} = 2.942$, p=0.0208) on apical tuft spine density at different timepoints. As can be observed in fig. 30 B and fig. 31, 14dpi and 21dpi groups had lower spine density compared to the control group but returned to normal at 42dpi (Sidak's post-hoc: mean $\text{diff}_{\text{control-14dpi}}$ = 0.329 ± 0.1318, p=0.0158, mean $\text{diff}_{\text{control-21dpi}}$ = 0.2977 ± 0.1242, p= 0.0203, mean $\text{diff}_{\text{21dpi-42dpi}}$= 0.3132 ± 0.1242, p=0.0149). However, there was no TBI effect on the apical tuft spine density of NTC neurons at any timepoint (1-way ANOVA: $F_{(5, 87)} = 0.9366$, p=0.4615) (fig. 30 C).
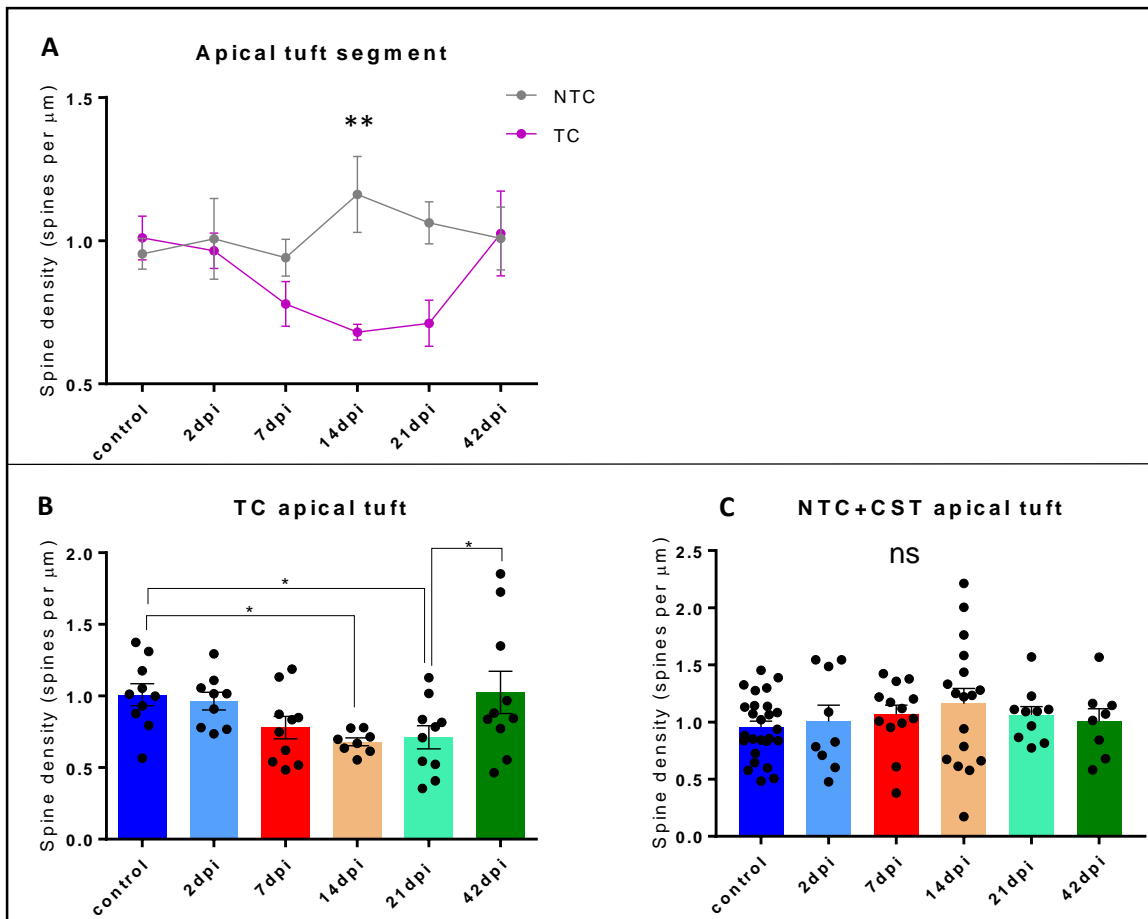
Figure 30. **A.** Mean apical tuft dendrite spine density of TC population plotted against NTC+CST$_{control,7dpi}$ population across post-injury timepoint groups. Significantly higher spine density in NTC compared to TC at 14dpi (2-way ANOVA followed by Sidak's post hoc). **B.** Significant effect of post-injury timepoint on TC apical tuft spine density detected by 1-way ANOVA. Lower mean spine density at 14 and 21dpi compared to control (Sidak's multiple comparisons test). **C.** No significant variance in spine density of the apical tuft among post-injury timepoint groups for NTC+CST identified using 1-way ANOVA. Control and 7dpi groups contain NTC+CST neurons. Each dot represents one dendritic segment. N (TC): control= 5 mice (n=10, 2dpi=5 mice/n=9, 7dpi=4 mice/n=10, 14dpi=4 mice/n=8, 21dpi=5 mice/n=10, 42dpi=4 mice/n=10. N (NTC+CST$_{control, 7dpi}$): control=9 mice/n=25, 2dpi=5 mice/n=9, 7dpi=9 mice/n=13, 14dpi=6 mice/n=17, 21dpi=5 mice/n=10, 42dpi=4 mice/n=8. Error bars: SEM; * $p < 0.05$, **$p < 0.01$
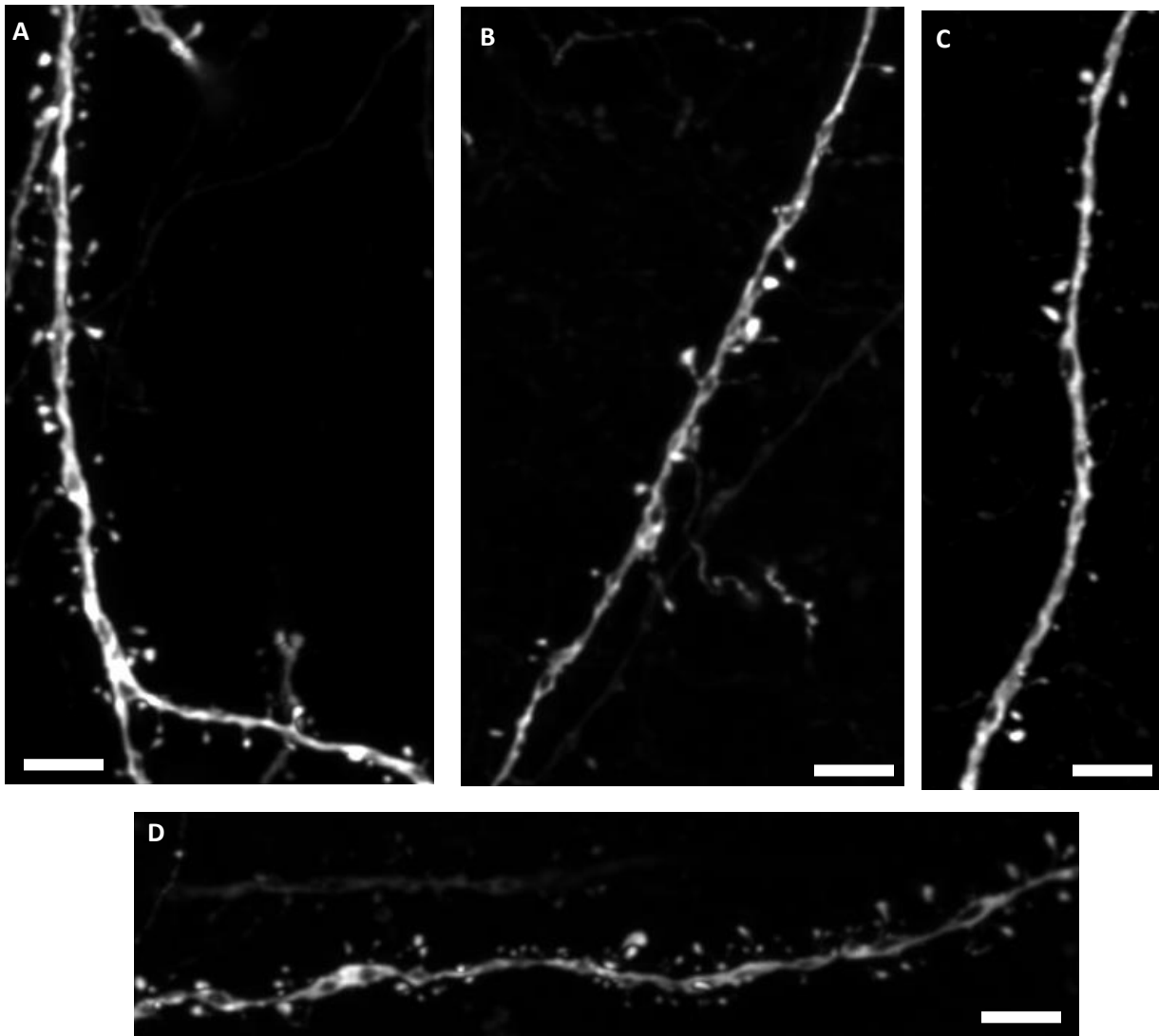
Figure 31. Representative images of TC apical tuft dendrite segments for control (A), 14dpi (B) and 21dpi (C) and 42dpi(D). Deconvolved Z-projection of Olympus confocal scans acquired with 60x objective zoom of 3.5 and 800x800 quality, Kalman of 2. Scale bars: ~ 5µm
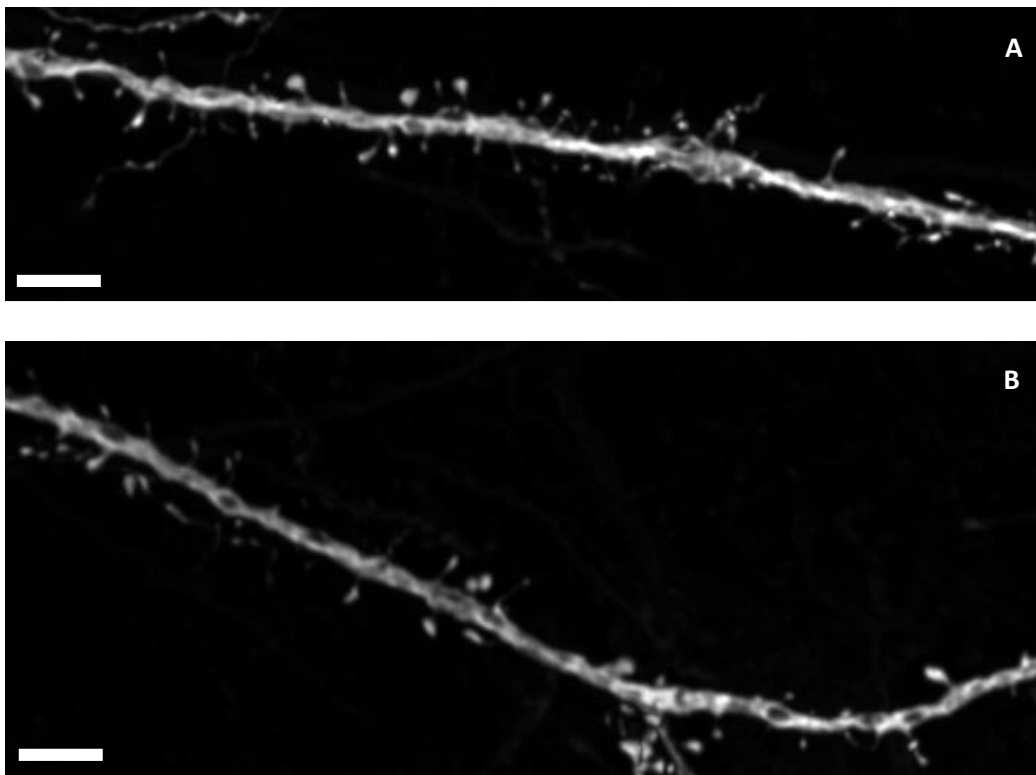
Figure 32. Representative images of NTC (A), and TC (B) apical tuft dendrite segments at 14dpi. Deconvolved Z-projection of Olympus confocal scans acquired with 60x objective zoom of 3.5 and 800x800 quality, Kalman of 2. Scale bars: ~5µm

In brief, dendritic spine density of the NTC+CST population is not altered by TBI across timepoints. However, spine density in TC dendrites is influenced by TBI in a time-dependent way, but the effect varies with distance from soma. The proximal dendrite shows a drop in spine numbers at 7dpi and 14dpi that returns to control levels at 21dpi. The distal TC dendrite is characterized by low spine density at 7dpi, but the difference is significant only when compared to the 2dpi group. Finally, the apical tuft segment displays a delayed –compared to the proximal- spine density reduction that only starts at 14dpi but persists at 21dpi until it returns to control levels at 42dpi.

3.2.6 Spine morphology of the dendritic apical tuft at the contralateral cortex is significantly influenced by TBI in a time-dependent manner.

As a subsequent step in my analysis, I investigated whether the changes in spine density are related to a specific type of spine. Spines vary in shape and different morphologies are believed to serve different functions. Interestingly, different spine shapes are associated with different levels of synaptic maturity, therefore spine morphology can provide information about the synaptic dynamics of a dendrite. Spines can be classified according to the presence (pedunculated) or absence (sessile) of a peduncle or neck and according to the shape or size of the spine head. Here, I included three major spine categories that are often implemented in spine classification: Stubby spines (without neck, length to width ratio<1), mushroom spines (with neck, large head diameter), and thin spines (with or without neck, length>1µm) (fig. 33 E). The spine recognition and classification was provided by the Neuron Studio (CNIC) software in 3D and the counts for each class of spine were divided by the total number of spines counted, giving the spine type percentage. The spine morphology data for the three dendritic segments were statistically analyzed separately, using one-way ANOVA.
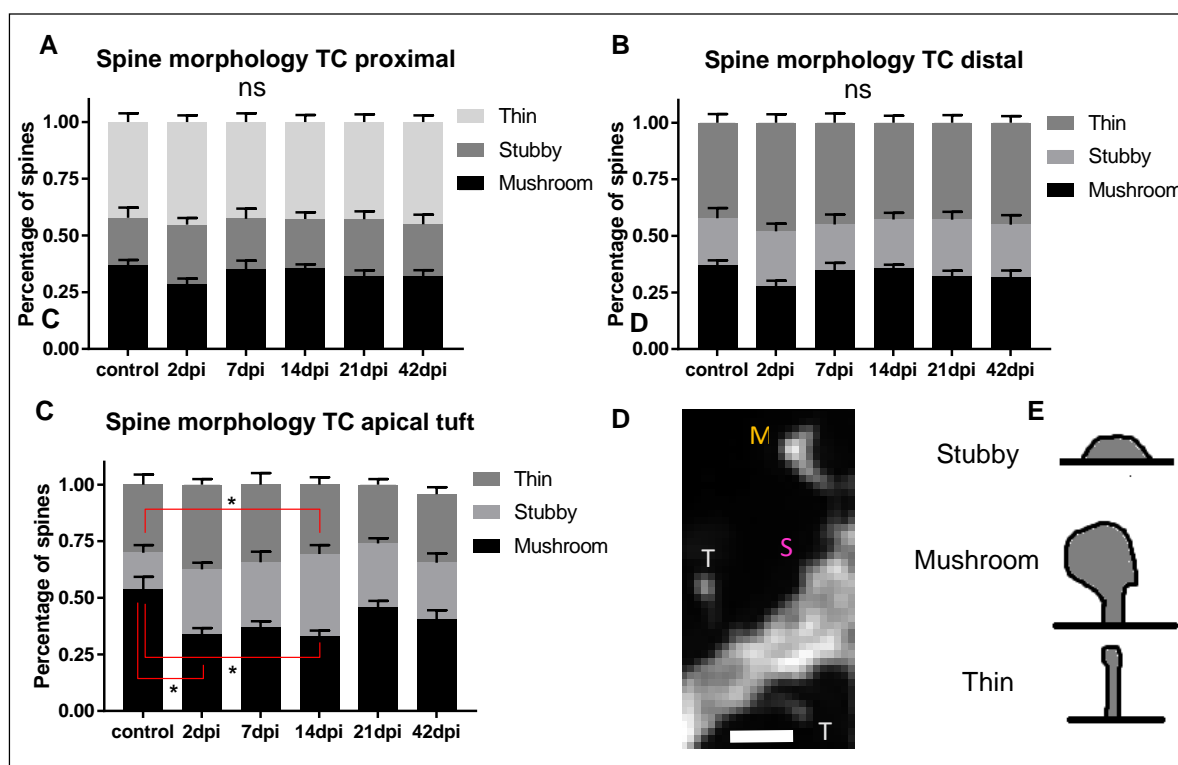
Figure 33. Percentage of different types of spines in TC dendritic segments across timepoints. **A.** TC proximal **B**. TC distal dendritic segment: no effect of TBI on the percentage of stubby, thin or mushroom spines (1-way ANOVA per spine category). **C.** TC apical tuft segment: Significant effect of post-injury timepoint on the percentage of mushroom and stubby but not thin spines (1-way ANOVA per spine category). **D.** Example zoomed image of a dendritic piece containing the three different spine shape categories. **E.** Schematic illustration of the three different spine shape categories. control= 10 dendrites, 2dpi= 9 dendrites, 7dpi=8 dendrites, 14dpi= 10 dendrites, 21dpi= 10 dendrites, 42dpi= 7 dendrites. N=5 mice per group; Scale bar: ~ 1μm. Error bars: ±SEM, * p<0.05, **p<0.01

My results showed that spine morphology, specifically at the dendritic apical tuft, was altered by TBI for both TC and NTC+CST neurons. Regarding the TC apical tuft segment, the percentage of stubby [F (5, 44) = 3.504, p=0.0094] and mushroom [F (5, 45) = 4.94, p=0.0011] spines showed significant variance across post-injury timepoint groups. Using subsequent Tukey's multiple comparisons tests, I showed that the percentage of stubby spines was significantly higher in the 14dpi group compared to control (mean diff.=0.2035 ± 0.0498, p=0.0024), while the percentage of mushroom spines was significantly lower at 2dpi and 14dpi compared to control (mean diff.$_{control-2dpi}$=0.2007 ± 0.0508, p=0.0035, mean diff.$_{control-14dpi}$= 0.2093 ± 0.04959, p=0.0015), as shown in fig. 33 C. On the contrary, the spine morphology in TC neurons at the proximal and distal dendrite was not influenced by TBI at any post-injury timepoint (fig 33 A, B).

In the case of NTC+CST neurons, the percentage of stubby spines at the apical tuft was altered by TBI (1-way ANOVA: F (5, 78) = 2.341, p=0.0492). As can be appreciated in fig. 34 C, I identified significantly higher percentage of stubby spines at 42dpi compared to control (Tukey's multiple comparisons: mean diff.$_{control-42dpi}$ =0.1246 ± 0.04234, p=0.0493). Again, as was the case for TC neurons, the proximal and distal NTC+CST segments did not show significant changes in spine morphology after TBI (fig. 34 A, B).
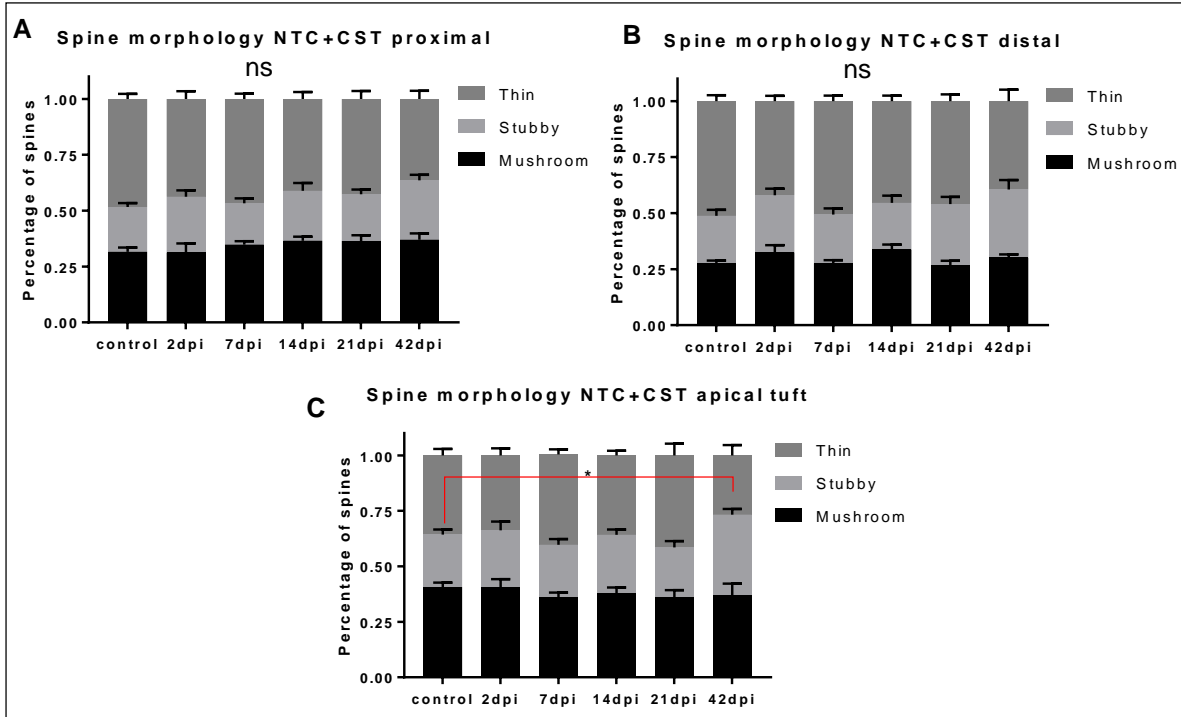
Figure 34. Percentage of different types of spines in NTC+CST$_{control,7dpi}$ dendritic segments across timepoints. **A**. NTC+CST proximal **B**. NTC+CST distal dendritic segment: no effect of TBI on the percentage of stubby, thin or mushroom spines (1-way ANOVA per spine category). **C.** NTC+CST apical tuft segment: Significant effect of post-injury timepoint on the percentage of stubby spines only (1-way ANOVA per spine category). n: control=24 dendrites, 2dpi=11 dendrites, 7dpi=26 dendrites, 14dpi=12 dendrites, 21dpi= 10 dendrites, 42dpi=8 dendrites (originating from 9-10 mice per group for control and 7dpi and 4-5 mice per group for the other post-injury timepoints). Error bars: SEM, *p<0.05

In summary, the apical tuft dendrite seems to be more susceptible to spine morphology changes induced by TBI in TC neurons, with the percentage of mushroom spines being reduced early after TBI. At 14 dpi, which is the timepoint-group that showed significant spine density decrease in the apical tuft of TC neurons, there is also an apical tuft-specific reduction of mushroom spine percentage with simultaneous increase in stubby spine percentage. In NTC+CST neurons, only the spine morphology of the apical tuft is altered as a result of the TBI (as was the case for the TC population) but only at the latest timepoint, in which stubby spines tend to increase in percentage.

3.3 Monosynaptic rabies virus tracing for reconstruction of transcallosal neuron circuitry to study remodeling after TBI: Subtle TBI-induced and time-dependent connectivity changes identified.

The details on the specific contribution to the results presented in this chapter are presented in Table13 below.

Table 13: Specific contribution to the data presented in 3.3

Conception and design of study	Florence Bareyre	Alexandra Chovsepian	Laura Empl
Acquisition of data Stereotactic brain injections Induction of trauma Animal perfusions Tissue processing (IHC) Image acquisition Image processing and analysis	Alexandra Chovsepian Alexandra Chovsepian Alexandra Chovsepian Alexandra Chovsepian Alexandra Chovsepian Alexandra Chovsepian	Laura Empl Laura Empl Laura Empl Laura Empl	 Sanofer Abdul Salaam Sanofer Abdul Salaam
Interpretation of data and statistical evaluation	Alexandra Chovsepian		

After revealing significant spine density recovery and re-establishment of mature spines at late timepoints after TBI that followed the early injury-induced spine loss, I asked whether this late spine recovery could be associated with a general remodeling of the TC circuitry. To answer that question, the first order presynaptic connections of TC neurons were investigated in healthy control and in injured mice at an early and late timepoint after mild TBI. For that purpose, I took advantage of the monosynaptic retrograde tracer the SAD-ΔG-mcherry (EnvA) Rabies virus. Using this virus to exclusively infect the pre-selected TC population of the intact cortex, together with G-protein complementation (provided by a green fluorescent AAV) to allow for trans-synaptic transfer of the rabies virus, it was possible to distinctively label the majority of TC neurons and their pre-synaptic partners, enabling the discrimination between the two populations. As can be appreciated in fig. 35, this results in 3 types of labeling: Yellow cells comprising the starter TC cell population, red cells which are the presynaptic partners of the TC starter cells and green cells that are TC neurons which did not get infected by the rabies virus and therefore do not provide any useful connectivity information. This study included non-injured mice (control group) and mice that underwent mild controlled cortical impact and were sacrificed at day 7 after the injury (TBI 7d group) or at day 42 after the injury (TBI 42d group). The control animals time-matched the TBI animals, therefore there was a 7d control group and a 42d control group.
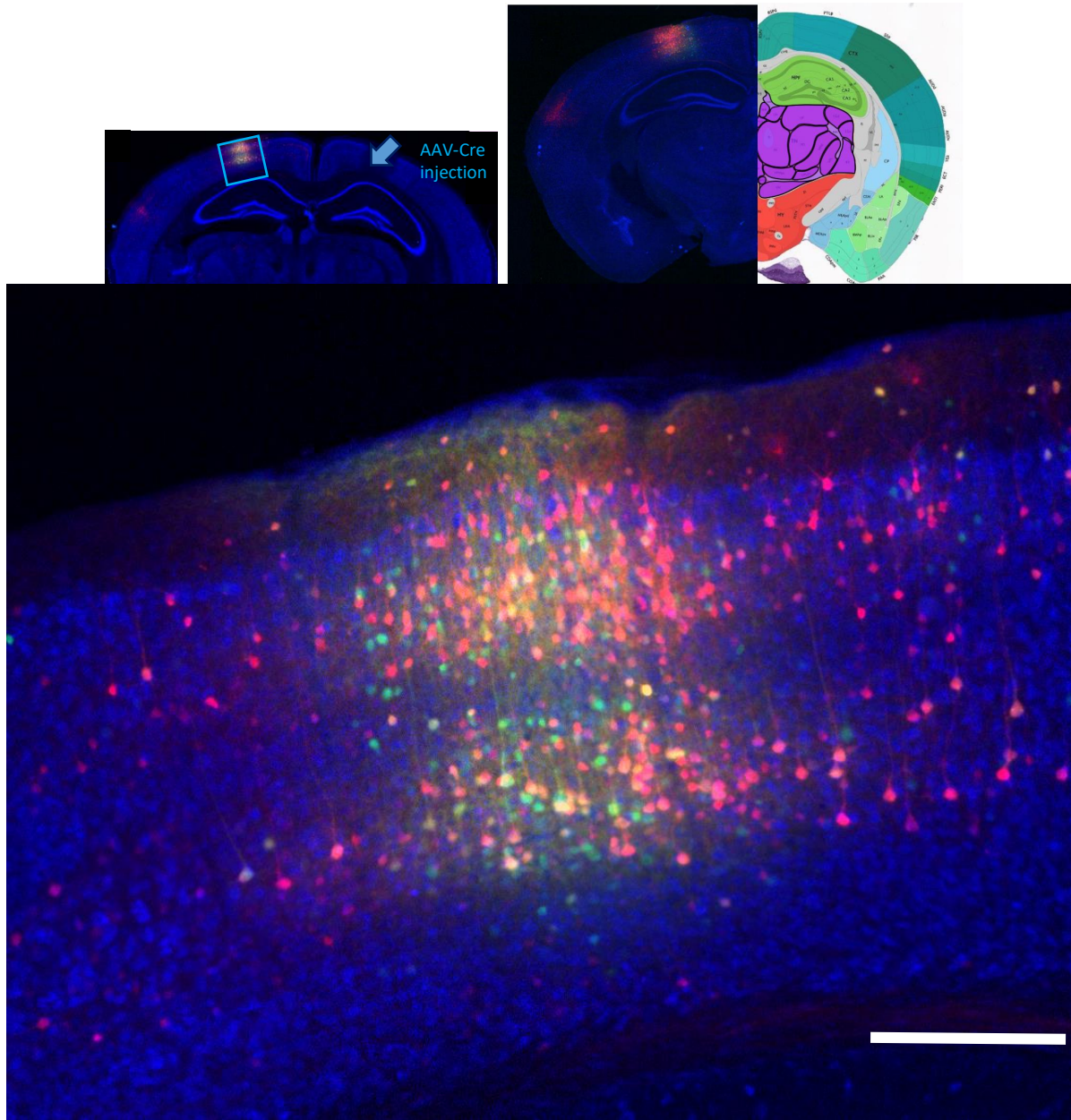
Figure 35. Representative images of a control brain sections including starter cells (yellow), presynaptic cells (red) and TC non-rabies infected neurons (green). **Upper:** (Left) Low magnification image (2.5x objective) acquired using Leica DM4 inverted microscope. Boxed area: PTLp area with high starter and presynaptic cell density. (Right) Example of area definition according to the Allen mouse brain atlas (Image credit: Allen Institute). **Lower:** Higher magnification of the boxed area, acquired using DM4, 10x magnification. Representative better resolution image for quantifying crowded areas. Scale bar: 500 µm

First of all, the lesion volume in all experimental animals was evaluated. According to these measurements, there is no significant difference (p= 0.4343) between the lesion volumes in the 7d -TBI group (2.836 ± 0.6202) and in the 42d-TBI group (2.251 ± 0.4177).

The lesion volume characterization was followed by an estimation of the total number of starter cells per animal, which was accomplished by quantifying 20x-magnification confocal scans (fig 36) of 6 sections per brain, with the sections before and after having ~0 starter cells. The interpolation of the total starter cell number was performed using polynomial curve fitting, as described in detail in the materials and methods chapter. The spread and total number of starter cells across mice was analyzed and outliers were removed, to ensure that the starter cell population has a relatively low variability between animals (fig. 37). Indeed, slight variations in the distribution of starter cells can trigger important variations in presynaptic cells location and number.
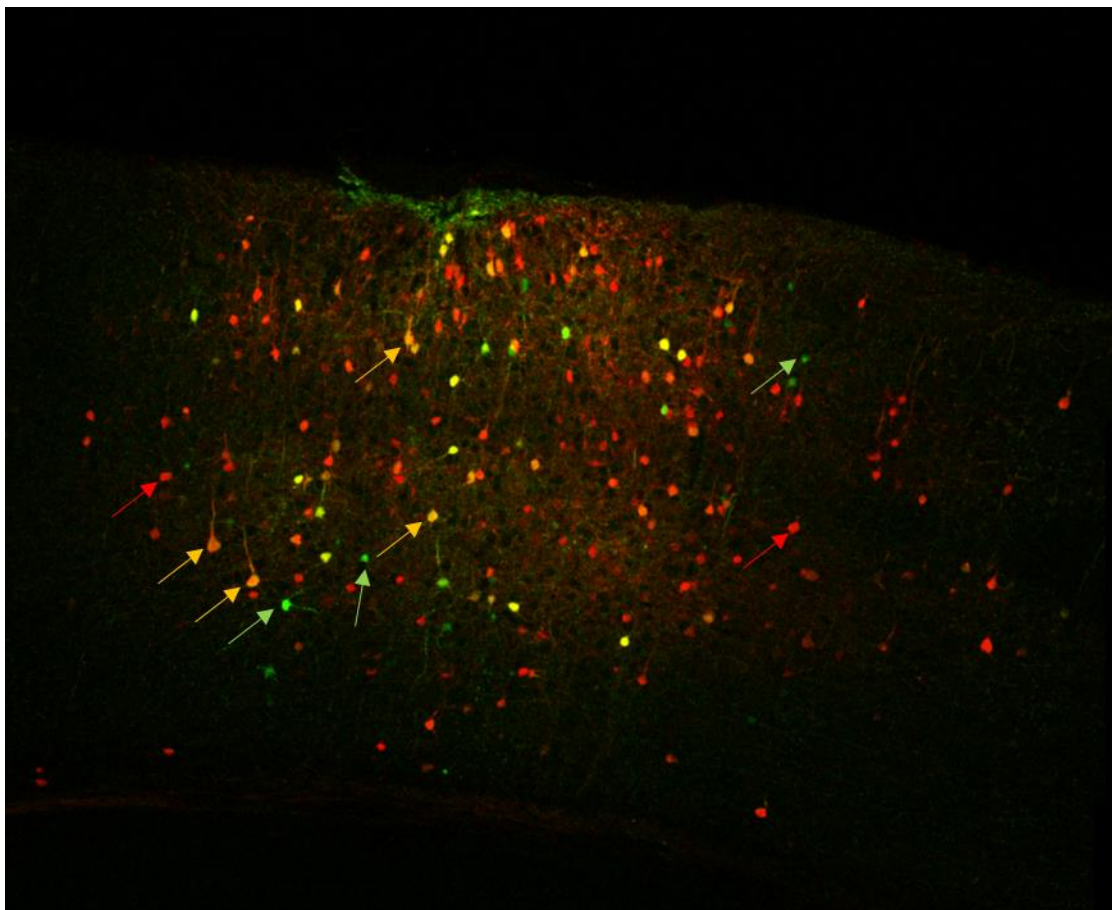
Figure 36. Example high resolution image (single level of a 40µm stack) acquired with Leica sp8 confocal microscope for quantification of starter cells. 20x objective, image resolution of 512x512, Kalman filter, step size of 1.04µm. Yellow arrows show example starter cells, red arrows show example presynaptic cells and green arrows show TC cells that are non-rabies infected. Scale bar: 500 µm

The number of presynaptic cells was then quantified on coronal sections in each distinct brain area containing presynaptic cells, by sampling every 200 μm in the rostro-caudal direction. Hence, a total of 20 sections per brain were analyzed, starting from the level corresponding to the Allen mouse brain atlas (© 2011 Allen Institute for Brain Science. Allen Mouse Brain Reference Atlas. Available from: http://mouse.brain-map.org/static/atlas) coronal section #44 to #82. The different brain areas were determined using NeuroTrace staining, with accordance to the corresponding Allen mouse brain atlas-coronal section. (fig. 35 upper, right).
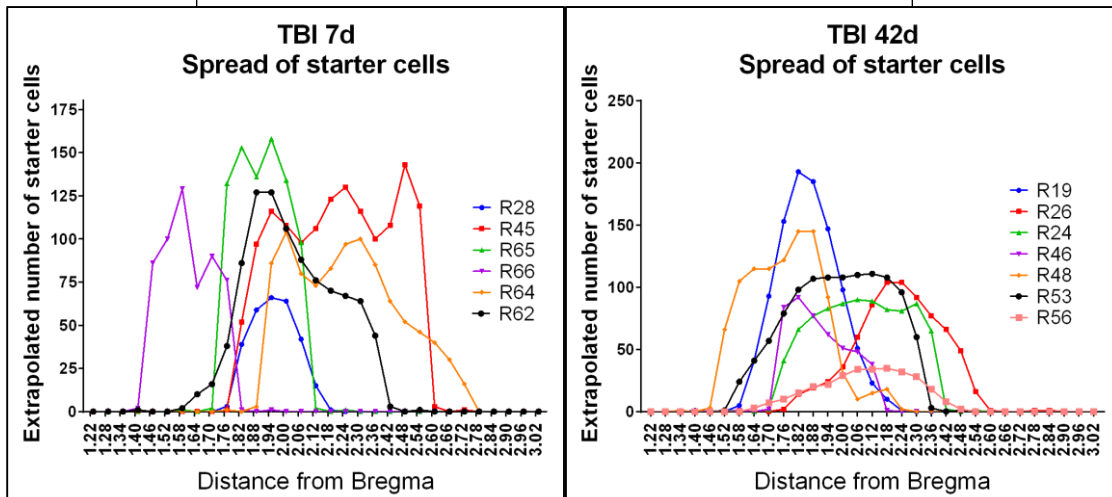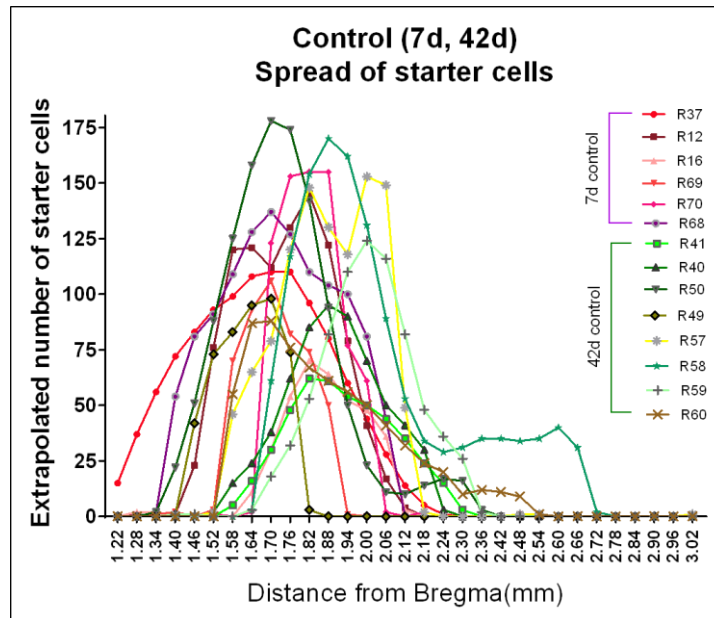
Figure 37. Interpolated numbers of starter cells across sections, spanning the extent of the cortex that was labeled with GFP. Brains with starter cell spread beyond 1.22mm or 2.72mm were excluded from the following presynaptic cell quantification. Coloured lines (R-number) correspond to the different animals included in the final analysis.

Initially, I compared in each brain the total number of starter cells to the total number of presynaptic cells counted. I found that there is a significant correlation between the two (Pearson r= 0.6275, p=0.0002), as can be observed in fig. 38. This reinforces the fact that starter cells need to be tightly distributed to yield reliable results between groups.

Correlation between starter and presynaptic cell number
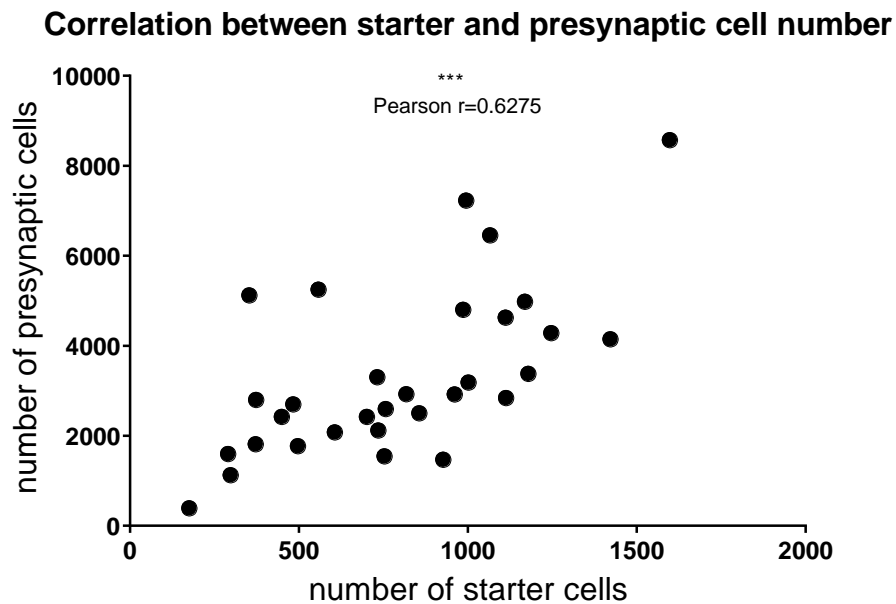
Figure 38. Number of presynaptic cells plotted against the number of starter cells per brain. Significant correlation between the two (r=0.6275). p<0.001

As the number of presynaptic cells correlates with the number of starter cells, I expressed my results as connectivity ratio, which is given by the number of presynaptic cells counted divided by the estimated total number of starter cells. For each distinct brain area (as defined in the Allen mouse brain atlas, © 2011 Allen Institute for Brain Science. Allen Mouse Brain Reference Atlas. Available from: http://mouse.brain-map.org/static/atlas) I calculated the connectivity ratio by dividing the number of presynaptic cells counted inside this area across sections by the estimated total number of starter cells in the brain. Examples of areas containing presynaptic cells in both healthy and injured brains are presented in fig. 39. The connectivity ratio per area for each animal is illustrated in the heatmap of fig. 40. In addition, areas with very low connectivity ratio that displayed changes after TBI are highlighted in the heatmap of fig. 42.
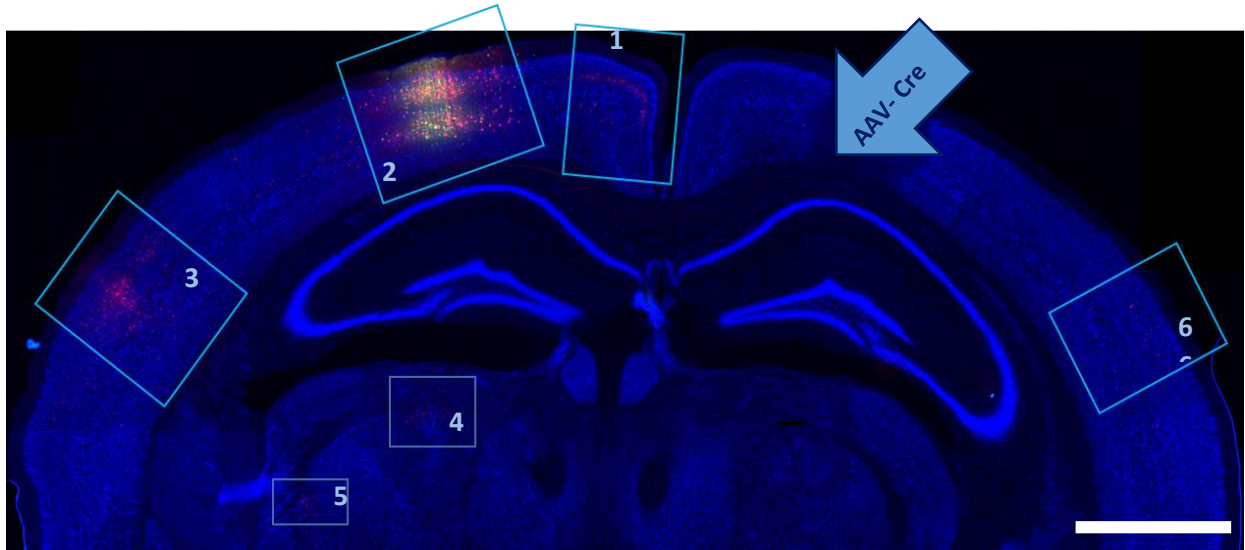
Figure 39. Representative low magnification image for pre-synaptic cell quantification. Control brain section stained with Neurotrace (blue) including starter cells (yellow), presynaptic cells (red) and TC non-rabies infected neurons (green). Boxed areas are all the cortical and subcortical regions that contained pre-synaptic cells in this section. 1: Retrosplenial cortex, 2: Somatosensory cortex, 3: Auditory cortex,4;5: Thalamus, 6: Contralateral auditory cortex. Image acquired using Leica DM4 inverted microscope, 2.5x objective. Scale bar: 1500 μm
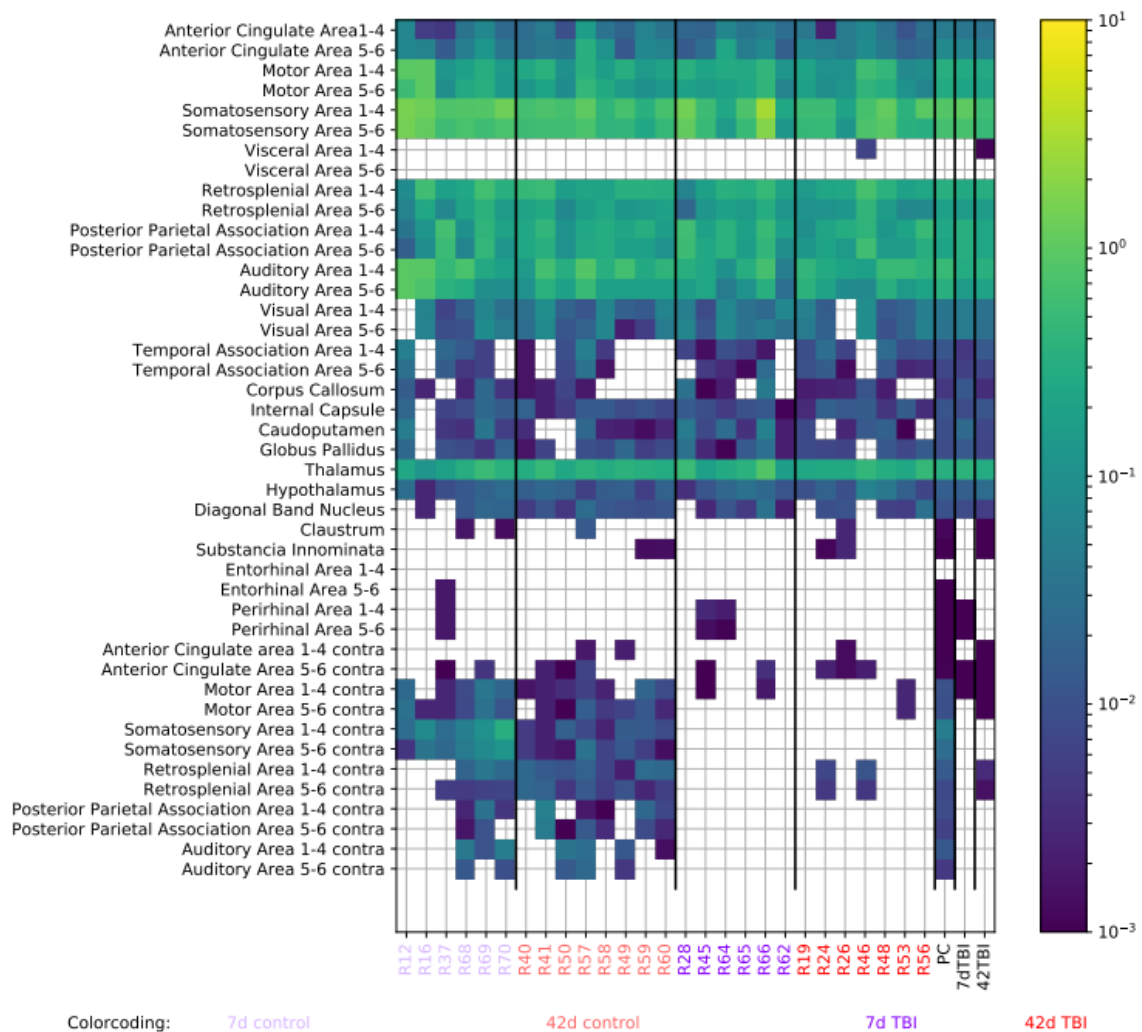
Figure 40. Quantitative heatmap showing the connectivity ratio per area, including all regions that contain presynaptic cells. x axis: individual mice comprising the four different groups (7d control, 42d control, 7d TBI, 42d TBI). The last three points show the median connectivity ratio for the pooled controls (PC), the median connectivity ratio for 7d TBI and the median connectivity ratio for 42d TBI. y axis: different areas quantified, 1-4 signifies the upper cortical layers and 5-6 the lower cortical layers, contra signifies the contralateral to the rabies injection hemisphere (lesioned hemisphere in case of TBI). Script in Python for the generation of the heatmap was provided by Sanofer Abdul-Salaam.

According to the resulting observations, significant connectivity changes in the motor, somatosensory and auditory cortices took place at the different post-injury timepoints (statistical evaluation by 2-way ANOVA and Tukey's post-hoc test). In particular, as can be observed in fig. 41 B, the upper layers of the motor cortex displayed significantly lower connectivity ratio at 42d post-TBI compared to control (mean diff.= 0.0546 ± 0.06274, p=0.0451). The connectivity in the upper somatosensory cortex was changed in a different direction (fig. 41 C): There was a significant decrease at 7d after injury compared to control (mean diff.= 0.1689 ± 0.06274, p= 0.0197) and subsequent increase at 42d after injury (mean diff.= 0.4761 ± 0.06945, p<0.0001). The connectivity ratio at 42d surpassed the control levels (mean diff.= 0.3072 ± 0.05699, p<0.0001). On the contrary, the layers 5-6 of the somatosensory cortex (fig. 41 D) showed higher connectivity ratio at 7d compared to 42d after injury (mean diff.= 0.2884 ± 0.06945, p=0.0001), with the connectivity ratio at 42d being significantly lower than control levels.
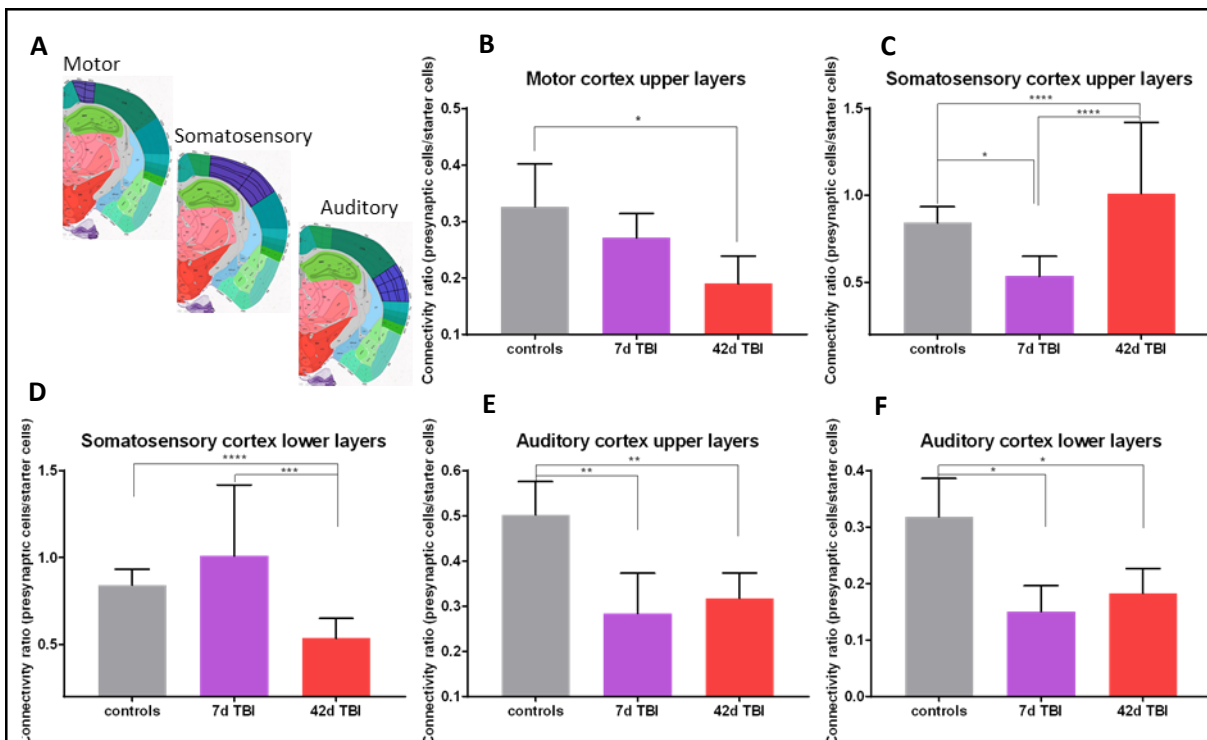
Figure 41. Average connectivity ratio per area, for regions identified by 2-way ANOVA and subsequent Tukey's multiple comparisons to be different after TBI. **A.** Definition of motor, somatosensory and auditory cortex shown in purple according to Allen brain atlas (Image credit: Allen Institute). **B.** Connectivity ratio in layers 1-4 of the motor cortex is significantly lower at the late timepoint after TBI. **C.** Somatosensory cortex 1-4 layers: significant decrease in connectivity ratio at 7d post-TBI which is reversed at 42d post-TBI reaching higher levels than control. **D.** Somatosensory cortex 5-6 layers: Connectivity at the late timepoint is significantly lower compared to control and the early timepoint group. In layers 1-4 **(E)** and 5-6 **(F)** of the auditory cortex there is a similar reduction at early and late timepoints after TBI. * p<0.05, **p<0.01, ***p<0.001, ****p<0.0001

Moreover, the auditory upper and lower cortical layers displayed a significant reduction in connectivity at both timepoints after TBI, as shown in fig. 41 D and E (Layers 1-4: mean diff $_{\text{control-TBI7d}}$= 0.2183 ± 0.06274, p=0.0015, mean diff $_{\text{control-TBI42d}}$= 0.1849 ± 0.05699, p= 0.0035. Layers 5-6: mean diff $_{\text{control-TBI7d}}$= 0.1679 ±,0.06274, p=0.0207, mean diff $_{\text{control-TBI42d}}$= 0.1358 ± 0.05699, p=0.0457).

Figure 42. Selected areas from the heatmap presented in fig. 40. Above red line: Highly crowded areas that show significant differences in connectivity between groups as revealed by 2-way ANOVA. Below red line: Less crowded areas that 'light up' (have at least 3 presynaptic cells) in only one or two of the groups and are therefore not common areas.
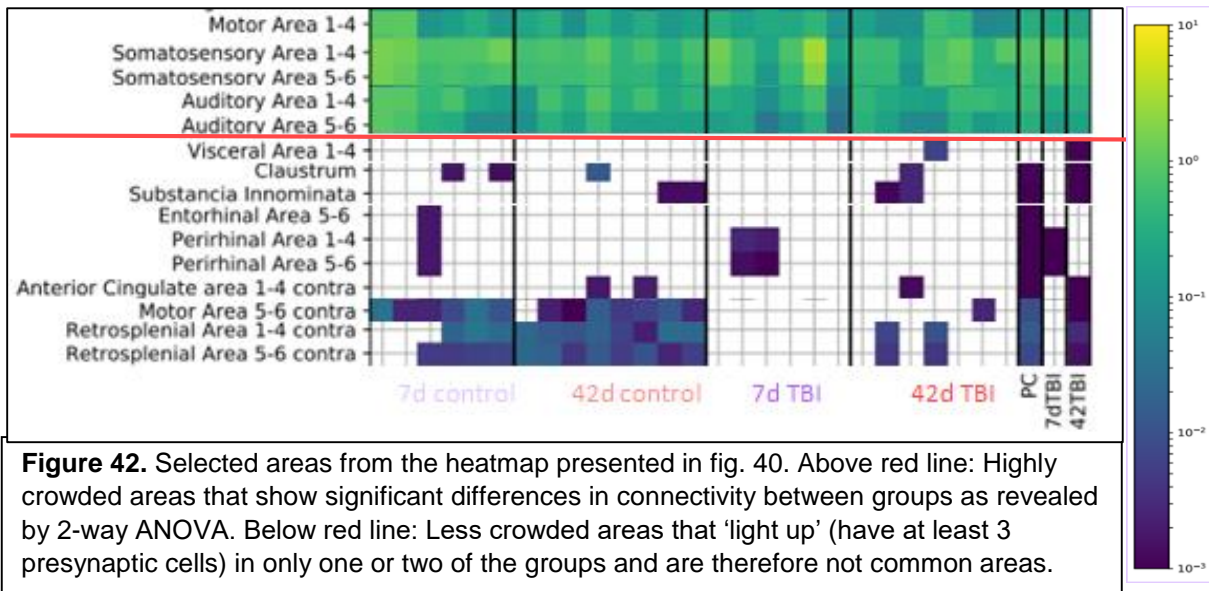
Apart from the area-dependent connectivity analysis, for which the numbers of presynaptic cells in each area were obtained as a sum of the counts from all sections containing that area, a section-wise connectivity analysis was performed where all cells counted in a section were summed, independently of the area they reside in. This analysis gives more insight into the rostro-caudal distribution of presynaptic connections at early and late timepoints after TBI. As can be appreciated in the fig. 43, the distribution of presynaptic cells was similar in all groups up to section 72. More caudally, changes starting from section 74 were evident. Caudally, the changes were amplified with sections 80 and 82 displaying significant differences (2-way ANOVA followed by Tukey's post-hoc) between control and TBI-42d (Section 80: mean diff.= 0.03662 ± 0.008074, p<0.0001. Section 82: mean diff.= 0.03642 ± 0.008074, p<0.0001). In section 82, there was also a significant difference between control and TBI-7d (mean diff= 0.02179 ± 0.00851, p=0.0289). Lastly, I showed that the total connectivity ratio per brain is not correlated to the brain's lesion volume (Pearson's r =0.06534, p=0.8401), meaning that the connectivity results were not influenced by small differences in lesion volume between mice.
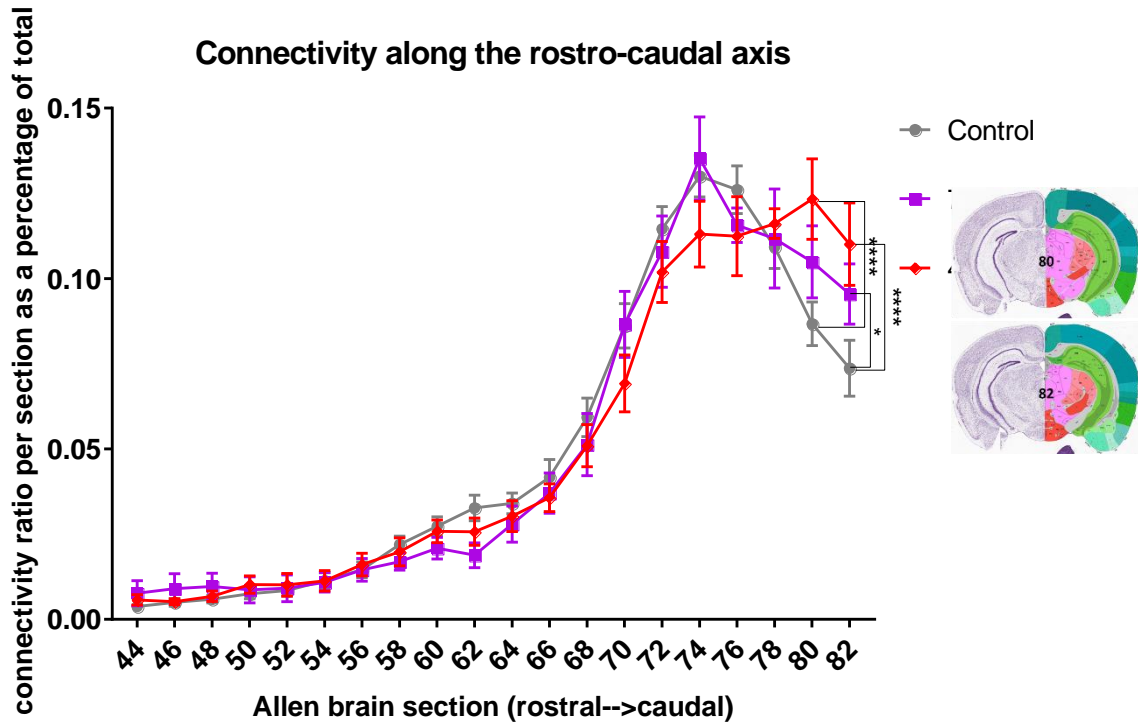
Figure 43. Analysis of connectivity ratio per section along the rostro-caudal axis (different areas summed). Connectivity ratio increases rapidly after Allen section 66 for all groups up to Allen section 74. More caudally, (sections 80 and 82) there are significant differences between groups (Image credit: Allen Institute). For both sections connectivity at 42d TBI is higher than control and for section 82 connectivity at 7d TBI is also higher than control. * p<0.05, ****p<0.0001

Chapter 4: Discussion

4.1 Descriptive study of Transcallosal Neuron distribution across the mouse cortex

In this study, I performed a systematic analysis of the location and organization of transcallosal neurons across the cortex. The goal was to understand whether transcallosal neurons and their axonal projections are uniformly arranged throughout the cortex or whether regions with different functions display different patterns of transcallosal organization. The resulting observations suggest that transcallosal projections maintain a homotopic organization across the cortex but are also found ectopically to a smaller extent. Moreover, their laminar distribution pattern is generally conserved but more strictly in the homotopic area, with the media and lateral adjacent areas showing some extent of variability.

4.1.2 Anterograde tracing showing that transcallosal neurons located in different layers similarly innervate the entire contralateral cortical column

In order to describe in greater detail how the axonal projections of transcallosal neurons are arranged in the contralateral cortex, I implemented standard anterograde tracing techniques. As a starting point, different injection depths were used to examine whether they result in different location of axonal terminals at the contralateral side. Taking into account many studies that have reported transcallosal neuron localization in layer II/III [230] [224] [261] [220] but also in layer V [262], the layer II/III and layer V were selected as the two distinct alternate points for the anterograde tracer injection.

The results suggest that both the homotopic arrangement of transcallosal projections and the laminar distribution of their axon terminals are independent of the injection depth. Nonetheless, it is crucial to highlight that the axonal terminals of transcallosal projection neurons span the entire contralateral cortical column. This observation suggests that both subpopulations of transcallosal neurons, the one residing deeper and the one located more superficially in the cortex send projections to the contralateral cortex that expand more broadly than previously believed. The experimental approach involved injecting a quite high amount of BDA tracer (1.5

µl), to ensure adequate labeling of the transcallosal neurons and their terminal fields. Although this resulted in a certain spread of the tracer to the directly adjacent ipsilateral cortical layers, that spread is not responsible for the wider contralateral distribution of terminals fields to the different layers. Both injection depths generated approximately equal projection patterns and the ipsilateral labeling was mainly evident in the layers targeted for injection (fig 11). An interesting observation is that, layer V injections led to a small increase in numbers of ectopic (outside the homotopic area) axon terminal fields compared to layer II/ III injections. The role of such ectopic projections in inter-hemispheric connectivity could be different than the role of the mainstream homotopic projections and is yet to be investigated.

4.1.3 Retrograde labeling verifies the homotopic organization of transcallosal projection neurons but also manifests distinct heterotopic connections

To study the organization of transcallosal neurons I implemented retrograde tracing techniques, allowing for the determination of transcallosal cell body location across the contralateral cortex. Consistently to several previous findings [231] [220] [263], this study reports that the majority of all retrogradely labeled transcallosal neurons reside in the area homotopic to the injection area. According to the quantifications, the homotopically located transcallosal neurons comprised approximately 67% of the total labeled transcallosal population, demonstrating that a considerable portion of transcallosal neurons is heterotopically organized.

Following that, I examined the laminar distribution of the same transcallosal projection neurons and found that, in agreement with earlier studies [230] [262] [224] [261] [220] most of these transcallosal cell bodies reside in layers II/III and layer V of the contralateral to the injection cortex. A novel finding of the present study is the detection of approximately 20% of labeled transcallosal neurons in layers IV and VI. The aforementioned results concern the area homotopic to the area of injection. An analogous pattern of laminar distribution, with the localization of transcallosal neurons in layers II/III and V being more prominent but not exclusive, was also observed in the medial and lateral adjacent areas. The existence of a substantial proportion of heterotopic transcallosal neurons that exhibit a layer distribution pattern similar to the homotopic ones is an important observation suggesting a potential functional significance of these heterotopic connections in the healthy mouse brain. Taking into consideration that partial callosal agenesis increases the numbers of heterotopic connections

[264], it is reasonable that these neurons may play a crucial role in compensatory functions following callosal impairments inherent or injury-induced.

4.1.4 Localization of transcallosal neurons mainly in layers II/III and V but also in ectopic layers especially in heterotopic areas

Unlike former studies of transcallosal neuron organization ([230] [224]   [261] [231]), that focused on one brain region at a time (part of the somatosensory cortex in most cases), the present study is novel as it investigates the organization of transcallosal connections across different brain regions using a uniform tracing procedure. More specifically, I aimed to understand whether transcallosal connections are homogeneously organized throughout the cortex or whether they exhibit considerable changes in arrangement across structurally and functionally discrete cortical regions. To evaluate the possible inter-regional variability, I performed stereotactic injections at six different brain coordinates (in the rostrocaudal and mediolateral axis) spanning the primary somatosensory and primary motor cortex. According to this study's findings, the transcallosal connections follow a common pattern of organization in all the examined regions, not only in terms of homotopy but also in terms of laminar distribution. In spite of the aforementioned homogeneity, some significant regional differences were also detected: the laminar distribution of transcallosal neurons shows some variability between the primary somatosensory and the primary motor cortex. In particular, regional-related differences were predominantly identified in heterotopically projecting neurons, while homotopically projecting neurons displayed less variability. Therefore, this finding supports the concept that heterotopically projecting neurons could play distinct and crucial functional roles in the primary motor and primary somatosensory cortex.

In summary, the significance of corpus callosum- mediated interhemispheric connectivity for proper brain function is irrefutable and this is evident in patients with callosal agenesis or dysgenesis. The roles of homotopic and heterotopic transcallosal neurons in sensory and motor function may serve distinct purposes and thus react differently in case of pathology. I am confident that the present systematic characterization sets the basis for better understanding of such differences and further underscores that studies should be careful when extrapolating observations about transcallosal connectivity from one region to other brain regions.

4.2 Effects of TBI on the structural integrity of transcallosal neurons located in the contralateral intact cortex

After the systematic characterization of Transcallosal neurons (TC) that provided significant insight into their localization and layer distribution, I used this information to study the effect of TBI on the structural integrity of this anatomically connected to the injury neuronal population residing at the intact cortex. I was specifically interested in determining whether neurons in areas anatomically connected to the brain injury respond differently to neurons located in areas without direct link to the lesion. This would indeed shed light on the principles that guide neuronal and circuit remodeling following injury.

To do so, I made use of the CCI brain injury model which I considered the most suitable choice for this study. Although a closed-head injury model would more accurately replicate the majority of the TBI incidents in humans [265] [266] , I was interested in the effects of a more focal, open skull TBI since ensuring that the contralateral cortex remains intact was a crucial requirement in my study. Closed-head injury models such as the Impact acceleration model, the Rotational acceleration injury model, Blast injury models and the Closed head impact model of engineered rotational acceleration (CHIMERA) are very successful at inducing diffuse axonal injury and bilateral damage but not unilateral focal brain lesion [105] [267] [108] [109] . One reason for selecting the CCI over other open skull models such as the fluid percussion injury model is that the latter can have variable results depending on the installation of the reservoir [104]. Moreover, the open-skull version of the weight-drop injury model was also not regarded as optimal for this study since it is not free of limitations such as unwanted skull fractures (which can increase the severity and induce diffuse injury in addition) and lack of precision on the impact site [103]. Lastly, the CCI was a better option compared to the penetrating TBI model as it is offers higher control over the injury severity, is highly reproducible and very well characterized for its biomechanics [268], as well as its histological and behavioral effects as described in the introduction of this thesis.

I examined the effects of CCI in a time-dependent fashion, looking at ex-vivo brain sections created at 2, 7, 14, 21, 42 and 84 days post-injury (dpi). First, I investigated how the focal injury affects the general state of the contralateral, intact cortex, looking for potential TBI-induced changes in the cortical thickness, cell density and cell body size, while distinguishing between the TC population and other neurons. I found that TBI did not induce any significant contralateral tissue thinning or swelling across the different timepoints. Moreover, there was

only an early and transient minor reduction in contralateral cell density and a restricted cell body swelling for both neuronal populations. I then investigated whether TBI affects the integrity of the dendritic structure, in terms of branching and spine density. Although there was no change in number of branches, I identified a significant and prominent spine loss starting at 1 or 2-weeks post-injury that recovered at 3 or 6-weeks post-injury, depending on the proximity to cell body. This was specific for neurons located in areas anatomically connected to the lesion (TC neurons). Lastly, I could also observe a concomitant shift in spine morphology in the apical tuft dendrite, mostly favoring stubby over mushroom spines in the TC population, which did not persist in long-term.

4.2.1 Cortical thickness, cell density and cell body size at the contralateral cortex after TBI

Following an initial characterization of the TBI lesion volume, which showed low variability between mice, I started my analysis by measuring the thickness of the contralateral cortex, opposite to the lesion, spanning the entire segment of the cortex that has been injured. Although not much is known about the contralateral cortical thickness following TBI, stroke studies have shown contralateral cortical thinning in stroke patients [269] at the onset and 6 months after the incident [270]. However, my results showed no significant TBI-induced changes in cortical thickness despite a tendency for higher thickness at 2dpi. With regards to the contralateral cell density analysis, I observed a transient reduction in cell density at 2dpi that was not statistically significant. This minor and temporary change could be attributed to edema that is known to start in the first 24hrs after the injury in the ipsilateral and contralateral cortices [271] [272] [273] and peak at 72 hours at the contralateral side after mild TBI [271] [272] but resorb after 7dpi [271]. Both vasogenic and cytotoxic edema could explain why the number of cells in a certain area appears smaller briefly after TBI. Subsequently, I wanted to understand whether TBI could also affect the average neuronal soma size and I found no statistically significant difference between groups. The observed tendency for cell body enlargement at 2dpi, more pronounced in NTC neurons, is suggestive of the presence of a mild intracellular edema. Overall, there seems to be a slight and temporary swelling early after TBI that might be attributed to cytotoxic edema but a higher number of animals per group could have enhanced the differences I observed, to reach statistical significance. These results are crucial, as they manifest that there is no apparent cell death in the contralateral intact cortex. Cell death would have precluded the next level of analysis that I aimed to perform as dying neurons exhibit intrinsic changes in their spine density

and morphology. Cell death would not allow for the study of plasticity-related dendritic branching changes and spine recovery. Here, I demonstrate clearly that mild brain injury does not affect significantly the overall cell viability and size of contralateral neurons.

4.2.2 Neurite branching, spine density and spine morphology at the contralateral cortex after TBI in TC and NTC neurons.

Subsequent to the examination of more generic structural changes in the contralateral cortex, I focused on investigating the dendritic morphology of TC vs NTC neurons. In the healthy mouse brain, after a juvenile plasticity time window when neurons establish their dendritic fields, dendrites stabilize and the dendritic fields become permanent for the rest of the adulthood [274]. In any case, the branching density and arrangement has to be appropriate for efficiently receiving and processing inputs converging to the dendritic field [275]. Thus, dendritic capability for adaptation as a reaction to experience is an essential feature and TBI is an event that could induce adaptive or maladaptive changes in dendritic branching density. Although reduced dendritic arborization has been reported at the ipsilateral cortex after injury [276] there is no conclusive evidence on how the dendritic branching of neurons at the intact cortex is influenced by TBI. According to my results regarding contralateral dendritic arborization, I found no differences between control and injured mice at any of the timepoints and both TC and NTC dendrites seemed to be similarly unaffected by the injury. Not only dendrites but also axons have the ability to extend multiple collateral branches in order to communicate with various targets and this process is highly dependent on cytoskeletal dynamics and extracellular cues [277]. Contralateral axon branching could be influenced by TBI not only as a direct result of diffuse traumatic axonal injury, especially in neurons that are anatomically connected to the injury, but also as an outcome of general injury-induced imbalances in growth factors and extracellular cues [278] [279]. According to my results, axon branching was not affected by TBI at an early or late post-injury stage, independently of the neuronal population examined. Taken together, my data regarding neurite arborization suggest that TBI did not induce degeneration on the level of branches.

To further explore the contralateral dendritic structural integrity after TBI, I looked at potential differences in spine density, in response to TBI. I examined dendritic segments at different distances from soma (proximal ~70-150 μm, distal~ 370-450 μm, apical tuft ~ 510-600 μm), distinguishing between layer V TC and NTC neurons. The quantification was performed using

93

the Neuron Studio platform (CNIC) which provides an automated detection and shape classification of dendritic spines in 3D, based on the Rayburst sampling algorithm [256]. The Neuron Studio software (CNIC) enabled the analysis of volumetric data with sufficient precision and therefore the identification of spines that would be undetectable with standard 2D analysis [253]. The average baseline apical dendritic spine density of a Layer V pyramidal neuron (TC or NTC) according to my 3D-based calculations was ~2.2 spines/μm at the proximal segment, ~1.8 spines/μm at the distal segment and ~1 spines/μm in the apical tuft. On the other hand, a 2016 study [280] measuring Layer V pyramidal neuron dendritic spine density also *ex vivo,* but in 2D, reported a much lower spine density of ~0.5 spines/μm for the distal apical dendrite and ~0.3 spines/ μm for the proximal apical dendrite. Therefore, my results underscore the higher accuracy of the 3D- compared to the 2D-analysis. When comparing my results to a recent study [281] that looked at the spine density of Layer V pyramidal neurons in GFPM mice (same mouse line and dendritic labeling as my study), using 3D analysis via MATLAB code, I have identified higher spine densities in the apical tuft. The deviation between their spine density results compared to mine (~0.45 spines/μm vs ~1 spines/μm at the apical tuft) derives from the different imaging methods used: Alexander et al [281] implemented *in vivo* two-photon imaging with 40x objective while I used *ex vivo* confocal imaging with 60x objective and zoom of 3.5 followed by deconvolution. Therefore, the image definition obtained in my study was significantly higher, so detecting more spines than the aforementioned *in vivo* imaging study [281] is not unexpected.

After establishing that at baseline (control, non-injured mice) I achieved an accurate estimation of dendritic spine density for both TC and NTC neurons, I compared these control densities to the densities at different post-injury timepoints. At a short distance from soma (proximal dendritic segment) I found that only TC neurons have significantly reduced spine density after TBI, specifically at day 7 and day 14 post-injury, which returns to control levels by day 21. At an intermediate distance from soma (distal dendritic segment) there is only a significant difference between TC at 2dpi and 7 dpi, with the latter group displaying lower spine density. Lastly, at the longest distance from soma (apical tuft segment) I observed a delayed spine reduction for TC neurons at 14dpi that returned to normal levels at 42dpi. No significant differences in spine density between control and TBI at different timepoints were observed for NTC neurons.

Overall, it seems that TC neurons have a greater sensitivity to TBI-induced damage. This is not unexpected, since the TC population I examined is anatomically connected to the injury and therefore more affected by it. The higher TC susceptibility is highlighted by the direct

comparison of TC and NTC spine densities across post-injury timepoints: While the two populations were very similar at proximal distances from soma, I noticed significant differences for the distal and apical tuft segments, with TC neurons displaying much lower spine density compared to NTC at 7dpi and 14dpi, respectively. Considering previous findings, there are only a few studies that-in agreement with my findings- reported contralateral spine loss after TBI but they observed it either in hippocampal neurons at 7dpi [282] or in layer II/III neurons just 24h post-injury. Moreover, none of these studies measured the spine density at longer post-injury timepoints to investigate potential spine recovery. Therefore, this is the first study to observe contralateral spine loss in neurons of layer V and specifically in TC neurons, a particular population of neurons anatomically connected via their axons to the injured area, appearing and resolving earlier at short distance from soma (7dpi-21dpi) and later at long distance from soma (14dpi-42dpi). This distance-related delay may indicate a retrogradely progressing deterioration, starting from the areas closest to the cell body, which takes about the same time to resolve. These results clearly show that the TC and NTC neuronal populations display a different response to TBI. My data argue for a direct sensing of the injury by the axons of TC neurons that, in response, induces changes on their dendrites such as spine loss followed by spine recovery. The fact that a small and non-significant loss of spines is also observed at 14dpi in NTC neurons at the proximal segment, which are not directly connected to the injury, also indicates a delayed and minored response that is potentially mediated by communication between the two populations. Thus, my results could argue that connected and non-connected neuronal populations experience a different effect of TBI in terms of magnitude and time-evolution. Importantly, the spine density of the connected population returns to normal levels by 42dpi.These plastic events could hence contribute to the functional recovery that can be seen following moderate brain injury.

I went on investigating whether the observed spine loss and subsequent spine recovery coincide with morphological rearrangements, such as reduction or prevalence of a certain type of spine over others. The morphology of a spine relates to different synaptic maturity and stability. It is generally accepted that mushroom-shaped spines are mostly seen in mature, stable synapses [283] while thin-shaped spines are quite mobile and are usually seen at newly formed, immature synapses [284]. Stubby-shaped spines are believed to either mirror the transitional state between a newly formed and a mature spine or to represent the retraction state of a mature spine that degrades [285].

My analysis revealed significant changes in spine morphology only in the apical tuft segment for both TC and NTC neuronal population. In the case of TC neurons, I observed a reduction in the percentage of mushroom spines at 2dpi to 14dpi compared to control, however the reduction at 7dpi was not statistically significant. Interestingly, at 14dpi the percentage of stubby spines was increased compared to control. Thus, at 14dpi, which is also the timepoint I noticed a drop in TC apical tuft-spine density, there is a loss of -normally stable- mushroom spines, together with gain of transition-state stubby spines compared to control, while newly formed thin spines seem to be unaffected. This is indicative of a general synaptic instability induced by the TBI, starting early after the injury with loss of mature synapses. Later on, the mature spines are still reduced but there is an increased number of spines at the transition state, most probably from maturity to elimination and this coincides with the point I first observed a spine density decrease.

Regarding NTC neurons, although I did not detect any significant reduction in spine density, there is a late and slight change in spine morphology at the apical tuft, with stubby spines being increased at 42dpi compared to control, and the percentage of thin spines being the lowest across the three types. This outcome further supports what the spine density results indicated: There is a delayed NTC response to TBI that could be mediated by communication with the directly connected to the injury TC population. The late NTC stubby spine increase could be interpreted as delayed mirroring of the spine destabilization taking place in TC neurons. However, it may also be a compensatory response, with NTC immature spines transitioning to a more mature and stable state. Considering that the two populations are integrated in common networks, it is possible that NTC neurons- being less affected by the injury compared to their TC neighbors- are able to provide some compensation for the initial TC spine destabilization.

My spine morphology results resemble previous research that found reduced mushroom spine density and increased stubby spine density after mild TBI [142]. However, the aforementioned study looked at spared neurons at the lesion area and not the intact contralateral cortex. Since there is a lack of TBI studies examining the contralateral to TBI cortex, I compare my results to stroke studies: According to an *in vivo* imaging stroke study [186] the turnover rate of mushroom-shaped spines of pyramidal neurons in the intact homologous cortex increased specifically at 7 days after stroke compared to control (with loss being slightly higher than gain). This finding is in line with my results, underscoring that the usually stable and mature mushroom spines are more de-stabilized after a remote focal lesion. However, these studies did not look at late post-injury timepoints to examine whether the mature spine loss persists while my data suggest that the mature spine loss is reversed by 42dpi. Nevertheless, using *in-vivo* two-photon

imaging to measure spine turnover for each spine type would be a more valid approach for making any inferences regarding contralateral synaptic plasticity but it was beyond the time limits of this study.

The most interesting finding of this part of my study is that after the aforementioned period of spine loss and de-stabilization there is significant spine recovery that is observable at 3-6 weeks post-injury. This was the case only for the anatomically connected to the injured cortex, TC population. The spine density of the NTC population did not only remain unaffected at early post-injury timepoints but also did not show any increase at later timepoints. Interestingly, for TC dendrites the smaller their distance from soma, the faster the spine recovery started. In addition to the late spine density recovery, the initial tendency for mature spine destabilization did not persist at later timepoints. This is another indication that adaptive events are taking place in long-term after TBI with TC neurons forming new connections or re-establishing previously lost connections.

To conclude, this is the first study to investigate the time-course of spine plasticity at the contralateral cortex in a population-based approach. No previous TBI research has compared the plastic abilities of a connected to the injury versus a non-connected to the injury neuronal population in a time-dependent manner. My findings do not only highlight that the two populations respond differently to the injury, but also suggest potential communication between them that could be adaptive. More importantly, the contralateral TC neurons exhibit a prominent ability for late recovery of their initial spine loss which suggests that the TC neuronal circuits might remodel and might lead to better functional outcomes chronically after injury. This underscores the existence of innate repair mechanisms, as it has been speculated before [130] [132] and these results motivated me to investigate the contralateral TC neuron circuitry after TBI, which constitutes the last part of my study.

4.3 Monosynaptic rabies virus tracing for reconstruction of transcallosal neuron circuitry to study remodeling after TBI: Re-establishment of original circuits following transient initial loss of connectivity

The detection of TC neuron-specific spine changes in spine density and morphology occurring between 1-2 weeks post-injury and recovering at 3-6 weeks post injury gave a strong indication that synaptic modifications take place in the anatomically connected neuronal population as a result of TBI. I therefore wanted to determine whether the change in synaptic density is mirrored by changes in circuit connectivity. In other terms, I wanted to clarify whether the spine loss and recovery over time translate in network integration changes of these transcallosal neurons. Thus, I aimed at investigating the first order presynaptic connections of TC neurons following TBI. I did so at two timepoints post-TBI: 1week post-injury (when I saw spine loss) and 6 weeks post injury (when the spine numbers recovered). For that purpose, I made use of the pseudotyped SAD-ΔG-mcherry (EnvA) Rabies virus, that enabled me to efficiently and specifically label the direct presynaptic partners of TC neurons, when complemented with G-protein expression. The successful implementation of this modified virus on monosynaptic tracing has been verified by several previous studies [244] [286] [287]. My question was not only how many presynaptic connections there are but also where they reside in the healthy and the injured brain, and whether they differ between the early versus the late timepoint post-injury, coinciding with the observed spine recovery. I expressed the results as connectivity ratio (number of presynaptic cells/ total number of starter cells) per brain region, after carefully defining distinct brain regions according to the Allen brain atlas (© 2011 Allen Institute for Brain Science. Allen Mouse Brain Reference Atlas. Available from: http://mouse.brain-map.org/static/atlas)

I observed that presynaptic cells are mainly found in the same brain regions in the healthy and injured brain. Areas containing the highest numbers of presynaptic connections were the somatosensory, motor, auditory, retrosplenial and parietal cortices, as well as the thalamus. Many areas that included presynaptic connections in the cortex contralateral to the rabies injection site in the control group were missing in the early TBI group as a result of the lesion. This is important to mention as it validates my approach and supports the logic behind looking at later timepoints for circuit remodeling.

Moreover, I found areas displaying a low number of presynaptic connections in the TBI-42d group but no connections in the TBI-7d group and vice versa. The 42d TBI group has

presynaptic connections in the claustrum and substantia innominata, upper layers of contralateral anterior cingulate cortex, lower layers of contralateral motor cortex and contralateral retrosplenial cortex that were not found in the 7d TBI mice (fig 42). This is indicative of compensatory remodeling. In addition, the 42d TBI group exhibited a very small number of presynaptic cells ectopically (not present in the healthy brain), in the upper visceral area of the cortex. Whether these are adaptive or maladaptive connection remains to be determined but their number remains relatively small. Although these findings suggest that connections with the aforementioned areas are lost at 7d post-TBI and re-established to some extent at 42d post-TBI, indicative of circuit plasticity, the connectivity ratios in those areas are very low. Therefore, it is essential to highlight that, if these low-scale changes I see between early and late post-injury timepoints reflect circuit remodeling, it is a very subtle process whose functional significance is yet unknown.

Furthermore, some of the areas with high numbers of presynaptic neurons displayed significantly different connectivity ratios after injury compared to control. Noticeably, there is a general significant de-connection between TC neurons and their presynaptic partners in the auditory cortex for both post-injury timepoints. The same stands for the upper layers of motor cortex but more prominently at 42d post-TBI. The upper and lower layers of the somatosensory cortex showed a quite differential response to TBI. I observed a significant de-connection between TC neurons and their presynaptic partners in the upper somatosensory layers at 7d post-TBI which was not just reversed at 42d post-TBI, but even more TC connections with this area formed. On the contrary, there was a late occurring de-connection of TC neurons with their presynaptic partners in the lower layers of the sensorimotor cortex. Such findings do not come as a surprise, since the somatosensory cortex is completely damaged by the injury, as is most of the auditory cortex and it is logical that their homologous areas at the intact cortex show more sensitivity to the effects of TBI. The observed reconnection of neurons in the upper somatosensory cortex with the TC population, which happens at the late post-injury timepoint, could underscore the functional significance of this area. Interestingly, the late establishment of even more connections in the upper somatosensory cortex shows that this area might be favored over the auditory, motor or lower somatosensory cortices, thus indicating a remodeling process of high specificity. In addition to the area-dependent analysis, I looked at possible changes in the distribution of the presynaptic cells along the rostro-caudal axis. I identified significantly higher percentage of presynaptic neurons residing in the two most caudal sections for the TBI-42d group and in the last most caudal section for the TBI-7d group compared to the control. Why caudal connections seem to be slightly favorable after TBI is an interesting

question that could be explained by the fact that the TBI-induced damage spreads rather caudally. A more rostral TBI paradigm could provide a possible answer to this question but such an experiment was beyond the time-limits of this study. It is crucial to highlight that, taken together, my data regarding spine loss followed by recovery and relative restoration of connection between transcallosal neurons and their presynaptic partners, indicate that following traumatic brain injury anatomically connected neurons recover by restoring or increasing their synaptic contacts with the initial population of presynaptic neurons rather than connecting with a different presynaptic population. This response is probably key to the restoration of adaptive functions and contributes to limiting maladaptive behavior.

Until today, limited studies have explored the effects of TBI on plasticity at the contralateral cortex, and they have done so by looking at contralateral dendritic spine/ synaptic response [140] [141]. This study is the first to investigate contralateral remodeling processes by means of neuronal circuit mapping. It is also the first study to accurately and quantitatively describe where TC neurons receive synaptic input from in the healthy brain as well as in the injured brain. These results demonstrate the presence of circuit adaptation that proceeds preferentially by re-establishing connections to the initial presynaptic population which might be of high importance for the maintenance of correct functional outcome.

Chapter 5: Conclusions

In summary, I can draw the following new conclusions from my thesis:

Most of the transcallosal projections show a rigorous homotopic organization across different regions of the cortex, with the cell bodies of these neurons being mainly located in layer II/III and layer V but also in smaller numbers in layer IV and layer VI. I have discovered that however, there is a small but considerable amount of transcallosal neuron connections that are heterotopic. Interestingly, the transcallosal neurons found heterotopically, especially in the lateral adjacent area, show less rigid layer distribution compared to the homotopic ones. I believe that I provide here a systematic characterization of transcallosal connections across distinct cortical regions that might set the foundation for future research into the potentially different functions of homotopic versus heterotopic transcallosal neurons in health and disease. Furthermore, the findings underscore that other studies should be careful when making assumptions about transcallosal connectivity among different cortical areas as I have described for the first time some previously under-reported heterogeneity.

TBI Induces important changes in the contralateral hemisphere. While I demonstrated that the gross contralateral cytoarchitecture and layering was not affected by a mild TBI, I observed new and important reductions in the dendritic spine density of transcallosal neurons. Dendritic segments closer to the soma (proximal) lose spines 1 week after the injury and regain them by 3 weeks post-TBI while dendritic segments with the highest distance from soma (apical tuft) lose spines 2 weeks after injury and regain them by 6 weeks post-TBI. Interestingly, I could also demonstrate a shift in spine morphology after TBI in particular in the apical tuft segments. Here again I could demonstrate that TC neurons show a reduction in mushroom-shaped spines together with an increase in stubby-shaped spines at the 2-week timepoint, coinciding with the general spine loss, indicative of a de-stabilization of mature synapses. Most surprisingly I also show that this spine shape change is then resolved at later timepoints following the injury. Therefore, my findings suggest plasticity-related changes that might suggest a change in general contralateral neuronal connectivity.

In the third part of the study, I have demonstrated that the spine plasticity does not result in circuit remodeling in the contralateral hemisphere. Rather than recruiting new synaptic partners as a result of the spine remodeling, I observed that transcallosal neurons re- establish similar

circuitry forming contacts with presynaptic cells in similar locations as in control animals. I therefore did not detect the establishment of new circuits. This might indicate a strengthening and re-establishment of original circuits following the transient initial deconstruction of connectivity after the injury and might be a sign of adaptive plasticity that could yield functional recovery.

Bibliography

1. McKee, A.C. and D.H. Daneshvar, *The neuropathology of traumatic brain injury.* Handb Clin Neurol, 2015. **127**: p. 45-66.
2. van Middendorp, J.J., G.M. Sanchez, and A.L. Burridge, *The Edwin Smith papyrus: a clinical reappraisal of the oldest known document on spinal injuries.* Eur Spine J, 2010. **19**(11): p. 1815-23.
3. Panourias, I.G., et al., *Hippocrates: a pioneer in the treatment of head injuries.* Neurosurgery, 2005. **57**(1): p. 181-9; discussion 181-9.
4. Kshettry, V.R., S.A. Mindea, and H.H. Batjer, *The management of cranial injuries in antiquity and beyond.* Neurosurg Focus, 2007. **23**(1): p. E8.
5. Levin H.S., B.A.L., Grossman R. , *''Historical review of head injury''. Neurobehavioral Consequences of Closed Head Injury*. Oxford University Press. 1982. 3–5.
6. Echemendia, R.J., *Assessment and Management of Concussion: A Neuropsychological Perspective*, in *Foundations of Sport-Related Brain Injuries*, S. Slobounov and W. Sebastianelli, Editors. 2006, Springer US: Boston, MA. p. 431-443.
7. Granacher, R.A., *Traumatic Brain Injury: Methods for Clinical and Forensic Neuropsychiatric Assessment*. Second ed. 2007, Boca Raton: CRC.
8. Johnson, W.D. and D.P. Griswold, *Traumatic brain injury: a global challenge.* Lancet Neurol, 2017. **16**(12): p. 949-950.
9. Hyder, A.A., et al., *The impact of traumatic brain injuries: a global perspective.* NeuroRehabilitation, 2007. **22**(5): p. 341-53.
10. Frost, R.B., et al., *Prevalence of traumatic brain injury in the general adult population: a meta-analysis.* Neuroepidemiology, 2013. **40**(3): p. 154-9.
11. Wirth, A., et al., *Prospective documentation and analysis of the pre- and early clinical management in severe head injury in southern Bavaria at a population based level.* Acta Neurochir Suppl, 2004. **89**: p. 119-23.
12. Taylor, C.A., et al., *Traumatic Brain Injury-Related Emergency Department Visits, Hospitalizations, and Deaths - United States, 2007 and 2013.* MMWR Surveill Summ, 2017. **66**(9): p. 1-16.
13. Majdan, M., et al., *Epidemiology of traumatic brain injuries in Europe: a cross-sectional analysis.* Lancet Public Health, 2016. **1**(2): p. e76-e83.
14. Polinder, S., et al., *Cost estimation of injury-related hospital admissions in 10 European countries.* J Trauma, 2005. **59**(6): p. 1283-90; discussion 1290-1.
15. Polinder, S., et al., *Assessing the burden of injury in six European countries.* Bull World Health Organ, 2007. **85**(1): p. 27-34.
16. Li, Y., et al., *Head Injury as a Risk Factor for Dementia and Alzheimer's Disease: A Systematic Review and Meta-Analysis of 32 Observational Studies.* PLoS One, 2017. **12**(1): p. e0169650.
17. Nemetz, P.N., et al., *Traumatic brain injury and time to onset of Alzheimer's disease: a population-based study.* Am J Epidemiol, 1999. **149**(1): p. 32-40.
18. Schaffert, J., et al., *Traumatic brain injury history is associated with an earlier age of dementia onset in autopsy-confirmed Alzheimer's disease.* Neuropsychology, 2018. **32**(4): p. 410-416.
19. Rugbjerg, K., et al., *Risk of Parkinson's disease after hospital contact for head injury: population based case-control study.* BMJ, 2008. **337**: p. a2494.
20. Fedoroff, J.P., et al., *Depression in patients with acute traumatic brain injury.* Am J Psychiatry, 1992. **149**(7): p. 918-23.

21.   Jorge, R.E., et al., *Major depression following traumatic brain injury.* Arch Gen Psychiatry, 2004. **61**(1): p. 42-50.

22.   Kim, E., et al., *Neuropsychiatric complications of traumatic brain injury: a critical review of the literature (a report by the ANPA Committee on Research).* J Neuropsychiatry Clin Neurosci, 2007. **19**(2): p. 106-27.

23.   Rogers, J.M. and C.A. Read, *Psychiatric comorbidity following traumatic brain injury.* Brain Inj, 2007. **21**(13-14): p. 1321-33.

24.   Schwarzbold, M., et al., *Psychiatric disorders and traumatic brain injury.* Neuropsychiatr Dis Treat, 2008. **4**(4): p. 797-816.

25.   Zink, B.J., *Traumatic brain injury outcome: concepts for emergency care.* Ann Emerg Med, 2001. **37**(3): p. 318-32.

26.   Cassidy, J.D., et al., *Incidence, risk factors and prevention of mild traumatic brain injury: results of the WHO Collaborating Centre Task Force on Mild Traumatic Brain Injury.* J Rehabil Med, 2004(43 Suppl): p. 28-60.

27.   Narayan, R.K., et al., *Clinical trials in head injury.* J Neurotrauma, 2002. **19**(5): p. 503-57.

28.   Teasdale, S.G. 1974; Available from: www.universitystory.gla.ac.uk/biography/?id=WH1855&type=P.

29.   Saatman, K.E., et al., *Classification of traumatic brain injury for targeted therapies.* J Neurotrauma, 2008. **25**(7): p. 719-38.

30.   Drake, A.I., et al., *Utility of Glasgow Coma Scale-Extended in symptom prediction following mild traumatic brain injury.* Brain Inj, 2006. **20**(5): p. 469-75.

31.   McCullagh, S., et al., *Prediction of neuropsychiatric outcome following mild trauma brain injury: an examination of the Glasgow Coma Scale.* Brain Inj, 2001. **15**(6): p. 489-97.

32.   National Academy of Engineering (US); Institute of Medicine (US); Butler D, B.J., Erdtmann F, et al., editors. Systems Engineering to Improve Traumatic Brain Injury Care in the Military Health System: Workshop Summary. Washington (DC): National Academies Press (US); 2009. 3, Traumatic Brain Injury and the Military Health System. Available from: https://www.ncbi.nlm.nih.gov/books/NBK214914/.

33.   Andriessen, T.M., B. Jacobs, and P.E. Vos, *Clinical characteristics and pathophysiological mechanisms of focal and diffuse traumatic brain injury.* J Cell Mol Med, 2010. **14**(10): p. 2381-92.

34.   Gennarelli, T.A., et al., *Diffuse axonal injury and traumatic coma in the primate.* Ann Neurol, 1982. **12**(6): p. 564-74.

35.   Pudenz, R.H. and C.H. Shelden, *The lucite calvarium; a method for direct observation of the brain; cranial trauma and brain movement.* J Neurosurg, 1946. **3**(6): p. 487-505.

36.   LaPlaca, M.C., et al., *CNS injury biomechanics and experimental models.* Prog Brain Res, 2007. **161**: p. 13-26.

37.   Gennarelli, T.A., *Mechanisms of brain injury.* J Emerg Med, 1993. **11 Suppl 1**: p. 5-11.

38.   Skandsen, T., et al., *Prevalence and impact of diffuse axonal injury in patients with moderate and severe head injury: a cohort study of early magnetic resonance imaging findings and 1-year outcome.* J Neurosurg, 2010. **113**(3): p. 556-63.

39.   Graham, D.I., et al., *Quantification of primary and secondary lesions in severe head injury.* Acta Neurochir Suppl (Wien), 1993. **57**: p. 41-8.

40.   Inoue, Y., et al., *Changes in cerebral blood flow from the acute to the chronic phase of severe head injury.* J Neurotrauma, 2005. **22**(12): p. 1411-8.

41.   Overgaard, J. and W.A. Tweed, *Cerebral circulation after head injury. Part 4: Functional anatomy and boundary-zone flow deprivation in the first week of traumatic coma.* J Neurosurg, 1983. **59**(3): p. 439-46.

42.   Johnston, A.J., et al., *Effect of cerebral perfusion pressure augmentation on regional oxygenation and metabolism after head injury.* Crit Care Med, 2005. **33**(1): p. 189-95; discussion 255-7.

43.   Rose, J.C., T.A. Neill, and J.C. Hemphill, 3rd, *Continuous monitoring of the microcirculation in neurocritical care: an update on brain tissue oxygenation.* Curr Opin Crit Care, 2006. **12**(2): p. 97-102.

44.   Stiefel, M.F., Y. Tomita, and A. Marmarou, *Secondary ischemia impairing the restoration of ion homeostasis following traumatic brain injury.* J Neurosurg, 2005. **103**(4): p. 707-14.

45.   Verweij, B.H., et al., *Impaired cerebral mitochondrial function after traumatic brain injury in humans.* J Neurosurg, 2000. **93**(5): p. 815-20.

46.   Bullock, R., et al., *Factors affecting excitatory amino acid release following severe human head injury.* J Neurosurg, 1998. **89**(4): p. 507-18.

47.   Dong, X.X., Y. Wang, and Z.H. Qin, *Molecular mechanisms of excitotoxicity and their relevance to pathogenesis of neurodegenerative diseases.* Acta Pharmacol Sin, 2009. **30**(4): p. 379-87.

48.   Floyd, C.L., F.A. Gorin, and B.G. Lyeth, *Mechanical strain injury increases intracellular sodium and reverses Na+/Ca2+ exchange in cortical astrocytes.* Glia, 2005. **51**(1): p. 35-46.

49.   Pant, H.C., et al., *Distribution of calcium-activated protease activity and endogenous substrates in the squid nervous system.* J Neurosci, 1982. **2**(11): p. 1578-87.

50.   Velasco M., R.-Q.J., Chávez-Castillo M., Rojas M., Bautista J.   , *Excitotoxicity: An Organized Crime at The Cellular Level.* J Neurol Neurosci. , 2017. **8**(3): p. 193.

51.   Tepperman, B.L., C.W. Lush, and B.D. Soper, *Role of endonuclease activity and DNA fragmentation in Ca2+ ionophore A23187-mediated injury to rabbit isolated gastric mucosal cells.* Dig Dis Sci, 1996. **41**(6): p. 1172-80.

52.   Ong, W.Y., et al., *Slow excitotoxicity in Alzheimer's disease.* J Alzheimers Dis, 2013. **35**(4): p. 643-68.

53.   Melloni, E. and S. Pontremoli, *The calpains.* Trends Neurosci, 1989. **12**(11): p. 438-44.

54.   Gagliardi, R.J., *Neuroprotection, excitotoxicity and NMDA antagonists.* Arq Neuropsiquiatr, 2000. **58**(2B): p. 583-8.

55.   Duchen, M.R., *Roles of mitochondria in health and disease.* Diabetes, 2004. **53 Suppl 1**: p. S96-102.

56.   Bhat, A.H., et al., *Oxidative stress, mitochondrial dysfunction and neurodegenerative diseases; a mechanistic insight.* Biomed Pharmacother, 2015. **74**: p. 101-10.

57.   Guo, Y., et al., *Caspase-2 induces apoptosis by releasing proapoptotic proteins from mitochondria.* J Biol Chem, 2002. **277**(16): p. 13430-7.

58.   Uzan, M., et al., *Evaluation of apoptosis in cerebrospinal fluid of patients with severe head injury.* Acta Neurochir (Wien), 2006. **148**(11): p. 1157-64; discussion.

59.   Strich, S.J., *Shearing of nerve fibres as a cause of brain damage due to head injury: a pathological study of twenty cases.* The Lancet 1961. **278**(7200): p. 443 - 448.

60.   Green, R.E., et al., *Scale and pattern of atrophy in the chronic stages of moderate-severe TBI.* Front Hum Neurosci, 2014. **8**: p. 67.

61.   Adams, J.H., et al., *Diffuse axonal injury in head injury: definition, diagnosis and grading.* Histopathology, 1989. **15**(1): p. 49-59.

62.   Margulies, S.S. and L.E. Thibault, *A proposed tolerance criterion for diffuse axonal injury in man.* J Biomech, 1992. **25**(8): p. 917-23.

63.   Povlishock, J.T. and C.W. Christman, *The pathobiology of traumatically induced axonal injury in animals and humans: a review of current thoughts.* J Neurotrauma, 1995. **12**(4): p. 555-64.

64.   Povlishock, J.T. and E.H. Pettus, *Traumatically induced axonal damage: evidence for enduring changes in axolemmal permeability with associated cytoskeletal change.* Acta Neurochir Suppl, 1996. **66**: p. 81-6.

65.   Buki, A., et al., *The role of calpain-mediated spectrin proteolysis in traumatically induced axonal injury.* J Neuropathol Exp Neurol, 1999. **58**(4): p. 365-75.

66.   Povlishock, J.T., *Traumatically induced axonal injury: pathogenesis and pathobiological implications.* Brain Pathol, 1992. **2**(1): p. 1-12.

67.   Nikic, I., et al., *A reversible form of axon damage in experimental autoimmune encephalomyelitis and multiple sclerosis.* Nat Med, 2011. **17**(4): p. 495-9.

68.   Christman, C.W., et al., *Ultrastructural studies of diffuse axonal injury in humans.* J Neurotrauma, 1994. **11**(2): p. 173-86.

69.   Reeves, T.M., L.L. Phillips, and J.T. Povlishock, *Myelinated and unmyelinated axons of the corpus callosum differ in vulnerability and functional recovery following traumatic brain injury.* Exp Neurol, 2005. **196**(1): p. 126-37.

70.   Reeves, T.M., et al., *Unmyelinated axons show selective rostrocaudal pathology in the corpus callosum after traumatic brain injury.* J Neuropathol Exp Neurol, 2012. **71**(3): p. 198-210.

71.   Greer, J.E., et al., *Mild traumatic brain injury in the mouse induces axotomy primarily within the axon initial segment.* Acta Neuropathol, 2013. **126**(1): p. 59-74.

72.   Greer, J.E., M.J. McGinn, and J.T. Povlishock, *Diffuse traumatic axonal injury in the mouse induces atrophy, c-Jun activation, and axonal outgrowth in the axotomized neuronal population.* J Neurosci, 2011. **31**(13): p. 5089-105.

73.   Wang, G., et al., *Microglia/macrophage polarization dynamics in white matter after traumatic brain injury.* J Cereb Blood Flow Metab, 2013. **33**(12): p. 1864-74.

74.   Morganti-Kossmann, M.C., et al., *Role of cerebral inflammation after traumatic brain injury: a revisited concept.* Shock, 2001. **16**(3): p. 165-77.

75.   Riva-Depaty, I., et al., *Contribution of peripheral macrophages and microglia to the cellular reaction after mechanical or neurotoxin-induced lesions of the rat brain.* Exp Neurol, 1994. **128**(1): p. 77-87.

76.   Chiu, C.C., et al., *Neuroinflammation in animal models of traumatic brain injury.* J Neurosci Methods, 2016. **272**: p. 38-49.

77.   Velazquez, A., et al., *Widespread microglial activation in patients deceased from traumatic brain injury.* Brain Inj, 2015. **29**(9): p. 1126-33.

78.   Fu, R., et al., *Phagocytosis of microglia in the central nervous system diseases.* Mol Neurobiol, 2014. **49**(3): p. 1422-34.

79.   Kigerl, K.A., et al., *Identification of two distinct macrophage subsets with divergent effects causing either neurotoxicity or regeneration in the injured mouse spinal cord.* J Neurosci, 2009. **29**(43): p. 13435-44.

80.   Kumar, A., et al., *Traumatic brain injury in aged animals increases lesion size and chronically alters microglial/macrophage classical and alternative activation states.* Neurobiol Aging, 2013. **34**(5): p. 1397-411.

81.   Loane, D.J., et al., *Progressive neurodegeneration after experimental brain trauma: association with chronic microglial activation.* J Neuropathol Exp Neurol, 2014. **73**(1): p. 14-29.

82.   Brooks, W.M., et al., *Metabolic and cognitive response to human traumatic brain injury: a quantitative proton magnetic resonance study.* J Neurotrauma, 2000. **17**(8): p. 629-40.

83.   Taupin, V., et al., *Increase in IL-6, IL-1 and TNF levels in rat brain following traumatic lesion. Influence of pre- and post-traumatic treatment with Ro5 4864, a peripheral-type (p site) benzodiazepine ligand.* J Neuroimmunol, 1993. **42**(2): p. 177-85.

84.   Holmin, S. and B. Hojeberg, *In situ detection of intracerebral cytokine expression after human brain contusion.* Neurosci Lett, 2004. **369**(2): p. 108-14.

85.   Rothwell, N.J., *Annual review prize lecture cytokines - killers in the brain?* J Physiol, 1999. **514 (Pt 1)**: p. 3-17.

86.   Clausen, F., et al., *Neutralization of interleukin-1beta reduces cerebral edema and tissue loss and improves late cognitive outcome following traumatic brain injury in mice.* Eur J Neurosci, 2011. **34**(1): p. 110-23.

87.   Penkowa, M., et al., *Impaired inflammatory response and increased oxidative stress and neurodegeneration after brain injury in interleukin-6-deficient mice.* Glia, 2000. **32**(3): p. 271-85.

88.   Penkowa, M., et al., *Astrocyte-targeted expression of interleukin-6 protects the central nervous system during neuroglial degeneration induced by 6-aminonicotinamide.* J Neurosci Res, 2003. **73**(4): p. 481-96.

89.   Ziebell, J.M. and M.C. Morganti-Kossmann, *Involvement of pro- and anti-inflammatory cytokines and chemokines in the pathophysiology of traumatic brain injury.* Neurotherapeutics, 2010. **7**(1): p. 22-30.

90.   Whalen, M.J., et al., *Interleukin-8 is increased in cerebrospinal fluid of children with severe head injury.* Crit Care Med, 2000. **28**(4): p. 929-34.

91.   Bellander, B.M., et al., *Complement activation in the human brain after traumatic head injury.* J Neurotrauma, 2001. **18**(12): p. 1295-311.

92.   van Beek, J., K. Elward, and P. Gasque, *Activation of complement in the central nervous system: roles in neurodegeneration and neuroprotection.* Ann N Y Acad Sci, 2003. **992**: p. 56-71.

93.   Schmidt, O.I., et al., *Closed head injury--an inflammatory disease?* Brain Res Brain Res Rev, 2005. **48**(2): p. 388-99.

94.   Alawieh, A., et al., *Identifying the role of complement in triggering neuroinflammation after traumatic brain injury.* J Neurosci, 2018.

95.   Bellander, B.M., et al., *Secondary insults following traumatic brain injury enhance complement activation in the human brain and release of the tissue damage marker S100B.* Acta Neurochir (Wien), 2011. **153**(1): p. 90-100.

96.   Nathoo, N., et al., *Influence of apoptosis on neurological outcome following traumatic cerebral contusion.* J Neurosurg, 2004. **101**(2): p. 233-40.

97.   Borgens, R.B. and P. Liu-Snyder, *Understanding secondary injury.* Q Rev Biol, 2012. **87**(2): p. 89-127.

98.   Ling, G.S., S.A. Marshall, and D.F. Moore, *Diagnosis and management of traumatic brain injury.* Continuum (Minneap Minn), 2010. **16**(6 Traumatic Brain Injury): p. 27-40.

99.   Levin, H.S. and R.R. Diaz-Arrastia, *Diagnosis, prognosis, and clinical management of mild traumatic brain injury.* Lancet Neurol, 2015. **14**(5): p. 506-17.

100.   Carron, S.F., D.S. Alwis, and R. Rajan, *Traumatic Brain Injury and Neuronal Functionality Changes in Sensory Cortex.* Front Syst Neurosci, 2016. **10**: p. 47.

101.   Wright, D.W., et al., *Very early administration of progesterone for acute traumatic brain injury.* N Engl J Med, 2014. **371**(26): p. 2457-66.

102.   Williams, A.J., et al., *Characterization of a new rat model of penetrating ballistic brain injury.* J Neurotrauma, 2005. **22**(2): p. 313-31.

103.   Nilsson, B., U. Ponten, and G. Voigt, *Experimental head injury in the rat. Part 1: Mechanics, pathophysiology, and morphology in an impact acceleration trauma model.* J Neurosurg, 1977. **47**(2): p. 241-51.

104.   Alder, J., et al., *Lateral fluid percussion: model of traumatic brain injury in mice.* J Vis Exp, 2011(54).

105.   Marmarou, A., et al., *A new model of diffuse brain injury in rats. Part I: Pathophysiology and biomechanics.* J Neurosurg, 1994. **80**(2): p. 291-300.

106.   White, C.S., I.G. Bowen, and D.R. Richmond, *Biological tolerance to air blast and related biomedical criteria. CEX-65.4.* CEX Rep Civ Eff Exerc, 1965: p. 1-239.

107. Risling, M., et al., *Mechanisms of blast induced brain injuries, experimental studies in rats.* Neuroimage, 2011. **54 Suppl 1**: p. S89-97.
108. Long, J.B., et al., *Blast overpressure in rats: recreating a battlefield injury in the laboratory.* J Neurotrauma, 2009. **26**(6): p. 827-40.
109. Namjoshi, D.R., et al., *Merging pathology with biomechanics using CHIMERA (Closed-Head Impact Model of Engineered Rotational Acceleration): a novel, surgery-free model of traumatic brain injury.* Mol Neurodegener, 2014. **9**: p. 55.
110. Albert-Weissenberger, C. and A.L. Siren, *Experimental traumatic brain injury.* Exp Transl Stroke Med, 2010. **2**(1): p. 16.
111. Alessandri, B., et al., *Caspase-dependent cell death involved in brain damage after acute subdural hematoma in rats.* Brain Res, 2006. **1111**(1): p. 196-202.
112. Manley, G.T., et al., *Controlled cortical impact in swine: pathophysiology and biomechanics.* J Neurotrauma, 2006. **23**(2): p. 128-39.
113. Alessandri, B., et al., *Moderate controlled cortical contusion in pigs: effects on multi-parametric neuromonitoring and clinical relevance.* J Neurotrauma, 2003. **20**(12): p. 1293-305.
114. Smith, D.H., et al., *A model of parasagittal controlled cortical impact in the mouse: cognitive and histopathologic effects.* J Neurotrauma, 1995. **12**(2): p. 169-78.
115. Dixon, C.E., et al., *A controlled cortical impact model of traumatic brain injury in the rat.* J Neurosci Methods, 1991. **39**(3): p. 253-62.
116. Lighthall, J.W., *Controlled cortical impact: a new experimental brain injury model.* J Neurotrauma, 1988. **5**(1): p. 1-15.
117. Lighthall, J.W., H.G. Goshgarian, and C.R. Pinderski, *Characterization of axonal injury produced by controlled cortical impact.* J Neurotrauma, 1990. **7**(2): p. 65-76.
118. Hall, E.D., et al., *Evolution of post-traumatic neurodegeneration after controlled cortical impact traumatic brain injury in mice and rats as assessed by the de Olmos silver and fluorojade staining methods.* J Neurotrauma, 2008. **25**(3): p. 235-47.
119. Lighthall, J.W., C.E. Dixon, and T.E. Anderson, *Experimental models of brain injury.* J Neurotrauma, 1989. **6**(2): p. 83-97.
120. Saatman, K.E., et al., *Differential behavioral and histopathological responses to graded cortical impact injury in mice.* J Neurotrauma, 2006. **23**(8): p. 1241-53.
121. Washington, P.M., et al., *The effect of injury severity on behavior: a phenotypic study of cognitive and emotional deficits after mild, moderate, and severe controlled cortical impact injury in mice.* J Neurotrauma, 2012. **29**(13): p. 2283-96.
122. Fox, G.B., et al., *Sustained sensory/motor and cognitive deficits with neuronal apoptosis following controlled cortical impact brain injury in the mouse.* J Neurotrauma, 1998. **15**(8): p. 599-614.
123. Dixon, C.E., et al., *Amantadine improves water maze performance without affecting motor behavior following traumatic brain injury in rats.* Restor Neurol Neurosci, 1999. **14**(4): p. 285-294.
124. Dixon, C.E., et al., *One-year study of spatial memory performance, brain morphology, and cholinergic markers after moderate controlled cortical impact in rats.* J Neurotrauma, 1999. **16**(2): p. 109-22.
125. Kochanek, P.M., et al., *Cerebral blood flow at one year after controlled cortical impact in rats: assessment by magnetic resonance imaging.* J Neurotrauma, 2002. **19**(9): p. 1029-37.
126. Liu, N.K., et al., *A bilateral head injury that shows graded brain damage and behavioral deficits in adultmice.* Brain Res, 2013. **1499**: p. 121-8.
127. Zhang, Y.P., et al., *Traumatic brain injury using mouse models.* Transl Stroke Res, 2014. **5**(4): p. 454-71.

128. Bolton Hall, A.N., et al., *Repeated Closed Head Injury in Mice Results in Sustained Motor and Memory Deficits and Chronic Cellular Changes.* PLoS One, 2016. **11**(7): p. e0159442.

129. Haaland, K.Y., et al., *Recovery of simple motor skills after head injury.* J Clin Exp Neuropsychol, 1994. **16**(3): p. 448-56.

130. Stahnisch, F.W. and R. Nitsch, *Santiago Ramon y Cajal's concept of neuronal plasticity: the ambiguity lives on.* Trends Neurosci, 2002. **25**(11): p. 589-91.

131. Liao, C.C., et al., *Stroke risk and outcomes in patients with traumatic brain injury: 2 nationwide studies.* Mayo Clin Proc, 2014. **89**(2): p. 163-72.

132. Meyer, J.S., Hata, T., Imai, A., *Clinical and experimental studies of diaschisis*, in *Cerebral Blood Flow: Physiologic and Clinical Aspects. .* 1987, McGraw-Hill Book Co: New York. p. 481-502.

133. Andrews, R.J., *Transhemispheric diaschisis. A review and comment.* Stroke, 1991. **22**(7): p. 943-9.

134. Finger, S., *Chapter 51: recovery of function: redundancy and vicariation theories.* Handb Clin Neurol, 2010. **95**: p. 833-41.

135. Stein, D.G., *Concepts of CNS plasticity and their implications or recovery after brain damage*, in *Brain Injury Med Principles and Practice.* 2013, Zasler ed. p. 162-174.

136. Yaghmai, A. and J. Povlishock, *Traumatically induced reactive change as visualized through the use of monoclonal antibodies targeted to neurofilament subunits.* J Neuropathol Exp Neurol, 1992. **51**(2): p. 158-76.

137. Hayes, R.L., et al., *Cytoskeletal derangements following central nervous system injury: modulation by neurotrophic gene transfection.* J Neurotrauma, 1995. **12**(5): p. 933-41.

138. Chen, S., J.D. Pickard, and N.G. Harris, *Time course of cellular pathology after controlled cortical impact injury.* Exp Neurol, 2003. **182**(1): p. 87-102.

139. Zhao, J., et al., *Mild Traumatic Brain Injury Reduces Spine Density of Projection Neurons in the Medial Prefrontal Cortex and Impairs Extinction of Contextual Fear Memory.* J Neurotrauma, 2018. **35**(1): p. 149-156.

140. Winston, C.N., et al., *Controlled cortical impact results in an extensive loss of dendritic spines that is not mediated by injury-induced amyloid-beta accumulation.* J Neurotrauma, 2013. **30**(23): p. 1966-72.

141. Campbell, J.N., et al., *Mechanisms of dendritic spine remodeling in a rat model of traumatic brain injury.* J Neurotrauma, 2012. **29**(2): p. 218-34.

142. Gao, X., et al., *Moderate traumatic brain injury causes acute dendritic and synaptic degeneration in the hippocampal dentate gyrus.* PLoS One, 2011. **6**(9): p. e24566.

143. Campbell, J.N., D. Register, and S.B. Churn, *Traumatic brain injury causes an FK506-sensitive loss and an overgrowth of dendritic spines in rat forebrain.* J Neurotrauma, 2012. **29**(2): p. 201-17.

144. Ding, M.C., et al., *Cortical excitation and inhibition following focal traumatic brain injury.* J Neurosci, 2011. **31**(40): p. 14085-94.

145. Johnstone, V.P., et al., *The acute phase of mild traumatic brain injury is characterized by a distance-dependent neuronal hypoactivity.* J Neurotrauma, 2014. **31**(22): p. 1881-95.

146. Alwis, D.S., et al., *Sensory cortex underpinnings of traumatic brain injury deficits.* PLoS One, 2012. **7**(12): p. e52169.

147. Johnstone, V.P., et al., *Cortical hypoexcitation defines neuronal responses in the immediate aftermath of traumatic brain injury.* PLoS One, 2013. **8**(5): p. e63454.

148. Yang, L., et al., *Spontaneous epileptiform activity in rat neocortex after controlled cortical impact injury.* J Neurotrauma, 2010. **27**(8): p. 1541-8.

149. Hofmeijer, J. and M.J. van Putten, *Ischemic cerebral damage: an appraisal of synaptic failure.* Stroke, 2012. **43**(2): p. 607-15.

150. Pei, L., et al., *A Novel Mechanism of Spine Damages in Stroke via DAPK1 and Tau.* Cereb Cortex, 2015. **25**(11): p. 4559-71.

151. Que, M., et al., *Widespread up-regulation of N-methyl-D-aspartate receptors after focal photothrombotic lesion in rat brain.* Neurosci Lett, 1999. **273**(2): p. 77-80.

152. Neumann-Haefelin, T., G. Hagemann, and O.W. Witte, *Cellular correlates of neuronal hyperexcitability in the vicinity of photochemically induced cortical infarcts in rats in vitro.* Neurosci Lett, 1995. **193**(2): p. 101-4.

153. Schiene, K., et al., *Neuronal hyperexcitability and reduction of GABAA-receptor expression in the surround of cerebral photothrombosis.* J Cereb Blood Flow Metab, 1996. **16**(5): p. 906-14.

154. Domann, R., et al., *Electrophysiological changes in the surrounding brain tissue of photochemically induced cortical infarcts in the rat.* Neurosci Lett, 1993. **155**(1): p. 69-72.

155. Schmidt, S., et al., *Age dependence of excitatory-inhibitory balance following stroke.* Neurobiol Aging, 2012. **33**(7): p. 1356-63.

156. Luhmann, H.J., *Ischemia and lesion induced imbalances in cortical function.* Prog Neurobiol, 1996. **48**(2): p. 131-66.

157. Logue, O.C., et al., *Alterations of functional properties of hippocampal networks following repetitive closed-head injury.* Exp Neurol, 2016. **277**: p. 227-243.

158. Tran, L.D., et al., *Response of the contralateral hippocampus to lateral fluid percussion brain injury.* J Neurotrauma, 2006. **23**(9): p. 1330-42.

159. Xerri, C., et al., *Interplay between intra- and interhemispheric remodeling of neural networks as a substrate of functional recovery after stroke: adaptive versus maladaptive reorganization.* Neuroscience, 2014. **283**: p. 178-201.

160. Nilsson, P., et al., *Epileptic seizure activity in the acute phase following cortical impact trauma in rat.* Brain Res, 1994. **637**(1-2): p. 227-32.

161. Roukoz B. Chamoun, S.P.G.a.C.S.R., *Cerebral Metabolism in the Management of TBI Patients.* The Open Neurosurgery Journal, 2010: p. 3-5.

162. Langfitt, T.W., et al., *Computerized tomography, magnetic resonance imaging, and positron emission tomography in the study of brain trauma. Preliminary observations.* J Neurosurg, 1986. **64**(5): p. 760-7.

163. Cantu, D., et al., *Traumatic Brain Injury Increases Cortical Glutamate Network Activity by Compromising GABAergic Control.* Cereb Cortex, 2015. **25**(8): p. 2306-20.

164. Carmichael, S.T., *Plasticity of cortical projections after stroke.* Neuroscientist, 2003. **9**(1): p. 64-75.

165. Carmichael, S.T., et al., *New patterns of intracortical projections after focal cortical stroke.* Neurobiol Dis, 2001. **8**(5): p. 910-22.

166. Christman, C.W., et al., *Characterization of a prolonged regenerative attempt by diffusely injured axons following traumatic brain injury in adult cat: a light and electron microscopic immunocytochemical study.* Acta Neuropathol, 1997. **94**(4): p. 329-37.

167. Emery, D.L., et al., *Bilateral growth-related protein expression suggests a transient increase in regenerative potential following brain trauma.* J Comp Neurol, 2000. **424**(3): p. 521-31.

168. Harris, N.G., et al., *Pericontusion axon sprouting is spatially and temporally consistent with a growth-permissive environment after traumatic brain injury.* J Neuropathol Exp Neurol, 2010. **69**(2): p. 139-54.

169. Jorgensen, O.S., et al., *Synaptic remodeling and free radical formation after brain contusion injury in the rat.* Exp Neurol, 1997. **144**(2): p. 326-38.

170. Kim, H.J., et al., *Elevation of hippocampal MMP-3 expression and activity during trauma-induced synaptogenesis.* Exp Neurol, 2005. **192**(1): p. 60-72.

171. Phillips, L.L. and T.M. Reeves, *Interactive pathology following traumatic brain injury modifies hippocampal plasticity.* Restor Neurol Neurosci, 2001. **19**(3-4): p. 213-35.

172.	Brown, C.E., et al., *Extensive turnover of dendritic spines and vascular remodeling in cortical tissues recovering from stroke.* J Neurosci, 2007. **27**(15): p. 4101-9.

173.	Brown, C.E., et al., *In vivo voltage-sensitive dye imaging in adult mice reveals that somatosensory maps lost to stroke are replaced over weeks by new structural and functional circuits with prolonged modes of activation within both the peri-infarct zone and distant sites.* J Neurosci, 2009. **29**(6): p. 1719-34.

174.	Brown, C.E., J.D. Boyd, and T.H. Murphy, *Longitudinal in vivo imaging reveals balanced and branch-specific remodeling of mature cortical pyramidal dendritic arbors after stroke.* J Cereb Blood Flow Metab, 2010. **30**(4): p. 783-91.

175.	Schaechter, J.D., et al., *Structural and functional plasticity in the somatosensory cortex of chronic stroke patients.* Brain, 2006. **129**(Pt 10): p. 2722-33.

176.	Xerri, C., et al., *Plasticity of primary somatosensory cortex paralleling sensorimotor skill recovery from stroke in adult monkeys.* J Neurophysiol, 1998. **79**(4): p. 2119-48.

177.	Dijkhuizen, R.M., et al., *Functional magnetic resonance imaging of reorganization in rat brain after stroke.* Proc Natl Acad Sci U S A, 2001. **98**(22): p. 12766-71.

178.	Gharbawie, O.A., et al., *Middle cerebral artery (MCA) stroke produces dysfunction in adjacent motor cortex as detected by intracortical microstimulation in rats.* Neuroscience, 2005. **130**(3): p. 601-10.

179.	Winship, I.R. and T.H. Murphy, *In vivo calcium imaging reveals functional rewiring of single somatosensory neurons after stroke.* J Neurosci, 2008. **28**(26): p. 6592-606.

180.	Reinecke, S., et al., *Induction of bilateral plasticity in sensory cortical maps by small unilateral cortical infarcts in rats.* Eur J Neurosci, 2003. **17**(3): p. 623-7.

181.	Fujioka, H., et al., *Epileptiform discharges and neuronal plasticity in the acute peri-infarct cortex of rats.* Neurol Res, 2010. **32**(6): p. 666-9.

182.	Castro-Alamancos, M.A. and J. Borrel, *Functional recovery of forelimb response capacity after forelimb primary motor cortex damage in the rat is due to the reorganization of adjacent areas of cortex.* Neuroscience, 1995. **68**(3): p. 793-805.

183.	Xerri, C., et al., *Experience-induced plasticity of cutaneous maps in the primary somatosensory cortex of adult monkeys and rats.* J Physiol Paris, 1996. **90**(3-4): p. 277-87.

184.	Xerri, C., et al., *Representational plasticity in cortical area 3b paralleling tactual-motor skill acquisition in adult monkeys.* Cereb Cortex, 1999. **9**(3): p. 264-76.

185.	Jones, T.A. and T. Schallert, *Use-dependent growth of pyramidal neurons after neocortical damage.* J Neurosci, 1994. **14**(4): p. 2140-52.

186.	Takatsuru, Y., et al., *Neuronal circuit remodeling in the contralateral cortical hemisphere during functional recovery from cerebral infarction.* J Neurosci, 2009. **29**(32): p. 10081-6.

187.	Buchkremer-Ratzmann, I., et al., *Electrophysiological transcortical diaschisis after cortical photothrombosis in rat brain.* Stroke, 1996. **27**(6): p. 1105-9; discussion 1109-11.

188.	Reinecke, S., et al., *Electrophysiological transcortical diaschisis after middle cerebral artery occlusion (MCAO) in rats.* Neurosci Lett, 1999. **261**(1-2): p. 85-8.

189.	Que, M., et al., *Changes in GABA(A) and GABA(B) receptor binding following cortical photothrombosis: a quantitative receptor autoradiographic study.* Neuroscience, 1999. **93**(4): p. 1233-40.

190.	Liepert, J., F. Hamzei, and C. Weiller, *Motor cortex disinhibition of the unaffected hemisphere after acute stroke.* Muscle Nerve, 2000. **23**(11): p. 1761-3.

191.	Bury, S.D. and T.A. Jones, *Unilateral sensorimotor cortex lesions in adult rats facilitate motor skill learning with the "unaffected" forelimb and training-induced dendritic structural plasticity in the motor cortex.* J Neurosci, 2002. **22**(19): p. 8597-606.

192.   Mohajerani, M.H., K. Aminoltejari, and T.H. Murphy, *Targeted mini-strokes produce changes in interhemispheric sensory signal processing that are indicative of disinhibition within minutes.* Proc Natl Acad Sci U S A, 2011. **108**(22): p. E183-91.

193.   Rehme, A.K., et al., *Activation likelihood estimation meta-analysis of motor-related neural activity after stroke.* Neuroimage, 2012. **59**(3): p. 2771-82.

194.   Ward, N.S., et al., *Neural correlates of outcome after stroke: a cross-sectional fMRI study.* Brain, 2003. **126**(Pt 6): p. 1430-48.

195.   Chen, J.L. and G. Schlaug, *Resting state interhemispheric motor connectivity and white matter integrity correlate with motor impairment in chronic stroke.* Front Neurol, 2013. **4**: p. 178.

196.   Marshall, R.S., et al., *Evolution of cortical activation during recovery from corticospinal tract infarction.* Stroke, 2000. **31**(3): p. 656-61.

197.   Calautti, C., et al., *Sequential activation brain mapping after subcortical stroke: changes in hemispheric balance and recovery.* Neuroreport, 2001. **12**(18): p. 3883-6.

198.   Rehme, A.K., et al., *The role of the contralesional motor cortex for motor recovery in the early days after stroke assessed with longitudinal FMRI.* Cereb Cortex, 2011. **21**(4): p. 756-68.

199.   Chollet, F., et al., *The functional anatomy of motor recovery after stroke in humans: a study with positron emission tomography.* Ann Neurol, 1991. **29**(1): p. 63-71.

200.   Cramer, S.C., et al., *A functional MRI study of subjects recovered from hemiparetic stroke.* Stroke, 1997. **28**(12): p. 2518-27.

201.   Foltys, H., et al., *Motor representation in patients rapidly recovering after stroke: a functional magnetic resonance imaging and transcranial magnetic stimulation study.* Clin Neurophysiol, 2003. **114**(12): p. 2404-15.

202.   Lotze, M., et al., *The role of multiple contralesional motor areas for complex hand movements after internal capsular lesion.* J Neurosci, 2006. **26**(22): p. 6096-102.

203.   Murase, N., et al., *Influence of interhemispheric interactions on motor function in chronic stroke.* Ann Neurol, 2004. **55**(3): p. 400-9.

204.   Nowak, D.A., et al., *Interhemispheric competition after stroke: brain stimulation to enhance recovery of function of the affected hand.* Neurorehabil Neural Repair, 2009. **23**(7): p. 641-56.

205.   Takeuchi, N., et al., *Repetitive transcranial magnetic stimulation of contralesional primary motor cortex improves hand function after stroke.* Stroke, 2005. **36**(12): p. 2681-6.

206.   Grefkes, C., et al., *Cortical connectivity after subcortical stroke assessed with functional magnetic resonance imaging.* Ann Neurol, 2008. **63**(2): p. 236-46.

207.   Turton, A., et al., *Contralateral and ipsilateral EMG responses to transcranial magnetic stimulation during recovery of arm and hand function after stroke.* Electroencephalogr Clin Neurophysiol, 1996. **101**(4): p. 316-28.

208.   Mansur, C.G., et al., *A sham stimulation-controlled trial of rTMS of the unaffected hemisphere in stroke patients.* Neurology, 2005. **64**(10): p. 1802-4.

209.   Takeuchi, N., et al., *Low-frequency repetitive TMS plus anodal transcranial DCS prevents transient decline in bimanual movement induced by contralesional inhibitory rTMS after stroke.* Neurorehabil Neural Repair, 2012. **26**(8): p. 988-98.

210.   Fregni, F., et al., *A sham-controlled trial of a 5-day course of repetitive transcranial magnetic stimulation of the unaffected hemisphere in stroke patients.* Stroke, 2006. **37**(8): p. 2115-22.

211.   Bertolucci, F., C. Chisari, and F. Fregni, *The potential dual role of transcallosal inhibition in post-stroke motor recovery.* Restor Neurol Neurosci, 2018. **36**(1): p. 83-97.

212.   H., F.W., *On the commissures of the cerebral hemispheres of the Marsupialia and Monotremata as compared with those of placental mammals. .* Philosophical Transactions of the Royal Society of London, 1865(23): p. 633-651.

213.   Aboitiz, F. and J. Montiel, *One hundred million years of interhemispheric communication: the history of the corpus callosum.* Braz J Med Biol Res, 2003. **36**(4): p. 409-20.

214.   Luders, E., P.M. Thompson, and A.W. Toga, *The development of the corpus callosum in the healthy human brain.* J Neurosci, 2010. **30**(33): p. 10985-90.

215.   Rockland, K.S. and D.N. Pandya, *Topography of occipital lobe commissural connections in the rhesus monkey.* Brain Res, 1986. **365**(1): p. 174-8.

216.   Kim, J.H., A. Ellman, and J.M. Juraska, *A re-examination of sex differences in axon density and number in the splenium of the rat corpus callosum.* Brain Res, 1996. **740**(1-2): p. 47-56.

217.   Innocenti G .M., A.-Z.D., Lehmann P. , *Cellular aspects of callosal connections and their development.* Neuropsychologia, 1995(33): p. 961-988.

218.   Innocenti, G.M. and D.O. Frost, *The postnatal development of visual callosal connections in the absence of visual experience or of the eyes.* Exp Brain Res, 1980. **39**(4): p. 365-75.

219.   Yorke, C.H., Jr. and V.S. Caviness, Jr., *Interhemispheric neocortical connections of the corpus callosum in the normal mouse: a study based on anterograde and retrograde methods.* J Comp Neurol, 1975. **164**(2): p. 233-45.

220.   Fame, R.M., J.L. MacDonald, and J.D. Macklis, *Development, specification, and diversity of callosal projection neurons.* Trends Neurosci, 2011. **34**(1): p. 41-50.

221.   Mitchell, B.D. and J.D. Macklis, *Large-scale maintenance of dual projections by callosal and frontal cortical projection neurons in adult mice.* J Comp Neurol, 2005. **482**(1): p. 17-32.

222.   Wilson, C.J., *Morphology and synaptic connections of crossed corticostriatal neurons in the rat.* J Comp Neurol, 1987. **263**(4): p. 567-80.

223.   Petreanu, L., et al., *Channelrhodopsin-2-assisted circuit mapping of long-range callosal projections.* Nat Neurosci, 2007. **10**(5): p. 663-8.

224.   Peters, A., B.R. Payne, and K. Josephson, *Transcallosal non-pyramidal cell projections from visual cortex in the cat.* J Comp Neurol, 1990. **302**(1): p. 124-42.

225.   Gonchar, Y.A., P.B. Johnson, and R.J. Weinberg, *GABA-immunopositive neurons in rat neocortex with contralateral projections to S-I.* Brain Res, 1995. **697**(1-2): p. 27-34.

226.   Fabri, M. and T. Manzoni, *Glutamic acid decarboxylase immunoreactivity in callosal projecting neurons of cat and rat somatic sensory areas.* Neuroscience, 2004. **123**(2): p. 557-66.

227.   Tamamaki, N. and R. Tomioka, *Long-Range GABAergic Connections Distributed throughout the Neocortex and their Possible Function.* Front Neurosci, 2010. **4**: p. 202.

228.   Zurita, H., P.L.C. Feyen, and A.J. Apicella, *Layer 5 Callosal Parvalbumin-Expressing Neurons: A Distinct Functional Group of GABAergic Neurons.* Front Cell Neurosci, 2018. **12**: p. 53.

229.   Jacobson, S. and J.Q. Trojanowski, *The cells of origin of the corpus callosum in rat, cat and rhesus monkey.* Brain Res, 1974. **74**(1): p. 149-55.

230.   Wise, S.P. and E.G. Jones, *The organization and postnatal development of the commissural projection of the rat somatic sensory cortex.* J Comp Neurol, 1976. **168**(3): p. 313-43.

231.   Schuz, A., et al., *Quantitative aspects of corticocortical connections: a tracer study in the mouse.* Cereb Cortex, 2006. **16**(10): p. 1474-86.

232.   Chovsepian, A., et al., *Heterotopic Transcallosal Projections Are Present throughout the Mouse Cortex.* Front Cell Neurosci, 2017. **11**: p. 36.

233.   Vidal, C.N., et al., *Mapping corpus callosum deficits in autism: an index of aberrant cortical connectivity.* Biol Psychiatry, 2006. **60**(3): p. 218-25.

234.   Freitag, C.M., et al., *Total brain volume and corpus callosum size in medication-naive adolescents and young adults with autism spectrum disorder.* Biol Psychiatry, 2009. **66**(4): p. 316-9.

235.   McAlonan, G.M., et al., *Differential effects on white-matter systems in high-functioning autism and Asperger's syndrome.* Psychol Med, 2009. **39**(11): p. 1885-93.

236.	Nowicka, A. and P. Tacikowski, *Transcallosal transfer of information and functional asymmetry of the human brain.* Laterality, 2011. **16**(1): p. 35-74.

237.	Renard, D., et al., *An MRI review of acquired corpus callosum lesions.* J Neurol Neurosurg Psychiatry, 2014. **85**(9): p. 1041-8.

238.	Ginger, M., et al., *Revealing the secrets of neuronal circuits with recombinant rabies virus technology.* Front Neural Circuits, 2013. **7**: p. 2.

239.	Wickersham, I.R. and E.H. Feinberg, *New technologies for imaging synaptic partners.* Curr Opin Neurobiol, 2012. **22**(1): p. 121-7.

240.	A., V.B., *The biology of viruses*. 1993, William C. Brown: Boston, MA. p. 386

241.	Ekstrand, M.I., L.W. Enquist, and L.E. Pomeranz, *The alpha-herpesviruses: molecular pathfinders in nervous system circuits.* Trends Mol Med, 2008. **14**(3): p. 134-40.

242.	Ugolini, G., *Rabies virus as a transneuronal tracer of neuronal connections.* Adv Virus Res, 2011. **79**: p. 165-202.

243.	Luo, L., E.M. Callaway, and K. Svoboda, *Genetic Dissection of Neural Circuits: A Decade of Progress.* Neuron, 2018. **98**(4): p. 865.

244.	Wickersham, I.R., et al., *Monosynaptic restriction of transsynaptic tracing from single, genetically targeted neurons.* Neuron, 2007. **53**(5): p. 639-47.

245.	Mebatsion, T., M. Konig, and K.K. Conzelmann, *Budding of rabies virus particles in the absence of the spike glycoprotein.* Cell, 1996. **84**(6): p. 941-51.

246.	Etessami, R., et al., *Spread and pathogenic characteristics of a G-deficient rabies virus recombinant: an in vitro and in vivo study.* J Gen Virol, 2000. **81**(Pt 9): p. 2147-53.

247.	Bates, P., J.A. Young, and H.E. Varmus, *A receptor for subgroup A Rous sarcoma virus is related to the low density lipoprotein receptor.* Cell, 1993. **74**(6): p. 1043-51.

248.	Young, J.A., P. Bates, and H.E. Varmus, *Isolation of a chicken gene that confers susceptibility to infection by subgroup A avian leukosis and sarcoma viruses.* J Virol, 1993. **67**(4): p. 1811-6.

249.	Federspiel, M.J., et al., *A system for tissue-specific gene targeting: transgenic mice susceptible to subgroup A avian leukosis virus-based retroviral vectors.* Proc Natl Acad Sci U S A, 1994. **91**(23): p. 11241-5.

250.	Reiner, A., et al., *Pathway tracing using biotinylated dextran amines.* J Neurosci Methods, 2000. **103**(1): p. 23-37.

251.	Schindelin, J., et al., *Fiji: an open-source platform for biological-image analysis.* Nat Methods, 2012. **9**(7): p. 676-82.

252.	Day, K.J., et al., *Improved deconvolution of very weak confocal signals.* F1000Res, 2017. **6**: p. 787.

253.	Rodriguez, A., et al., *Automated three-dimensional detection and shape classification of dendritic spines from fluorescence microscopy images.* PLoS One, 2008. **3**(4): p. e1997.

254.	Yu, F., et al., *Posttrauma cotreatment with lithium and valproate: reduction of lesion volume, attenuation of blood-brain barrier disruption, and improvement in motor coordination in mice with traumatic brain injury.* J Neurosurg, 2013. **119**(3): p. 766-73.

255.	Wearne, S.L., et al., *New techniques for imaging, digitization and analysis of three-dimensional neural morphology on multiple scales.* Neuroscience, 2005. **136**(3): p. 661-80.

256.	Rodriguez, A., et al., *Rayburst sampling, an algorithm for automated three-dimensional shape analysis from laser scanning microscopy images.* Nat Protoc, 2006. **1**(4): p. 2152-61.

257.	Won Young Yang, W.C., Tae-Sang Chung, John Morris, *Interpolation and Curve Fitting. Chapter 3*. 2005: Wiley Online Library.

258. Pollock, D., *Handbook of Time Series Analysis, Signal Processing, and Dynamics. Smoothing with Cubic Splines.* 1999: Wiley Online Library.

259. Schmued, L.C. and J.H. Fallon, *Fluoro-Gold: a new fluorescent retrograde axonal tracer with numerous unique properties.* Brain Res, 1986. **377**(1): p. 147-54.

260. Lanciego, J.L., et al., *Multiple neuroanatomical tracing in primates.* Brain Res Brain Res Protoc, 1998. **2**(4): p. 323-32.

261. Czeiger, D. and E.L. White, *Comparison of the distribution of parvalbumin-immunoreactive and other synapses onto the somata of callosal projection neurons in mouse visual and somatosensory cortex.* J Comp Neurol, 1997. **379**(2): p. 198-210.

262. O'Leary, D.D., B.B. Stanfield, and W.M. Cowan, *Evidence that the early postnatal restriction of the cells of origin of the callosal projection is due to the elimination of axonal collaterals rather than to the death of neurons.* Brain Res, 1981. **227**(4): p. 607-17.

263. Oswald, M.J., et al., *Diversity of layer 5 projection neurons in the mouse motor cortex.* Front Cell Neurosci, 2013. **7**: p. 174.

264. Wahl, M., et al., *Variability of homotopic and heterotopic callosal connectivity in partial agenesis of the corpus callosum: a 3T diffusion tensor imaging and Q-ball tractography study.* AJNR Am J Neuroradiol, 2009. **30**(2): p. 282-9.

265. Smith, D.H., D.F. Meaney, and W.H. Shull, *Diffuse axonal injury in head trauma.* J Head Trauma Rehabil, 2003. **18**(4): p. 307-16.

266. Singh, A., et al., *A new model of traumatic axonal injury to determine the effects of strain and displacement rates.* Stapp Car Crash J, 2006. **50**: p. 601-23.

267. Bonnier, C., et al., *Delayed white matter injury in a murine model of shaken baby syndrome.* Brain Pathol, 2002. **12**(3): p. 320-8.

268. Ivancevic, V.G., *New mechanics of traumatic brain injury.* Cogn Neurodyn, 2009. **3**(3): p. 281-93.

269. Duering, M., et al., *Incident subcortical infarcts induce focal thinning in connected cortical regions.* Neurology, 2012. **79**(20): p. 2025-8.

270. Duering, M., et al., *Acute infarcts cause focal thinning in remote cortex via degeneration of connecting fiber tracts.* Neurology, 2015. **84**(16): p. 1685-92.

271. Bareyre, F., et al., *Time course of cerebral edema after traumatic brain injury in rats: effects of riluzole and mannitol.* J Neurotrauma, 1997. **14**(11): p. 839-49.

272. Chen, J.Q., et al., *Effects of Aquaporin 4 Knockdown on Brain Edema of the Uninjured Side After Traumatic Brain Injury in Rats.* Med Sci Monit, 2016. **22**: p. 4809-4819.

273. Lu, H. and X. Lei, *The apparent diffusion coefficient does not reflect cytotoxic edema on the uninjured side after traumatic brain injury.* Neural Regen Res, 2014. **9**(9): p. 973-7.

274. Mizrahi, A. and L.C. Katz, *Dendritic stability in the adult olfactory bulb.* Nat Neurosci, 2003. **6**(11): p. 1201-7.

275. Losonczy, A., J.K. Makara, and J.C. Magee, *Compartmentalized dendritic plasticity and input feature storage in neurons.* Nature, 2008. **452**(7186): p. 436-41.

276. Gao, X. and J. Chen, *Mild traumatic brain injury results in extensive neuronal degeneration in the cerebral cortex.* J Neuropathol Exp Neurol, 2011. **70**(3): p. 183-91.

277. Kalil, K. and E.W. Dent, *Branch management: mechanisms of axon branching in the developing vertebrate CNS.* Nat Rev Neurosci, 2014. **15**(1): p. 7-18.

278. Hill, C.S., M.P. Coleman, and D.K. Menon, *Traumatic Axonal Injury: Mechanisms and Translational Opportunities.* Trends Neurosci, 2016. **39**(5): p. 311-324.

279. Hollis, E.R., 2nd, *Axon Guidance Molecules and Neural Circuit Remodeling After Spinal Cord Injury.* Neurotherapeutics, 2016. **13**(2): p. 360-9.

280. Fogarty, M.J., et al., *Cortical synaptic and dendritic spine abnormalities in a presymptomatic TDP-43 model of amyotrophic lateral sclerosis.* Sci Rep, 2016. **6**: p. 37968.

281.   Alexander, B.H., et al., *Stable Density and Dynamics of Dendritic Spines of Cortical Neurons Across the Estrous Cycle While Expressing Differential Levels of Sensory-Evoked Plasticity.* Front Mol Neurosci, 2018. **11**: p. 83.

282.   Erturk, A., et al., *Interfering with the Chronic Immune Response Rescues Chronic Degeneration After Traumatic Brain Injury.* J Neurosci, 2016. **36**(38): p. 9962-75.

283.   Harris, K.M., F.E. Jensen, and B. Tsao, *Three-dimensional structure of dendritic spines and synapses in rat hippocampus (CA1) at postnatal day 15 and adult ages: implications for the maturation of synaptic physiology and long-term potentiation.* J Neurosci, 1992. **12**(7): p. 2685-705.

284.   Portera-Cailliau, C., D.T. Pan, and R. Yuste, *Activity-regulated dynamic behavior of early dendritic protrusions: evidence for different types of dendritic filopodia.* J Neurosci, 2003. **23**(18): p. 7129-42.

285.   Fischer, M., et al., *Rapid actin-based plasticity in dendritic spines.* Neuron, 1998. **20**(5): p. 847-54.

286.   Grealish, S., et al., *Monosynaptic Tracing using Modified Rabies Virus Reveals Early and Extensive Circuit Integration of Human Embryonic Stem Cell-Derived Neurons.* Stem Cell Reports, 2015. **4**(6): p. 975-83.

287.   Wertz, A., et al., *PRESYNAPTIC NETWORKS. Single-cell-initiated monosynaptic tracing reveals layer-specific cortical network modules.* Science, 2015. **349**(6243): p. 70-4.

<h1 style="text-align: center;">Curriculum Vitae</h1>

Personal data

Full name: **Alexandra**

Surname: **Chovsepian**

Date of birth: 06/07/1989

Place of birth: Athens, Greece

Education and working experience

01/2019   Post-doctorate research at the Klinik für psychiatrie und psychotherapie, Department of Molecular Neurobiology, Ludwig Maximilian University of Munich.

07/2014 – 01/2018

    Doctorate/PhD research at the Ludwig Maximilian University of Munich

    Thesis title: *"Reappraisal of Transcallosal Neuron Organization in Mice and Evaluation of Their Dendritic Remodeling and Circuit Integration Following Traumatic Brain Injury"*

- Field: Group of Spinal Cord repair, Biomedical Center, Institute of Clinical Neuroimmunology
- Topic: Neuronal circuit remodelling in a mouse model of Traumatic Brain Injury
  - Promotor: PD Dr. Florence Bareyre
  - Employer: Klinikum der Universität München
- Lab Collaborations:
  - University of Geneva, Department of Pathology and Immunology
  - Klinikum der Universität München, Institut für Schlaganfall- und Demenzforschung (ISD)
- Supervision of Master students

02/2012 – 02/2014 MSc Diploma in Cognitive Neuroscience (honours: *"bene meritum"*)

    at the Radboud University, Nijmegen, The Netherlands

- Graduation internship (03/2013–02/2014) in the group of Behavioral Neurogenetics, Department of Cognitive Neuroscience/126, Donders

Institute for Brain, Cognition and Behavior, under supervision of Dr. J.R. Homberg with the title:

> *"Influence of serotonin transporter gene variation on social behavior and role of Oxytocin and CRF neurotransmission in social bonding"*

> Grade: 9 (Dutch scale, judicium: *"very good"*)

09/2007 – 11/2011   BSc Diploma in Biology (honours: upper second class)

Department of Biology, School of Science and Technology, University of Crete, Greece

➢ BSc graduation internship (04/2011-09/2011) in the Neurophysiology Lab, Department of Biology, under the supervision of Dr. K. Sidiropoulou with the title:

> *"Effects of the neurosteroid DHEA on Long Term Potentiation in the   mouse hippocampus."*

> Grade: 10 (Greek scale, judicium: "outstanding")

➢ Practical training (11/2010–02/2011) in the Neurophysiology Lab, Department of Biology, under the supervision of Dr. K. Sidiropoulou with subject:

> *"Synaptic properties of microcircuits in barrel and prefrontal cortex of mice"*

> Grade: 10 (Greek scale, judicium: "outstanding")

09/2004 – 07/2007   28th public Lyceum (High school) of Athens, Greece

➢ General higher education entrance qualification on 30.07.2007, grade: 18.30/20.00 (judicium: "excellent")

Scientific publications

2017   Chovsepian A*, Empl L*, Correa D, Bareyre FM. Heterotopic Transcallosal Projections Are Present throughout the Mouse Cortex. Frontiers in Cellular Neuroscience. 2017;11:36. doi:10.3389/fncel.2017.00036.

*These authors have contributed equally to the experiments, data analysis and manuscript for this publication.

In preparation   Empl L*, Chovsepian A*, Abdul Salaam S, Ertürk A, Merkler D, Liebscher S, Conzelmann KK, Bareyre FM. Rewiring of Injured Contralateral Neurons Following Traumatic Brain Injury.

*These authors have contributed equally to the experiments, data analysis and manuscript for this publication. Data from Laura Empl (not present in this thesis) are pooled in this publication with my own data presented in the current thesis.